

**Dissertation**  
submitted to the  
**Combined Faculties for the Natural Sciences and for Mathematics**  
**of the Ruperto-Carola University of Heidelberg, Germany**  
for the degree of  
**Doctor of Natural Sciences**

Put forward by

**Frederick Arand**

Born in: Karlstadt

Oral examination: 22.05.2019



# **Morphological Analysis, Digital Modeling, and Mechanical Simulation of Carbon Foam**

**Referees:** Prof. Dr. Jürgen Hesser  
Prof. Dr. Guido Kanschat



## Abstract

A carbon foam sample is investigated in three steps.

Analysis of the pore distribution of the foam is based on its computed tomography data set. For this purpose, an automatic segmentation algorithm is improved: Random access memory usage can be reduced up to two thirds. Effective radii of detected pores lie between  $r_{\text{eff}} = 1 \mu\text{m}$  and  $r_{\text{eff}} = 160 \mu\text{m}$ . Small pores with  $r_{\text{eff}} < 8 \mu\text{m}$  are spherical and occur abundantly. Large pores resemble ellipsoids, and are aligned to each other.

After analysis, carbon foam is modeled digitally. Void space is approximated by overlapping ellipsoids, which mimic the previously determined distribution of pores. Modeling is subdivided into two steps: First, around 9600 ellipsoids are packed in a virtual process. For efficiency, inner distances of intersecting ellipsoid surfaces are approximated. Then, small spheres are placed randomly within the remaining material. Altogether, a model foam with 100 000 pores is generated.

Multiple linear elastic mechanics simulations are conducted to compare mechanical properties of carbon foam and digital model. Depending on spatial direction, the elastic modulus of the real foam is between 10 % and 45 % larger than the modulus of the model. Finally, effective mechanical properties are compared with models which can be found in literature.

## Zusammenfassung

Eine Carbonschaumprobe wird in drei Schritten untersucht.

Basierend auf dem Computertomographie-Datensatz des Schaums werden zuerst dessen Hohlräume hinsichtlich der Porenverteilung analysiert. Ein automatischer Segmentierungsalgorithmus wird zu diesem Zweck verbessert, der Arbeitsspeicherbedarf wird um bis zu zwei Drittel reduziert. Die effektiven Radien der gefundenen Poren liegen zwischen  $r_{\text{eff}} = 1 \mu\text{m}$  und  $r_{\text{eff}} = 160 \mu\text{m}$ . Kleine Poren mit  $r_{\text{eff}} < 8 \mu\text{m}$  sind kugelförmig und treten mit großer Häufigkeit auf. Große Poren ähneln Ellipsoiden, die parallel zueinander ausgerichtet sind.

Nach der Analyse wird der Carbonschaum digital modelliert. Dabei werden Hohlräume durch überlappende Ellipsoide angenähert, deren Größenverteilung diejenige der Poren im realen Schaum abbildet. Die Modellierung ist zweigeteilt: Zunächst werden ca. 9600 Ellipsoide in einem virtuellen Prozess gepackt. Zur Effizienzsteigerung werden innere Abstände schneidender Ellipsoidoberflächen approximiert. Danach werden kleinen Kugeln zufällig im verbliebenen Material verteilt. Im Endeffekt kann so ein Modellschaum mit insgesamt 100 000 Poren erzeugt werden.

Mit Hilfe mehrerer linear-elastischer Mechaniksimulationen werden Carbonschaum und digitales Modell verglichen. Abhängig von der Raumrichtung liegt das Elastizitätsmodul des realen Schaums zwischen 10 % und 45 % über dem des Modellschaums. Abschließend werden die effektiven Mechanikeigenschaften mit Literaturmodellen verglichen.



This dissertation is dedicated to my family.



# Table of contents

<b>1</b>	<b>Introduction</b>	<b>1</b>
1.1	Motivation . . . . .	1
1.2	Morphological Analysis of Pore Space . . . . .	3
1.2.1	Fundamentals . . . . .	3
1.2.2	State of the Art . . . . .	7
1.3	Digital Modeling of Foam . . . . .	11
1.3.1	Fundamentals . . . . .	11
1.3.2	State of the Art . . . . .	12
1.4	Structural Mechanics Simulation . . . . .	15
1.4.1	Fundamentals . . . . .	15
1.4.2	State of the Art . . . . .	17
<b>2</b>	<b>Morphological Analysis of Pore Space</b>	<b>21</b>
2.1	Methods . . . . .	21
2.1.1	Preparation of Data Set . . . . .	22
2.1.2	Modified Maximal Ball Algorithm . . . . .	24
2.1.3	Statistical Analysis of Pores . . . . .	31
2.2	Computational Performance of Segmentation Algorithm . . . . .	35
2.2.1	Memory Efficiency . . . . .	35
2.2.2	Processing Speed . . . . .	36
2.3	Validation of Segmentation Algorithm . . . . .	37
2.3.1	Regular Sphere Pack . . . . .	37
2.3.2	Irregular Polydisperse Sphere Pack . . . . .	41
2.4	Statistics of Carbon Foam Sample . . . . .	44
2.4.1	Pore Size Distribution . . . . .	44
2.4.2	Anisotropy of Pores . . . . .	49

---

<b>3</b>	<b>Digital Modeling of Carbon Foam</b>	<b>53</b>
3.1	Methods . . . . .	53
3.1.1	Sampling of Ellipsoids . . . . .	54
3.1.2	Foaming Heuristic for Large Pores . . . . .	55
3.1.3	Sequential Addition of Small Pores . . . . .	61
3.1.4	Comparison to Literature . . . . .	61
3.2	Statistics of Model . . . . .	62
3.2.1	Pore Size Distribution . . . . .	63
3.2.2	Anisotropy of Modeled Pores . . . . .	64
3.2.3	Wall Thickness Distribution . . . . .	66
<b>4</b>	<b>Structural Mechanics Simulation</b>	<b>67</b>
4.1	Methods . . . . .	67
4.1.1	Preparation of Data Sets for Mechanics Simulation . . . . .	67
4.1.2	Mechanics Simulation with VGSTUDIO MAX . . . . .	68
4.2	Evaluation of Simulations . . . . .	69
4.2.1	Simulations in x-Direction . . . . .	69
4.2.2	Simulations in y- and z-Direction . . . . .	71
4.2.3	Comparison to Literature . . . . .	73
<b>5</b>	<b>Conclusion</b>	<b>77</b>
	<b>References</b>	<b>81</b>

# Chapter 1

## Introduction

### 1.1 Motivation

According to Antoine de Saint-Exupery,

“It seems that perfection is attained not when there is nothing more to add, but when there is nothing more to remove.”<sup>1</sup>

Inanimate nature, which is studied by physicists, shows this kind of perfection in two ways. First, objects of nearly arbitrary complexity, from galaxies to molecules, can be reduced to a few properties, which still allow meaningful and accurate predictions. Second, matter is distributed so sparse that there is indeed nothing more to remove. Atoms are a popular example: More than 99.9 % of the rest mass is concentrated in a central region which has a relative diameter of 0.001 %. Multiple kinds of sparsity are found at all length scales, up to the universe as we know it. Often, structures are distributed in fascinating ways, i.e., there are regular and irregular patterns, see fig. 1.1.

Carbon foam is a particularly interesting structure: It is a recently developed material, finds broad applications, and has an appealing geometric composition (details follow in section 1.2.1).

The main goal of this thesis lies in creating a virtual, geometric model of carbon foam. Compared to previous models found in literature, the model in this thesis should be able to match a given sample more closely. This can be achieved in three steps: First, the geometry of the given real foam sample needs to be analyzed quantitatively, in an effective and precise way. Second, the geometric model needs to introduce new degrees of freedom compared to current literature models, else it is not possible to achieve a closer match between foam sample

---

<sup>1</sup>“Il semble que la perfection soit atteinte non quand il n’y a plus rien à ajouter, mais quand il n’y a plus rien à retrancher.”, *Terre des Hommes* (1939)

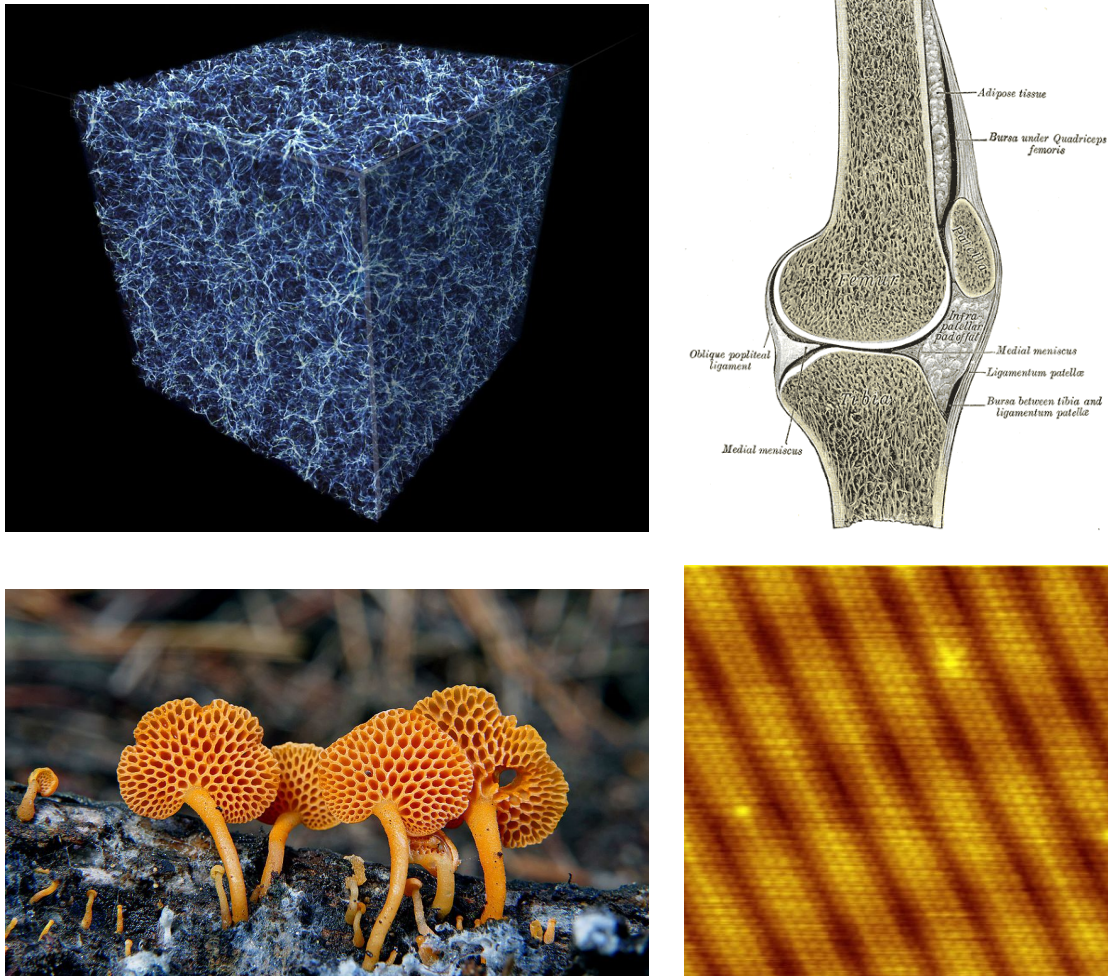


**Fig. 1.1** Structures at different length scales (Images in Public Domain, 2019).

**Top left:** Structure of the universe, also called “cosmic web”. Length scale:  $> 10^{25}$  m

**Top right:** Cross section of human knee. Length scale:  $10^{-1}$  m

**Bottom left:** Orange Pore Fungi. Length scale:  $10^{-2}$  m

**Bottom right:** Gold atoms, observed using a Scanning Tunneling Microscope. Length scale:  $10^{-10}$  m

and model. Third, agreement of sample and model needs to be validated, using properties that cannot be controlled in the modeling process.

Parts of this thesis are related to publications which contributed to the scientific community (Arand and Hesser, 2017; Arand and Hesser, 2018).

## 1.2 Morphological Analysis of Pore Space

At this point, introductions are given for each of the three thesis chapters (see also the table of contents). Each introduction is divided into two parts: First, fundamentals are summarized. Topics are ordered from relatively general to more specific to the chapter's content. Second, the state of the art is given. Each later chapter is intended to contribute to the corresponding state of the art.

### 1.2.1 Fundamentals

#### **Properties and Applications of Natural and Industrial Foams**

*Nature's hierarchical materials* such as wood and bone are reviewed by Fratzl and Weinkamer (2007). Both show the significance of porous structures, and motivate why natural materials often guide the design of industrial foams. Wood and bone have cellular anisotropic structures, i.e., they consist of a bulk material and at least another material, and cells are oriented in distinct directions. The advantages of anisotropy and cellularity can be highlighted with the example of bones: Anisotropy of cells adapts to external stress fields, an observation already made in 1892, known as Wolff's law (see English translation: Wolff, 2010). Cells are oriented such that stability is achieved against main loading directions, cellularity (porosity) itself results in a light material (Mosekilde et al., 2000).

Different types and applications of industrial metal foams are summarized by García-Moreno (2016): The author categorizes foams into open cell sponges and closed cell foams, and gives examples of major manufactures and products. Typical applications of metal foams are listed, for example energy (crash) absorption in cars and trains, mechanical stability of mobile cranes, passive thermal cooling in heat exchangers, and sound absorption in audience halls.

Baumeister, Banhart, and Weber (1997) discuss the application of aluminum foams with respect to energy absorption in detail. Investigated foams have a very low density (lower than water). The authors measure non-linear relationships between foam density and mechanical properties such as Young's modulus.

## Carbon Foam Production and Applications

Inagaki, Qiu, and Guo (2015) explain different carbon foam production methods, and typical applications. Five classes of production methods are given. For example, carbon foam may be produced from a template of another material, such as polyurethane foam, which is then carbonized in a multi-step chemical process. Another carbon foam production method is based on (mesophase) pitches, for example consisting of coal tar or petroleum. The pitch is heated to a temperature around 300 °C, then a pressure of approximately 5 MPa is released within 5 s. In a final step, the carbon foam is treated with temperatures above 1000 °C. The carbon foam sample which is discussed in this thesis is pitch-derived.

Multiple applications of carbon foam are discussed by Inagaki, Qiu, and Guo (2015). Composites of paraffin and carbon foam (which acts as a container) can be used for thermal energy storage, since carbon foam has high thermal conductivity, low density, low thermal expansion, and low chemical activity. Furthermore, carbon foam can be used for electrodes, since it has a high corrosion resistance. The large surface area and open pore structure makes carbon foam suitable for adsorption, examples are organic liquids such as oil.

Klett, Hardy, et al. (2000) discuss production methods for mesophase pitch derived carbon foams. The authors show how variations in the production parameters lead to different foam characteristics, which are measured extensively, for example by Scanning Electron Microscopy (SEM) and X-ray diffraction. Klett, McMillan, et al. (2004) discuss how the aligned graphitic structures in pitch-derived carbon foams are correlated to their high thermal conductivity.

Yuan et al. (2016) present a curious and cost effective production method for carbon foam, which is based on materials that can be bought in a food market. The foam is based on yeast, flour, and deionized water. A bread is baked and dried, then it is burnt under an Argon atmosphere. The authors discuss effects of variations in the production process. Example applications of the foam are electromagnetic interference (EMI) shielding and thermal insulation.

Zhang et al. (2016) discuss graphene foam with respect to microwave absorption, which has applications in military aircrafts because of a low radar cross-section combined with resistance to heat and mechanical stress.

Lee et al. (2016) examine the capabilities of carbon foam to remove heavy metal from industrial waste water. The authors also find that carbon foam has low toxic effects on human cells.

### Computed Tomography

As mentioned before, two methods for morphological analysis of porous structures are SEM and X-ray diffraction. Computed Tomography (CT) is another important non-destructive examination method. Buzug (2008) gives an extensive introduction to the 3D imaging method.

Wildenschild and Sheppard (2013) review techniques for the analysis of CT datasets, applied to porous media and multi-phase fluid flow. The authors describe X-ray fluorescence tomography (XRF). In contrast to conventional CT, XRF uses pencil beams, and is therefore comparably slow in image acquisition time. However, precise information about material can be obtained. Furthermore, the authors summarize many methods which are also described in this section, such as segmentation with the Maximal Ball algorithm.

### Noise Filtering

Noise in volumetric data sets can be attenuated with filters of increasing complexity. An example for a simple filter is the median filter (Huang, Yang, and Tang, 1979): It replaces each image value by the median inside its immediate neighborhood.

Many denoising filters require noise estimation. A straightforward method is described by Immerkær (1996): The image is convoluted with a Laplacian kernel (similar to the second derivative). If the image has a low amount of edges, then the mean absolute value of the convoluted image is nearly equivalent to the noise variance.

Tai and Yang (2008) extend the method: The Laplacian kernel is applied to image areas where the first derivative has a low absolute value. These areas have probably no edges if the data set is not textured, i.e., edges are not ubiquitous.

A noise estimation method which can handle textured data sets and has a good accuracy given the fast noise estimation speed, is described by Pyatykh, Hesser, and Zheng (2013): Image block covariance matrices are evaluated by principal component analysis (PCA). The smallest Eigenvalues of the covariance matrices estimate the noise level.

Computationally and theoretically more involved noise filters (which require prior noise estimation) are the non-local means filter (Buades, Coll, and Morel, 2005; Darbon et al., 2008) and the BM4D filter (Maggioni et al., 2013): The filters compare image patches across the entire image and exploit self-similarity of natural images for noise attenuation. It should be noted that more complex filters usually produce higher quality images: Ideally, when the filtered image is subtracted from the noisy image, pure noise should remain.

## Segmentation of Void Space

In a typical workflow, after denoising, CT images are segmented into phases. This thesis is only concerned with two-phase systems, i.e., data sets with material phase and void phase. A method that suggests global segmentation thresholds for multiple phases is introduced by Tenginakai, Jinho Lee, and Machiraju (2001): Grey value distributions of image blocks are evaluated with respect to statistical properties, such as the kurtosis. The statistical properties take characteristic values if a boundary is present, and subsequently reveal possible segmentation thresholds.

Iassonov, Gebrenegus, and Tuller (2009) review segmentation methods for greyscale CT images. The authors compare experimental porosity measurements with those obtained from image segmentation. Different global thresholding techniques are evaluated, and locally adaptive segmentation is investigated. It is found that local image information, for example spatial correlation, combined with locally adaptive techniques, yields good results.

Gibson (1998) describes how smooth surfaces can be extracted from binary data: A “surface net” is relaxed such that it minimizes its energy, while nodes of the net are constrained to their respective voxel cubes. Standard approaches like the marching cube algorithm (Lorenson and Cline, 1987) are compared.

## Euclidean Distance Transform

Single phases, for example the void phase, can be segmented further. Most automatic segmentation algorithms for porous media are based on the Euclidean Distance Transform (EDT), according to Rabbani, Jamshidi, and Salehi (2014). The EDT gives the shortest distance between each void space position and the material phase. Danielsson (1980) describes a simple algorithm to obtain the EDT in 2D, which can be readily generalized to 3D.

Meijster, Roerdink, and Hesselink (2000) prove that their implementation of the EDT can be calculated in linear time. The authors also show how their algorithm can be applied to metrics other than the Euclidean metric, for example the Manhattan (city-block) metric.

Felzenszwalb and Huttenlocher (2012) generalize the EDT from distance metrics towards a class of minimization problems with cost functions. The proposed algorithm still runs in linear time.

Lindblad and Sladoje (2015) introduce an EDT algorithm which is based on “grid line sampling”. The authors argue why their algorithm is subvoxel precise. A detailed explanation of the algorithm can be found in section 2.1.1.

## 1.2.2 State of the Art

At this point, pore space segmentation algorithms are summarized, followed by their application to CT data sets. Usually, segmentation algorithms classify void space into pores and throats, where the relationship between pores and void space is similar to the one between caves and a cave system, and throats connect pores.

### Skeleton Based Segmentation

The image skeleton (or medial axis) is one way to analyze pore spaces. Given the 3D pore space, the image skeleton is typically a collection of 1D lines (edges), which are centered in the void space, and are connected by intersections and junctions.

Serra and Vincent (1992) give an overview of morphological filters, for example erosion and dilation. If an erosion filter is applied to an image phase, then the outer layer of the voxelized phase is removed, and the total phase volume shrinks. For example, applying the erosion filter multiple times to the material phase of a soil data set can already be sufficient to identify large grains (Homberg, Binner, et al., 2009).

Cornea, Silver, and Min (2007) give an overview of different skeletonization methods. Two classes of methods are mainly used: Thinning (also called burning) and distance field based methods. Thinning methods are based on repeated applications of an erosion filter, until only voxels which are relevant for the overall topology remain (which are then the skeleton). In distance field based methods, the skeleton is identified with ridges of the distance field. Ridges are typically obtained by evaluation of derivatives of the distance field.

Homberg, Baum, et al. (2014) present an algorithm which segments the void phase of a data set which already has a segmented material phase: For example, many soils have grains that can be easily segmented, however, the pore network of the void space might be of interest. In the algorithm, a skeleton is found by propagating the segmented material phase into the void phase. A merging logic simplifies the skeleton. Nodes in the skeleton which coincide with maxima of the distance field correspond to pore centers, nodes which coincide with saddle points correspond to throats.

Delgado-Friedrichs, Robins, and Sheppard (2015) provide detailed mathematical background for skeletonization and segmentation, based on discrete morse theory (Forman, 1998). In simple terms, discrete morse theory can be used to identify topologically interesting points in the distance field, such as the previously mentioned maxima, minima, saddle points, and skeleton edges. The authors use the combined (signed) distance transform of material and void phase, and construct a complete skeleton which spans over both phases. Next, they simplify the

skeleton with a logic which is similar to the merging logic of the previously discussed authors (Homberg, Baum, et al., 2014). Finally, the authors give runtimes and images of segmentations.

### **Maximal Ball Algorithm**

Silin and Patzek (2006) introduce a new type of segmentation algorithms, based on *Maximally Inscribed Spheres*. Before explaining their algorithm, the authors discuss shortcomings of other approaches which rely on the medial axis/ image skeleton: For example, ambiguities arise when the analysis direction is changed. The authors proceed to explain the concept of Maximally Inscribed Spheres: Void space is filled with overlapping spheres, such that each sphere is as large as possible (without containing material). It should be noted that the definition of a maximal sphere closely corresponds to the distance field, which is further explained in sections 2.1.1 and 2.1.2. After void space is filled with maximal spheres, a hierarchy is build such that larger spheres are ancestors of smaller ones, and sphere clusters make up individual pores.

Later papers change the name of the method to *Maximal Ball algorithm* (MBa). The MBa is updated with respect to more efficient hierarchy computations by Al-Kharusi and Blunt (2007). Extracted pore networks are evaluated with respect to statistical properties such as pore sizes, and absolute permeabilities are calculated from the networks and compared to experiments.

An extensive overview about the MBa and pore network extraction can be found in the PhD thesis of Dong (2008). A state of the art implementation of the MBa is described by Dong and Blunt (2009): Compared to the original method by Silin and Patzek (2006), it is faster and more memory efficient, mainly due to simplifications of the hierarchy computation. The authors provide morphology statistics of artificial data sets for verification, and evaluate real data sets with pore statistics and with multiphase flow simulations.

Raeini, Bijeljic, and Blunt (2017) combine the maximal ball algorithm with medial axis analysis in order to obtain detailed information on pore geometries. The authors split pores into so-called half-throats. Using the half-throats, connections between pores are parameterized, for example with respect to angle and volume. The authors use flow simulations on real data sets to show that the added complexity of their pore network is able to reproduce experimental findings better than the conventional pore network (Dong and Blunt, 2009).

### **Other Void Space Segmentation Methods**

Rabbani, Jamshidi, and Salehi (2014) give an overview of different segmentation algorithms such as skeleton-based algorithms and Maximal Ball algorithms. The authors proceed to combine different aspects of previous algorithms into a new one. Notably, they replace the

usual Euclidean distance transform by a city-block distance transformation, and embed their algorithm into a fixed pipeline which includes preprocessing steps such as median filtering.

Rabbani, Ayatollahi, et al. (2016) use their watershed-based segmentation algorithm to segment 2D images and 3D volumes. Then, the authors proceed to analyze 25 rock samples, and correlate the coordination numbers in 2D to those in 3D, with respect to mean and standard deviation. Finally, the authors use 5 rock samples to show that their calibrated formula is able to predict 3D coordination number statistics from the segmentation of 2D slices.

Gostick (2017) develops a segmentation method which relies on simple image processing tools, which are available for Matlab, Python or ImageJ. The author compares the algorithm to other state-of-the-art algorithms, and it shows good agreement. Furthermore, runtime information is given.

To some extent, defining where a pore ends and a throat begins is arbitrary, which is discussed by Kim, Kim, and Lindquist (2013). The authors also show examples for intersecting throats, and give an algorithm that quickly finds those in actual data sets.

### **Studies Based on Foam Morphology**

Morphological analysis based on CT imaging has broad applications. Some have been mentioned before, such as classification of data sets by pore statistics, and single-/multi-phase flow simulation, based on pore networks.

Olurin et al. (2002) use CT to examine open cell and closed cell aluminum foams, with respect to parameters such as wall thickness and cell size. Effects of CT resolution and thresholding techniques onto measured porosities are studied.

Maire (2003) analyzes CT images of several porous structures, including aluminum, bread crumbs, concrete, and polyurethane foam. Subsequently, cell sizes and wall thickness are evaluated. Mechanics simulations are conducted with regular model foams, based on beam elements. Then, the authors proceed to simulate mechanical behavior directly on a small region of the CT data set.

More research on aluminum foams is done by Benouali et al. (2005). First, the authors conduct mechanical compression tests with their foam specimens. Next, the authors analyze the foams with respect to cell size distribution, preferred cell orientations and axes lengths of ellipsoids which approximate foam cells.

Knackstedt et al. (2006) analyze polyurethane foams with respect to morphological properties such as volume-to-surface-area ratio, covering radius, and cord length. Simulations are conducted on the CT images of multiple samples in order to relate porosity to properties such as thermal conductivity, diffusivity and mechanical properties. The authors compare their simulations to literature models and experimental data.

In the first part of a two part study, Andrä et al. (2013a) focus on imaging and segmentation. Three real and one artificial data sets are investigated by three independent teams with respect to phase segmentation, and are then compared.

In the second part (Andrä et al., 2013b), various effective physical properties are calculated, such as mechanical moduli, absolute permeability, and electrical resistivity. Different simulation methods are used for the calculation of each property. Altogether, results of the simulation methods differ at most by a factor of 1.5.

Hormann et al. (2016) characterize silica monoliths in detail. The authors compare different approaches to obtain morphological parameters such as coordination numbers. Then, they use the void space skeleton to quantify connectivity of pores, a variation of the MBa for segmentation, and a shortest path algorithm to evaluate geometric tortuosity of the data set.

Bultreys, Van Hoorebeke, and Cnudde (2015) simulate fluid flow using a multi-scale pore network model. A CT scan is partitioned into three phases: Material, macroscopic pore space, and microscopic pore space (where pores are smaller than the resolution). The authors segment the macroscopic pore space using the MBa. If macroscopic pores are adjacent to a common region with microporosity, then they are connected with each other via so-called micro-links. Micro-links are modeled with regular, cubic pore networks. The authors then proceed to use results of micropore simulations inside the macropore simulation. Finally, the method is validated using an artificial data set and experimental results of a limestone.

### **Possibilities and Limitations**

In summary, pore space segmentation is typically part of digital rock physics workflows, where the extracted pore network is used for single- or multiphase fluid flow simulations. In some cases, the extracted pores and skeletons themselves are analyzed for their geometric properties. The following limitations can be identified:

- Requirements of computational memory are relatively large for Maximal Ball algorithms. This is discussed by Arand and Hesser (2017) and in section 2.2.1. The modified Maximal Ball algorithm (mMBa) is described in detail in section 2.1.2, it aims for better memory efficiency.
- Hierarchy computations and simplifications seem to be a bottleneck of other algorithms. For example, in the algorithm by Delgado-Friedrichs, Robins, and Sheppard (2015), the simplification step typically makes up more than 70 % of the total runtime. The mMBa lifts these limitations by computing a flat hierarchy efficiently, which only needs one kind of simplification (“pore merging”). The simplification step in the mMBa needs around 10-40 % of the total runtime (Arand and Hesser, 2017).

- For carbon foams, pore sizes and anisotropy are typically obtained using methods other than automatic segmentation (see “Comparison to Literature” in later sections), while in the digital rocks community, segmentation algorithms (such as the MBa) are an established tool. In section 2.4, it is shown how automatic segmentation with the MBa can give meaningful results in the context of carbon foams.

## 1.3 Digital Modeling of Foam

Digital foam modeling is a common method for better understanding of different sorts of foam, and for conducting parametric studies.

### 1.3.1 Fundamentals

#### Random Sphere Packing

Several foam models, in particular those of carbon foams, are based on random sphere packs.

The Lubachevsky Stillinger algorithm (LSa) (Lubachevsky and Stillinger, 1990) sets the foundation for a class of event-driven molecular dynamics (EDMD) sphere packing methods. Instead of updating a configuration of spheres with respect to subsequent points in time, the system of spheres is advanced from one collision (event) to another. An initial sphere configuration has a low volume fraction. Between subsequent collisions, sphere diameters grow. The algorithm finishes when the relative growth of sphere diameters gets close to the numerical resolution.

Kansal, Torquato, and Stillinger (2002) extend the LSa to polydisperse sphere packs, where sphere radii have different values. The algorithm starts with a polydisperse, low density configuration. Each sphere grows proportional to its initial diameter, which preserves relative size ratios to other spheres. The authors discuss the algorithm at the applied example of bidisperse sphere packings.

A more rigorous, mathematically underpinned method is presented by Torquato and Jiao (2010). The authors formulate the sphere packing problem inside a fundamental cell, which is defined by a Bravais lattice. Non-overlap of spheres is formulated by a system of inequalities. In each step of the algorithm, the lattice shrinks by a small relative amount. Sphere configurations are optimized in each step using sequential linear programming techniques (Dantzig, 1963). The authors validate that their algorithm produces strictly jammed packings (Atkinson, Stillinger, and Torquato, 2013): They are stable against compression and shear.

### 1.3.2 State of the Art

Roberts and Garboczi (2002), investigate three different models for open foams, which cover a wide class of materials. The first model is based on a Voronoi tessellation, where cell centers are placed according to an irregular sphere pack, in order to have roughly uniform cell sizes. Foam ligaments are then placed at intersections of three or more cells. The second model is based on nearest neighbor node-bond rules. For example, each node is connected to all neighbors which are closer than a maximum distance. The third model is based on Gaussian random fields, which assign spatially correlated random numbers to each point in space. A threshold (level set) then distinguishes between background and foam material. For each foam model, the authors proceed to simulate effective mechanical properties, and derive relationships between Elastic modulus, Poisson's ratio, and foam densities.

#### Voronoi Tessellation Based Models

Li, Gao, and Subhash (2006) use Voronoi tessellation to construct open cell foams. The authors study the effect of two model parameters onto effective mechanical properties of the generated virtual foams. First, cell size regularity is varied, and it is found that increased cell irregularity corresponds to a higher effective elastic modulus. Second, a parameter controls regularity of ligament thickness. In contrast to the findings about cell sizes, the authors find that more irregular ligament thickness corresponds to a decrease of the effective elastic modulus. Finally, the authors find that cross-sectional shapes of ligaments have a significant effect on overall mechanical properties.

Gaitanaros, Kyriakides, and Kraynik (2012) create a random model of aluminum foam. Centers of a random sphere pack are used as seeds of a Voronoi tessellation. Then, the foam is optimized for Plateau's laws (Taylor, 1976), in particular the law that in natural foams, cell faces have a constant mean curvature. The software Surface Evolver (Brakke, 1992) is used to adjust surface curvature according to Plateau's laws. In order to introduce anisotropy, the authors stretch their model. The virtual foam is then used to simulate crushing behavior with the finite element (FE) software LS-DYNA.

#### Unit Cell Based Models

Gong, Kyriakides, and Jang (2005) analyze polyurethane foam with SEM. From the micrographs, the authors show that the cross-sectional shape of ligaments can be modeled by triangles which have inwardly curved sites. The authors proceed to model individual nodes and ligaments with curved triangles, and relate mechanical properties using finite element simulation. Then,

the authors simulate the macroscopic structure, using beam elements and the commercial software ABAQUS.

De Jaeger et al. (2011) analyze five different aluminum foams with CT. Then, the authors create a periodic model based on a unit cell. Inside the unit cell, the authors control cross-sectional ligament shape and thickness. An iterative algorithm is used to match the model and CT measurements, until surface-to-volume ratio and porosity agree.

### **Modeling of Carbon Foam**

Examples for carbon foam modeling follow. Sihn and Roy (2004) model carbon foam at a microstructural level. In the model, four foam ligaments meet at a central node inside a tetrahedral unit cell. According to mechanics simulations conducted by the authors, the elastic modulus of carbon foam can be enhanced by improving the modulus at the center of the ligaments. Variations of the central node (where the four ligaments meet) have a comparably minor effect.

Beechem, Lafdi, and Elgafy (2005) model growth of a single, non-spherical bubble in two dimensions. The authors assume that an isothermal Newtonian fluid surrounds the bubble seed. Changes in external parameters, such as pressure, result in distinct changes of the final bubble shape. Model bubbles are compared to photographs of actual bubbles in carbon foam, and the authors suggest that foam producers can use insights from the model to tailor foams for specific applications.

Kirca et al. (2007) observe that pores of pitch-derived carbon foam resemble spheres. Subsequently, the authors model carbon foam using packings of overlapping spheres. The sphere size distribution is obtained from analysis of scanning electron microscopy (SEM) images. The authors convert their model to computer aided design (CAD) datasets. In the next step, effective mechanical properties of the CAD data set are simulated with the finite element software ABAQUS. Model foams with different porosities are evaluated. A comparison between the created foams and literature models yields good agreement with respect to effective mechanical properties.

Dyck and Straatman (2015) also model carbon foam with overlapping spheres. A bubble contact law describes pairwise interactions of spheres. The spherical bubbles are sampled from a normal distribution. Finally, computational fluid dynamics (CFD) simulations are used to compare effective properties of the model, such as the permeability, to other models from literature.

## Ellipsoid Packing

The next step with respect to carbon foam modeling lies in approximating pores by ellipsoids instead of spheres, which is done in this thesis. For arbitrary bodies, an effective ellipsoid can be obtained using principal component analysis, as described by Wijewickrema and Papliński (2005).

In a two part paper (Donev, Torquato, and Stillinger, 2005a; Donev, Torquato, and Stillinger, 2005b), the authors discuss ellipsoid packing, based on event-driven molecular dynamics. Part one describes how near-neighbor lists are used to make the algorithm efficient. If ellipsoids are very aspherical, the authors use clusters of bounding spheres for fast vicinity checks. The second paper describes how overlap potentials (Perram and Wertheim, 1985) are used to evaluate distances between ellipsoids. For systems with very aspherical ellipsoids, the authors show that their algorithm is two orders of magnitude faster than previous algorithms. Finally, applications are given, such as ellipsoid packings inside spherical containers.

Birgin, Lobato, and Martínez (2016) introduce an ellipsoid packing method based on non-linear optimization. The authors are able to pack up to 100 ellipsoids to a jammed state. In another work, the method is extended (Birgin, Lobato, and Martínez, 2017), such that mid-sized packing problems with up to 1000 ellipsoids can be solved within a reasonable time. The authors provide implementations of the algorithms online.

## Possibilities and Limitations

In summary, foam modeling helps to understand (carbon) foam in two different ways. Unit cell approaches uncover the effects of constituting elements such as ligaments (also called struts or edges) and nodes onto the overall foam properties. Macroscopic models are able to reflect natural variations common to real world foams. It is possible parameterize these variations, and directly study their effects. In the literature, no carbon foam models have been found that model pore space with ellipsoids of varying size and elongation. Subsequently, the new modeling technique is described in chapter 3 (and by Arand and Hesser, 2018). Furthermore, ellipsoid packing is typically investigated under strict requirements, such as the non-overlap criterion. Therefore, a simple ellipsoid packing heuristic which fits the requirements of the analyzed foam sample is given in this thesis.

## 1.4 Structural Mechanics Simulation

### 1.4.1 Fundamentals

#### Finite Element Analysis

Finite Element Analysis (FEA) is a standard method in computational physics: Space is divided into smaller units (finite elements), which obey physical laws, and are coupled with each other. Several books give insightful introductions to FE. Two examples are Bathe (2006) and Bower (2009), the latter is very comprehensive and was made available online by the author.

FEA can be studied by applied examples, using the FE library deal.II (Bangerth, Hartmann, and Kanschat, 2007). The collaborative project offers extensive tutorials on the website, divided into “steps”. Steps 1-3 provide a good starting point for understanding finite elements.

In step 1, a finite element mesh is created: The 2D mesh (“triangulation”) consists of quadrilaterals, which are refined at areas of interest. Similarly, in real world 3D applications, meshes can consist of hexahedral elements. Tetrahedral mesh cells are also common in many applications.

In step 2, shape functions and degrees of freedom (DoF) are explained. FEA is used to calculate physical quantities (in this thesis: a displacement field), that satisfy equations and constraints (in this thesis: Hooke’s law and boundary conditions (BC)). Quantities (such as the displacement field) are continuous in space, while the FE mesh defines a discrete set of nodes. Each node represents the weight of a locally constrained shape function, and the superposition of weighted shape functions approximates the solution of the physical equations. Weights of shape functions are numbered consecutively, the total number of shape functions gives the global degrees of freedom.

In step 3, an example equation is given (Poisson’s equation). The solution of a finite element analysis fulfills the physical equation in the weak sense (in integral form). Now, the complete FEA problem can be formulated with the help of a system of linear equations. On the left hand side, a system matrix is multiplied with a solution vector. Elements in the system matrix represent the interaction of overlapping shape functions. Elements in the solution vector correspond to the searched-for weights of the shape functions. The vector on the right hand side is a result of the problem formulation, i.e., it is dependent on the physical equations and boundary conditions. Finally, the solution vector (shape function weights) is obtained by solving the FEA problem with methods such as the conjugate gradient (CG).

## Iterative Solution of Sparse Systems of Equations

Barrett et al. (1994) provide templates for methods which solve systems of equations iteratively. Examples for discussed methods are stationary methods such as the Jacobi method and the Gauss-Seidel method, and nonstationary methods such as the conjugate gradient. For each method, mathematical concepts are introduced, as well as requirements that the system of equations has to fulfill. The authors discuss different preconditioners, which are used to speed up convergence of methods.

A more extensive, and yet comprehensible book was written by Saad (2003). It gives the theoretical background to a complete selection of solution methods, and gives detailed technical instructions about data structures and parallel implementations. The book is provided online for free by the author.

## Finite Cell Method

The commercial software which is used in the thesis relies on a Finite Element Method (FEM) which is called the Finite Cell Method (FCM). Düster et al. (2008) introduce the FCM, and Schillinger and Ruess (2015) review it extensively.

In the FCM, analysis space is typically divided into regular, hexahedral cells, which are completely independent of the geometrical object which is analyzed. This is a major contrast to conventional FEM, where finite elements are aligned to the object and its boundary.

Shape functions which lie entirely inside or outside the geometrical object are handled similarly to the FEM. However, if the object boundary cuts a finite cell, then the cell is treated in a special way: The geometrical object is embedded inside in a proxy material, which has a stiffness that is typically 6 orders of magnitude lower. As a consequence of embedding, the hexahedral geometry of each cell is restored. Because of the treatment of cut cells, the FCM is also categorized as an “embedded domain method”.

While the simplicity of a regular mesh is a strength of the FCM, Dirichlet boundary conditions (BC) that do not coincide with cell boundaries require elaborate treatment. Fernández-Méndez and Huerta (2004) compare different methods for the imposition of Dirichlet BC in embedded domain methods. The authors highlight several positive aspects of the Nitsche method.

The Nitsche method (Burman and Hansbo, 2012; Schillinger and Ruess, 2015) imposes BC in the weak sense, i.e., equations are not fulfilled point-wise, but agree if they are integrated inside each finite cell. Embar, Dolbow, and Harari (2010) describe the weak imposition of Dirichlet BC, using the Nitsche Method, for spline-based FEM.

Variations of the FCM employ basis-splines (B-splines) and non-uniform rational B-splines (NURBS) (Piegl and Tiller, 2012) as shape functions. B-splines are piecewise polynomials with properties that are useful for finite elements, such as their quick computation and regularity.

NURBS-based FCM is related to the isogeometric analysis method (Hughes, Cottrell, and Bazilevs, 2005), which has applications to calculations on CAD (Computer-aided design) datasets, which commonly use NURBS as constitutive geometry elements. The authors explain that NURBS-based shape functions offer special refinement strategies. “Traditional” basis functions provide h-refinement (spatial refinement at interesting regions) and p-refinement (degree elevation of shape functions). NURBS shape functions enable k-refinement, which can be understood as a combination of p- and h-refinement with favorable mathematical properties.

It is possible to study the FCM with a MATLAB implementation, called FCMLab (Zander et al., 2014). Calculations can be done in 2D and 3D. Simple geometries can be generated and evaluated. Analysis of arbitrary 3D data, imported as a surface mesh, is possible as well.

If high-order elements are chosen for the FCM, then resulting system matrices are dense and ill-conditioned, i.e., the ratio between the largest and the smallest eigenvalue is large. The system of equations then needs to be solved directly (Schillinger and Ruess, 2015), opposed to iterative solving which was mentioned earlier.

## 1.4.2 State of the Art

### Effective Elasticity

When studying foams with mechanical simulations, effective properties are of interest, which are described by the elasticity tensor. Cowin and Mehrabadi (1987) classify different kinds of symmetry, ranging from triclinic symmetry (absence of elastic symmetry) to isotropic symmetry. The authors show how eigenvalue problems can be used to determine symmetry planes of the elasticity tensor, and furthermore, how to rotate the tensor into a system defined by such planes.

Van Rietbergen et al. (1996) describe how a full elasticity tensor can be obtained with the help of FEA. The authors show how the elasticity tensor can be rotated into its best orthotropic representation. Orthotropic material has perpendicular, distinguished directions in space. Furthermore, the authors demonstrate their method at the example of a CT dataset of trabecular bone specimen.

Pahr and Zysset (2008) compare different kind of boundary conditions (BCs), such as uniform displacement BCs and mixed BCs (a mixture of displacement and forces). The authors also compare different handling of the analyzed volumetric data set: It can be either analyzed as given, or it can be mirrored in order to induce additional symmetry (which increases the data set size by a factor of 8). After analyzing six samples of human bone using different BCs, the

authors argue that previous methods only calculate the “apparent elasticity tensor”, while the method which they introduce captures the actual “effective elasticity tensor”.

Veyhl et al. (2011) analyze CT data sets of two different aluminum foams with Finite Elements. Each data set is divided into 8 sub units. For each sub unit, effective Young’s moduli in the three space directions are obtained from uniaxial compression simulations with the software MSC.Marc. After the simulations, effective Young’s moduli are fitted against the relative density of the sub units.

### **Elastic Properties of Carbon Foam Models**

Kirca et al. (2007) calculate the effective Young’s modulus and Poisson’s ratio for a sphere-based carbon foam model, depending on the porosity of the model. For five different porosities, the authors calculate effective values by conducting finite element simulations along the z-axis (a similar approach will be taken in chapter 4). Then, the authors compare the effective properties with those obtained from literature formulas. An overview of the related publications follows, the formulas are written out in chapter 4. Although some of the literature models are not explicitly derived for carbon foam, they serve as good reference points.

Warren and Kraynik (1988) model open foam with the help of a tetrahedral unit cell. The cell consists of 4 equal struts (ligaments), which meet at a central node with an equal angle. Assuming that all orientations of the unit cell are equally probable, the authors derive the effective modulus of the macroscopic foam as a function of porosity. Furthermore, the authors discuss the effect which different strut shapes have on overall elasticity.

Zhu, Knott, and Mills (1997) model foam with tetrakaidecahedral cells (consisting of 14 faces), arranged on a body-centered cubic lattice. The authors derive a relationship between foam density and the effective modulus. Furthermore, they discuss the effect of different edge shapes, and compare their findings with Warren and Kraynik (1988).

Gan, Chen, and Shen (2005) create a periodic foam model, consisting of Voronoi cells with random seeds. The authors create multiple foams with different porosities, and obtain effective elastic moduli by finite element simulation. Then, the authors use curve fitting to derive the relationship between porosity and the elastic modulus. Furthermore, the authors introduce imperfections by breaking cell edges, and study effects on effective parameters.

Roberts and Garboczi (2002) model open foams with different models, as described in section 1.3.1. The model which comes closest to carbon foam is the Voronoi cell model, and is studied by the authors as follows: Strut thickness of the random foams is varied in order to change porosity. Then, computed effective moduli are fitted against the porosities.

**Possibilities and Limitations**

In the context of material research, finite element analysis is of increasing importance, enabled by better hardware and new methods that give good results, independent of the underlying geometry (such as the finite cell method). The state of the art is not extended by new methods or workflows in this thesis. However, the digital foam model in this thesis is validated with the help of mechanics simulations, and is compared to findings from literature (section [4.2.3](#)).



# Chapter 2

## Morphological Analysis of Pore Space

This chapter is concerned with analysis of three dimensional (3D) data sets, in particular a carbon foam sample. The same sample will be investigated in the other chapters as well.

First, methods are presented in section 2.1. Following the order of method descriptions gives a workflow which is applicable to a wide range of data sets. One of the methods, the *modified Maximal Ball algorithm* (mMBa) (Arand and Hesser, 2017), is explained in detail. Next, the mMBa is validated with the help of artificial data sets (section 2.3). Subsequently, the carbon foam sample is analyzed using the described methods (section 2.4).

Conceptual figures are given in two dimensions for more convenient visualization, however, terminology remains three dimensional (for example, voxel is used instead of pixel).

### 2.1 Methods

Analyses in this thesis are based on voxel data sets. A *position*  $\mathbf{x} = (x_1, x_2, x_3)^T \in \mathbb{R}^3$  with *coordinates*  $x_1, x_2, x_3$  is located inside Euclidean space  $\mathbb{R}^3$ . Voxels are centered at *voxel positions*  $\mathbf{x}_i \in \mathbb{N}^3$ , and can be indexed,  $i \in \{1, \dots, N_{\text{voxels}}\}$ . Voxel indices are numbered according to their x-y-z order, i.e.,

$$\mathbf{x}_i = (x_1, x_2, x_3) \in \mathbb{N}^3 \quad \Leftrightarrow \quad i = x_1 + N_x x_2 + N_x N_y x_3 \quad (2.1)$$

where  $N_x, N_y, N_z$  are the number of voxels in the corresponding directions, and  $N_x N_y N_z = N_{\text{voxels}}$ . Voxels are located in a *region*  $\mathcal{R} \subset \mathbb{R}^3$ ,

$$\mathcal{R} = [-0.5, N_x - 0.5] \times [-0.5, N_y - 0.5] \times [-0.5, N_z - 0.5] \quad (2.2)$$

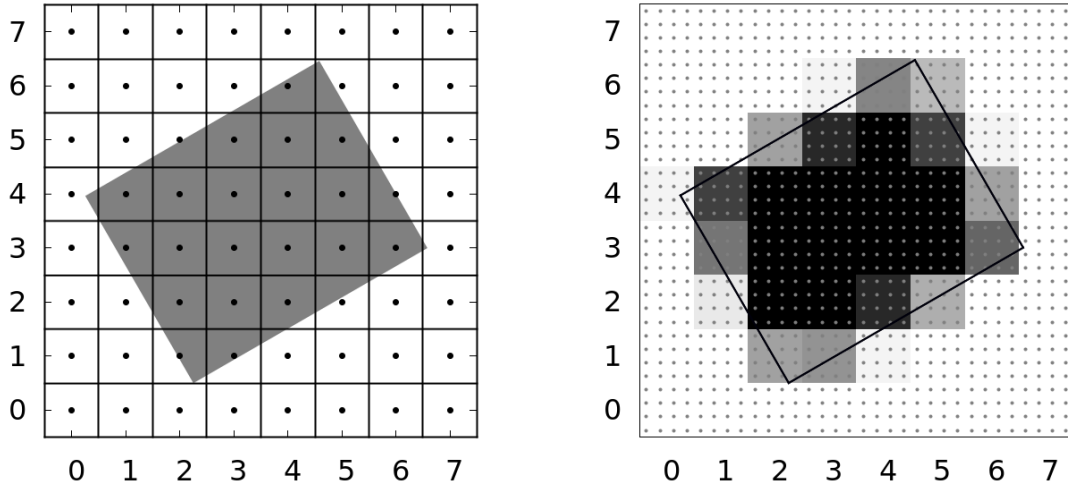


**Fig. 2.1** **Left:** Monodisperse material (white) with void cavity (gray), overlaid with voxel centers (points), and induced Voronoi cells (squares). **Right:** Coverage representation, where gray values of each voxel are proportional to sampling points inside the material.

Further partitioning of  $\mathcal{R}$  is possible with Voronoi cells, induced by the *set of voxel positions*  $\{\mathbf{x}_i\}$ .

### 2.1.1 Preparation of Data Set

Each investigated region  $\mathcal{R}$  is idealized to be partitioned into three parts: A void phase  $\Omega_{\text{void}}$ , a monodisperse material phase  $\Omega_{\text{mat}}$ , and an infinitesimal thin boundary  $\Gamma$  between the phases.  $\Omega_{\text{void}}$  is also called void space or pore space, while  $\Omega_{\text{mat}}$  is shortly called material. The goal of the following methods is further segmentation of  $\Omega_{\text{void}}$  into individual pores, which are related to void space as caves are related to a cave system.

Voxel values are noted as  $f_i = f(\mathbf{x}_i) \in \mathbb{R}$ . In actual data sets, voxel values are discrete. For example, if 1 Byte of memory is available for each voxel, its value is restricted to  $f_i \in \{0, \dots, 255\}$ . Voxel values are assumed to be a *coverage representation* (Lindblad and Sladoje, 2015) of the two phases, as visualized in fig. 2.1. In such a representation,  $f_i$  is proportional to the amount of material in the vicinity of  $\mathbf{x}_i$ . The vicinity of  $\mathbf{x}_i$  is defined by its surrounding Voronoi cell. Again, it should be noted that the coverage representation is idealized: In the coverage representation, the transition between material and void space is restricted to a width of 1 voxel, in contrast to real data sets, where the transition region can span several voxels as a result of CT imaging and reconstruction (Buzug, 2008).

Sampling of a coverage representation is coarse compared to the underlying phase distribution. A *segmentation threshold*  $t$ ,  $f_i \geq t$ , defines whether a voxel is filled with at least 50 %

material. Coverage representations can be partitioned according to  $t$ ,

$$\{\mathbf{x}_i^{\text{void}} \mid f_i < t\} \cup \{\mathbf{x}_j^{\text{mat}} \mid f_j \geq t\} = \{\mathbf{x}_k\} \quad (2.3)$$

with *void voxels*  $\{\mathbf{x}_i^{\text{void}}\}$  and *material voxels*  $\{\mathbf{x}_j^{\text{mat}}\}$ . Segmentation of  $\Omega_{\text{void}}$  into pores is based on  $\{\mathbf{x}_i^{\text{void}}\}$ .

### Preprocessing of CT Data

In this thesis, noise is estimated using the method described by Immerkær (1996): A  $3 \times 3 \times 3$  Laplacian kernel is convolved with the voxel volume. The averaged squared sum of the resulting voxel values is approximately proportional to the noise variance. It should be noted that the method only yields a good noise estimation if large areas without significant gradients are present. As can be seen later (section 2.4), the analyzed data set fulfills these requirements, since it consists of approximately 90 % void space.

Then, noise is attenuated with non-local means filtering (Buades, Coll, and Morel, 2005; Darbon et al., 2008), which reduces noise by averaging center values of similar volume patches within in the data set. The previously estimated noise level is incorporated as a parameter for non-local means denoising.

After noise removal, the data set is treated as a coverage representation. A background peak and a material peak are identified in the gray level histogram. The segmentation threshold  $t$  is taken from the minimum between both peaks.

Finally, material voxels that are “isolated” are removed: If  $\mathbf{x}_i^{\text{mat}}$  is not connected to the boundary of  $\mathcal{R}$  via a path through 27-neighborhoods of  $\{\mathbf{x}_j^{\text{mat}}\}$ , then it is set to a value  $f_i < t$ .

### Distance Field based on Grid Line Sampling

The modified Maximal Ball algorithm (mMBA) is based on the distance field of a data set. A *distance field*  $d(\mathbf{x})$  inside  $\mathcal{R}$  is defined as follows:

$$d(\mathbf{x}) = \min_{\mathbf{x}' \in \Omega_{\text{mat}}} \|\mathbf{x} - \mathbf{x}'\|_2 \quad (2.4)$$

In other words,  $d(\mathbf{x})$  gives the distance between a position  $\mathbf{x}$  and the closest material location. Discretized distance fields  $\{d_i\}$  which are based on binary data sets can be calculated in *linear time*  $\mathcal{O}(N_{\text{voxels}})$  (Danielsson, 1980; Meijster, Roerdink, and Hesselink, 2000). The calculation is also called *Euclidean Distance Transform* (EDT). A variation of the EDT (Lindblad and Sladoje, 2015) is used in this thesis: It approximates the EDT efficiently and subvoxel precise: In contrast to the previously mentioned publications, grey values are used to base the transfor-

mation on distances which are smaller than a voxel. This is achieved with the help of *grid line sampling*, which can be explained as follows.

Voxel positions  $\{\mathbf{x}_i\}$  coincide with intersections of perpendicular *grid lines*, which have at least two integer coordinates. Thus, *grid lines*  $\{\mathbf{x}^{\text{grid}}\}$  are defined as

$$\{\mathbf{x}^{\text{grid}} \mid \mathbf{x}^{\text{grid}} \in \mathbb{R} \times \mathbb{N}^2 \cup \mathbb{N} \times \mathbb{R} \times \mathbb{N} \cup \mathbb{N}^2 \times \mathbb{R}\} \quad (2.5)$$

*Grid values*  $f(\mathbf{x}^{\text{grid}})$  are assigned by linear interpolation of values of *voxel neighbors* on grid lines. A pair of voxel neighbors  $\mathbf{x}_i, \mathbf{x}_j$  has the property  $\mathbf{x}_i \pm \mathbf{e}_d = \mathbf{x}_j$ , with  $d$ -directional unit vector  $\mathbf{e}_d$ . Clearly, any position on a grid line can be written as  $\mathbf{x}^{\text{grid}} = \mathbf{x}_i + \lambda(\mathbf{x}_j - \mathbf{x}_i)$ , with  $0 \leq \lambda < 1$ . Now,  $f(\mathbf{x}^{\text{grid}}) = (1 - \lambda)f_i + \lambda f_j$ .

Given a segmentation threshold  $t$ , it is possible to obtain a grid line sampling from the previously defined coverage representation. Grid line sampling estimates *boundary positions*

$$\{\mathbf{x}_i^{\text{bound}} \mid \mathbf{x}_i^{\text{bound}} \in \{\mathbf{x}^{\text{grid}}\} \cap \Gamma^*\} \quad (2.6)$$

with approximative boundary  $\Gamma^*$  as follows: If  $(f_i - t)(f_j - t) < 0$  holds for a pair of grid neighbors, then

$$\mathbf{x}_k^{\text{bound}} = \mathbf{x}_i + \frac{|f_i - t|}{|f_i - f_j|}(\mathbf{x}_j - \mathbf{x}_i) \quad (2.7)$$

i.e.,  $f(\mathbf{x}_k^{\text{bound}}) = t$ . Finally, the distance field algorithm (Lindblad and Sladoje, 2015) approximates  $\{d_i\}$  such that

$$d(\mathbf{x}_i) = \min_{\mathbf{x}_j \in \{\mathbf{x}_k^{\text{bound}}\}} \|\mathbf{x}_i - \mathbf{x}_j\|_2 \quad (2.8)$$

An example can be seen in fig. 2.2.

### 2.1.2 Modified Maximal Ball Algorithm

Based on the EDT, a *Maximal Ball*  $\mathcal{MB}_i$  can be defined: It is the largest ball centered at  $\mathbf{x}_i \in \{\mathbf{x}_j^{\text{void}}\}$  with radius  $d(\mathbf{x}_i)$  which does not contain material.

The set of Maximal Balls  $\{\mathcal{MB}_i\}$  is the basis for segmentation of pore space into pores and throats. More precisely, the mMBA segments void voxels  $\{\mathbf{x}_i^{\text{void}}\}$  into smaller sets, i.e., pore voxels and throat voxels. As mentioned in the state of the art (section 1.2.2), pores are related to pore space as caves are related to a cave system, and throats are the connection between pores. There is no ideal number and shape of pores inside a given data set. Rather, a “good”

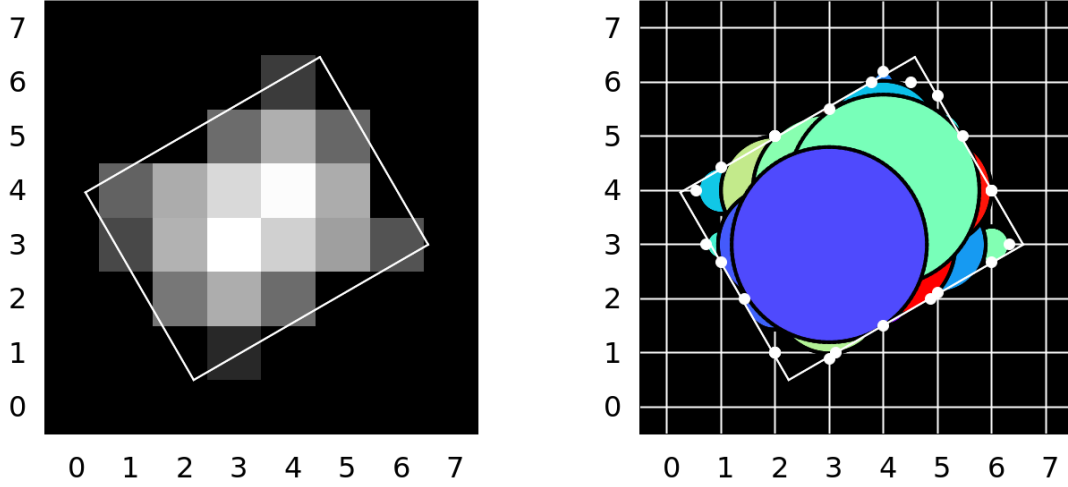


**Fig. 2.2 Left:** Euclidean distance transform  $\{d_i\}$ , obtained from fig. 2.1. Grey values are proportional to  $d_i$ . **Right:** Maximal Ball representation of the distance field. White dots represent estimated boundary positions, and are sampled on grid lines. Larger Maximal Balls are drawn on top of smaller ones.

segmentation is specified by its application (Kim, Kim, and Lindquist, 2013). In this thesis, the use-case is the identification of pores which are geometrically similar to ellipsoids, and membrane-like throats of 1 voxel thickness are favored.

A detailed description of the mMBA was given before (Arand and Hesser, 2017). However, it is explained in another fashion at this point.

### Initialization

The mMBA takes a distance field  $\{d_i\}$  as input. Then, a *morphology volume*  $\{m_i\}$  with equal dimensions  $N_x, N_y, N_z$  is created. Each *morphology value*  $m_i$  takes 32 bits of memory, where the first two bits encode a *state*  $m_i^{\text{state}}$ , the remaining 30 bits encode a *pore label*  $m_i^{\text{label}}$ :

$$m(\mathbf{x}_i) = m_i = \underbrace{\{m_i^{\text{state}}\}}_{b_0 b_1}, \underbrace{\{m_i^{\text{label}}\}}_{b_2 \dots b_{31}} \quad (2.9)$$

There are 4 possible states,

$$m_i^{\text{state}} \in \{\text{MATERIAL}, \text{INITIALIZED}, \text{INCLUDED}, \text{THROAT}\} \quad (2.10)$$

their meaning will be explained shortly.  $m_i^{\text{label}}$  stores up to  $2^{30} \approx 1.07 \times 10^{10}$  labels, which corresponds to the maximum number of pores the algorithm can process.

The basic idea is similar to a watershed segmentation: Labels propagate from pore centers as far as possible, by copying their value  $m_i^{\text{label}}$  to voxels inside the surrounding Maximal Ball  $\mathcal{M}\mathcal{B}_i$ , i.e.,  $m(\mathbf{x}_j)^{\text{label}} \leftarrow m(\mathbf{x}_i)^{\text{label}}$ . It is not allowed for a morphology value to have more than one label. Therefore, if two pores try to assign their label to a morphology value located at the same voxel, then its state changes, and it becomes a throat:  $m_j^{\text{state}} = \text{THROAT}$ . Before label propagation, the following steps are taken:

- The morphology volume is initialized:  $\forall i : m_i \leftarrow \{\text{INITIALIZED}, 0\}$ . It should be noted that  $m_i^{\text{label}} = 0$  is a special label, i.e., after segmentation, all void voxels have labels  $m_i^{\text{label}} \geq 1$ . Material voxels are excluded from the algorithm: If  $d_i = 0$ , then  $m_i^{\text{state}} \leftarrow \text{MATERIAL}$ .
- A processing order  $\{po(i)\}$  is established for  $\{\mathcal{M}\mathcal{B}_i\}$ , such that

$$po(i) < po(j) \Rightarrow d_i \geq d_j \quad (2.11)$$

i.e., Maximal Balls with large radii are processed before Maximal Balls with small radii. This is motivated by an intuitive approach of manual segmentation, where large structures are identified first. Furthermore, large Maximal Balls label many voxels, the latter might not have to be processed in following steps, resulting in increased algorithmic efficiency. It is possible that  $d(i) = d(j)$ . A strong ordering can be defined here, for example

$$po(i) < po(j) \Leftrightarrow i < j \quad \text{if } d(i) = d(j) \quad (2.12)$$

After establishing the processing order  $\{po(i)\}$ , the first Maximal Ball that is processed,  $\mathcal{M}\mathcal{B}_{po(1)}$ , has a radius which is the largest value in the distance field,

$$d_{po(1)} \geq d_i \quad \text{where } d_i \in \{d_j\} \quad (2.13)$$

### Inclusion of Maximal Balls

During the algorithm, Maximal Balls may *include* smaller balls: Given  $\mathcal{M}\mathcal{B}_i$  and  $\mathcal{M}\mathcal{B}_j$  with  $po(i) \leq po(j)$ , (i.e.,  $d_i \geq d_j$ ),

$$\mathcal{M}\mathcal{B}_j \overset{\approx}{\subseteq} \mathcal{M}\mathcal{B}_i : \quad \|\mathbf{x}_i - \mathbf{x}_j\|_2 + d_j \leq d_i + \varepsilon d_j \quad (2.14)$$

with  $0 \leq \varepsilon < 1$ . The symbol  $\overset{\approx}{\subseteq}$  means ‘‘approximately a subset of’’. For better understanding, the above equation can be worded: Maximal Ball  $j$  is approximately included by Maximal Ball  $i$  if a ball with radius  $d_i + \varepsilon d_j$  (with small padding  $\varepsilon d_j$ ) centered at  $\mathbf{x}_i$  is large enough such that

$\mathcal{M}\mathcal{B}_j$  is entirely contained within. Equivalently, one might say that the inclusion criterion allows the smaller ball  $\mathcal{M}\mathcal{B}_j$  to stick out of the larger ball  $\mathcal{M}\mathcal{B}_i$  by a small amount.

The case  $\varepsilon = 0$  is equivalent to the exact definition of included spheres (Silin and Patzek, 2006).  $\varepsilon > 0$  yields a relaxation of the “classic” inclusion criterion, in particular for balls with large radius  $d_j$  (as the padding  $\varepsilon d_j$  is proportional to  $d_j$ ). This results in a gain of processing speed without compromising the segmentation (see validations in section 2.3, and by Arand and Hesser, 2017). For the segmentations in this thesis,  $\varepsilon = 0.2$  was chosen. An example for included balls can be seen in fig. 2.3.

It should be noted that Dong and Blunt (2009) use a much more permissive inclusion criterion (which the authors call “absorption”): Using the above notation, and given that  $d_i \geq d_j$ , the criterion can be formulated as

$$\|\mathbf{x}_i - \mathbf{x}_j\|_2 \leq 2d_i \quad (2.15)$$

A clear advantage of the permissive criterion by Dong and Blunt (2009) is the quick hierarchy propagation. The criterion seems suitable for low porosity data sets with ramified tunnels, such as rocks. In contrast, for high porosity data sets, such as the validation data sets which are used in section 2.3 and the carbon foam sample, the permissive criterion would lead to severe under-segmentation.

### Label Propagation

All Maximal Balls are processed in the order  $\{po(j)\}$ , starting with  $\mathcal{M}\mathcal{B}_{po(1)}$  (fig. 2.3), ending at index  $po(N_{\mathcal{M}\mathcal{B}})$ . For convenience,  $po(j)$  is abbreviated as  $i = po(j)$ . Each  $\mathcal{M}\mathcal{B}_i$  is processed as follows, different stages of the algorithm are shown in fig. 2.4:

- First, the state of  $m_i$  is checked. If  $m_i^{\text{state}} \in \{\text{THROAT}, \text{INCLUDED}\}$ , then  $\mathcal{M}\mathcal{B}_i$  is skipped, and the algorithm continues in the processing order. (Included balls do not contribute to label propagation, and throats do not carry information about labels.)
- After the previous check, the state is  $m_i^{\text{state}} = \text{INITIALIZED}$ . If  $m_i^{\text{label}} = 0$  (for example, this is true for the first ball in the processing order,  $\mathcal{M}\mathcal{B}_{po(1)}$ ), then  $m_i$  was not labeled before, and a new pore label is assigned,  $m_i^{\text{label}} \leftarrow l$ . The global pore label index  $l$  is initialized as  $l = 1$  and is incremented by 1 after the each new pore assignment. If  $m_i^{\text{label}} \neq 0$ , i.e., a label was previously assigned to  $\mathbf{x}_i$ , then  $m_i^{\text{label}}$  is not changed.
- Now, the state is overwritten to  $m_i^{\text{state}} \leftarrow \text{INCLUDED}$ : Morphology values with  $m_i^{\text{state}} = \text{INCLUDED}$  become immutable to the algorithm, i.e., the label gets fixed.

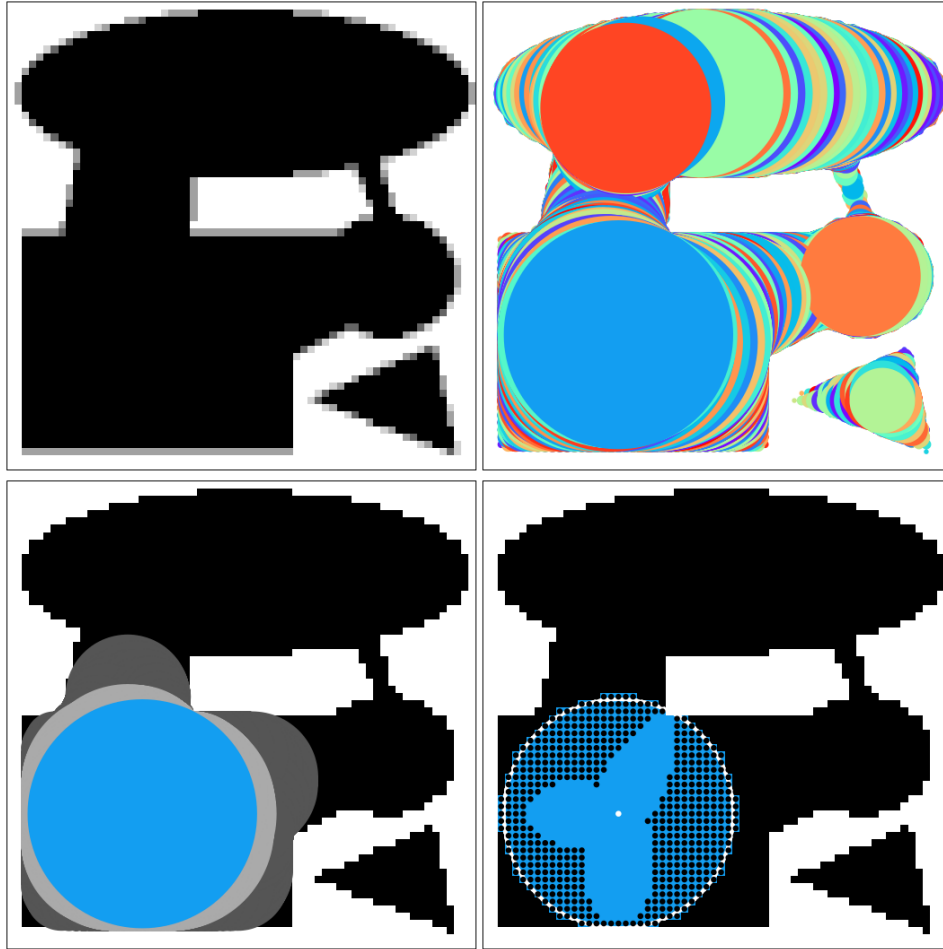


**Fig. 2.3** Initialization of the mMBA.

**Top left:** Coverage representation, obtained from idealized geometric elements.

**Top right:** Distance Field, which serves as algorithmic input, visualized with randomly colored Maximal Balls.  $\{d_i\}$  was produced from the coverage representation. It should be noted how well  $\{d_i\}$  reproduces subvoxel features such as the ellipse outline.

**Bottom left:** The mMBA is voxel based, i.e., segmentation is as coarse as  $\{\mathbf{x}_i\}$ . Material voxels (white) are ignored by the algorithm, void voxels in their initial state are colored black.  $\mathcal{M}\mathcal{B}_{po(1)}$  is colored blue. Balls which are included by  $\mathcal{M}\mathcal{B}_{po(1)}$  (2.14) are represented with light gray, those which are processed, but not included, are colored dark gray.

**Bottom right:**  $\{m_j\}$  after  $\mathcal{M}\mathcal{B}_{po(1)}$  was processed. A white dot represents the ball center. A white circle represents the ball radius  $d_{po(1)}$ . Colored voxels have  $m_j^{\text{label}} = 1$ . If a colored voxel has a black dot, then  $m_j^{\text{state}} = \text{INITIALIZED}$ , i.e., it will be processed later, and  $m_j^{\text{label}}$  might still change. If a colored voxel does not have a black dot, then  $m_j^{\text{state}} = \text{INCLUDED}$ , i.e., it will not be processed, and  $m_j^{\text{label}}$  remains fixed.

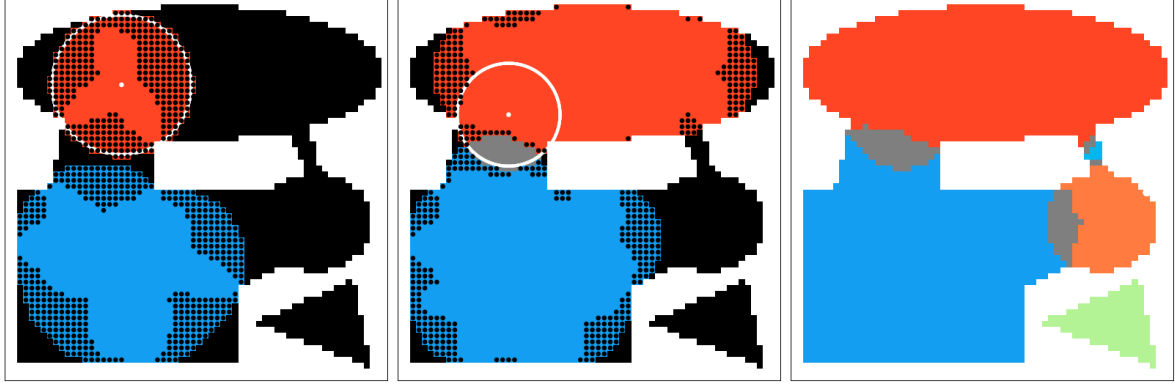


**Fig. 2.4**  $\{m_i\}$  at different stages of the algorithm. In the second picture, throat voxels can be seen (colored gray). The final result can be seen in the third picture.

- $\mathcal{M}\mathcal{B}_i$  may change surrounding balls  $\{\mathcal{M}\mathcal{B}_j\}$  which fulfill the following conditions: First, they have to come later in the processing order ( $d_i \geq d_j \wedge m_j^{\text{state}} \neq \text{INCLUDED}$ ). Second,  $\mathcal{M}\mathcal{B}_i$  has to (partially) overlap the voxel cell around  $\mathbf{x}_j$ ,

$$\|\mathbf{x}_i - \mathbf{x}_j\|_2 \leq d_i + 0.5 \quad (2.16)$$

- $\mathcal{M}\mathcal{B}_i$  modifies  $\mathcal{M}\mathcal{B}_j$  as follows: If  $m_j^{\text{label}} = 0$ , then  $m_j^{\text{label}} \leftarrow m_i^{\text{label}}$ . Additionally, if  $\mathcal{M}\mathcal{B}_j \subseteq \mathcal{M}\mathcal{B}_i$  according to eqn. 2.14, then  $m_j^{\text{state}} \leftarrow \text{INCLUDED}$ . Finally, if  $m_j^{\text{label}} \neq m_i^{\text{label}}$ , then it is marked as a throat,  $m_j^{\text{state}} \leftarrow \text{THROAT}$ .

### Throat Voxel Reduction

After label propagation, the volume is segmented into unique pores, and lense-shaped throat regions which are between pores.

As stated before, membrane-like throats are desired, similar to the description by Hormann et al. (2016). In order to obtain the membranes, throat voxels  $\{\mathbf{x}_i^{\text{throat}} \mid m_i^{\text{state}} = \text{THROAT}\}$  are separated into several connected regions:  $\{\mathbf{x}_i^{\text{throat}}\} = \{\{\mathbf{x}_k^{\text{throat}}\}_j\}$ , where each connected region  $\{\mathbf{x}_k^{\text{throat}}\}_j$  consists of voxels which are connected through 27-neighborhoods:

$$\mathbf{x}_m \in \{\mathbf{x}_k^{\text{throat}}\}_j \Rightarrow \exists \mathbf{x}_n \in \{\mathbf{x}_k^{\text{throat}}\}_j : |x_{m,d} - x_{n,d}| \leq 1 \text{ for } d = 1, 2, 3 \quad (2.17)$$

where  $\mathbf{x}_m = (x_{m,1}, x_{m,2}, x_{m,3})^T$  and  $|x|$  is the absolute value of  $x$ .

Now, each connected region can be reduced with a watershed process as follows:

- Voxels in the region are processed according to the previously described processing order (queue), i.e.,  $po(\mathbf{x}_i) < po(\mathbf{x}_j) \Rightarrow d(\mathbf{x}_i) \geq d(\mathbf{x}_j)$ .

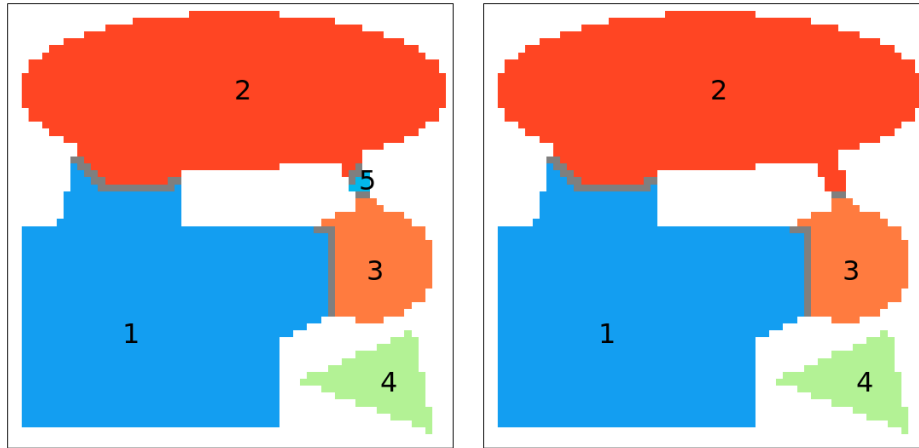


**Fig. 2.5 Left:** Throats are reduced to membranes. Pores are explicitly labeled. **Right:** Pore 5 was merged into pore 2: The largest maximal ball radius inside throat  $\{2, 5\}$  was greater than 80 % of the largest maximal ball radius inside pore 5.

- The 27-neighborhood of voxel  $\mathbf{x}_i$  is checked. If only throat and material voxels are found in the vicinity, then the next voxel is processed.
- If exactly one label is present in the 27-neighborhood of  $\mathbf{x}_i$ , i.e., all neighbor voxels which have  $m_j^{\text{state}} = \text{INCLUDED}$  also have  $m_j^{\text{label}} = l$ , then the morphology volume is modified at  $\mathbf{x}_i$ :  $m_i \leftarrow \{\text{INCLUDED}, l\}$ . In other words, the throat voxel at  $\mathbf{x}_i$  is changed to a labeled pore voxel. After the assignment,  $\mathbf{x}_i$  is removed from the processing queue, and processing continues at the beginning of the queue.
- If 2 or more labels are present in the 27-neighborhood of  $\mathbf{x}_i$ , then the current voxel is membrane-like, i.e. it is between two pores.  $\mathbf{x}_i$  is therefore a non reducible part of the throat, and removed from the processing queue. Again, processing continues at the beginning of the queue.

After the watershed process, all connected regions are reduced to membrane-like throats, see fig. 2.5.

### Network Construction and Pore Merging

A pore-throat network is a graph where vertices are pores and edges are throats. An example for its application is flow simulation (Dong and Blunt, 2009).

It is straightforward to obtain a pore-throat network from the morphology volume  $\{m_i\}$ . By construction, 27-neighborhoods of throat voxels contain all required information to map throats to surrounding pores. Similarly, given the mapping throats  $\rightarrow$  pores, the mappings

pores  $\rightarrow$  throats and pores  $\rightarrow$  pores can be constructed. For example, in fig. 2.5 (left), 5 pores are present. There are 4 throats, which can be uniquely identified by pairs of pore labels,  $\{1, 2\}$ ,  $\{1, 3\}$ ,  $\{2, 5\}$ ,  $\{3, 5\}$ .

In order prevent over-segmentation, pores may be merged into neighboring ones. First, the largest maximal balls inside each pore and throat is identified, using  $\{m_i\}$  and  $\{d_i\}$ . Their radii are  $\{d_j^{\text{pore}}\}$  and  $\{d_k^{\text{throat}}\}$ . Now, the set  $\{d_j^{\text{pore}}\}$  is processed in ascending order, i.e., the pore with the smallest radius is processed first. For each processed pore  $d_j^{\text{pore}}$ , if the largest connected throat  $d_k^{\text{throat}}$  is large compared to the pore,

$$d_k^{\text{throat}} > \lambda d_j^{\text{pore}} \quad (2.18)$$

with design parameter  $0 < \lambda < 1$ , then pore  $j$  is merged through throat  $k$  into the neighboring pore. In fig. 2.5, a choice of  $\lambda = 0.8$  leads to merging of pore 5 into pore 2. Smaller values of  $\lambda$  lead to more merging. For example, a value of  $\lambda = 0.76$  would have led to merging of pore 3 into pore 1.

Homberg, Baum, et al. (2014) suggest a similar merging heuristic: In their approach, merging is based on absolute differences of throat and pore radii. Opposed to that, the mMBa is based on relative sizes. An advantage of the relative criterion lies in the fact that one does not need to find a characteristic length scale. A disadvantage could be that arbitrarily large pores might merge as long as they are connected through a throat that is large enough.

### 2.1.3 Statistical Analysis of Pores

A set of pores is denoted as  $\{\mathcal{P}_i\}$ , where  $\mathcal{P}_i = \{x_j \mid m_j^{\text{label}} = i\}$ . Later in the thesis, pores are analyzed with respect to statistical properties, which are described as follows.

#### Pore Size and Histogram Binning

A pore volume  $V_i$  can be obtained by counting voxels inside  $\mathcal{P}_i$ . In order to make orders of magnitude more conceivable, pore sizes are given by their effective radius  $r_i^{\text{eff}}$  such that

$$V_i = \frac{4\pi}{3}(r_i^{\text{eff}})^3 \quad (2.19)$$

In contrast to the previous explanations of the mMBa, indices are not of importance for statistical analysis. Therefore, the following abbreviations will be used if applicable:  $V = V_i$  and  $r = r^{\text{eff}} = r_i^{\text{eff}}$ .

It is possible to identify statistical distributions by sorting the underlying values into a histogram  $h(x \mid x_i \leq x < x_{i+1})$ . Linear histograms are not useful if bins are filled sparsely, i.e.,

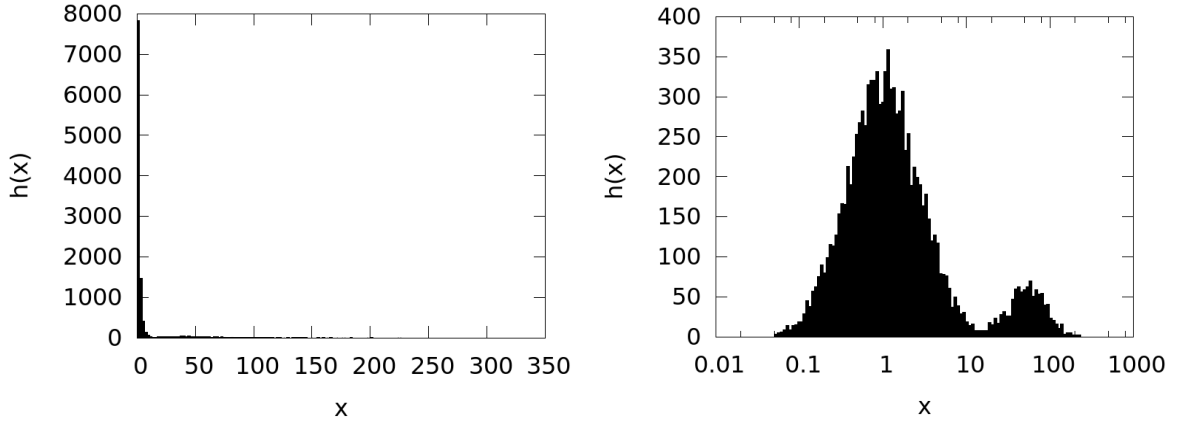


**Fig. 2.6** Values  $x$  are sampled from the sum of two arbitrarily chosen lognormal distributions. **Left:** A histogram  $h(x)$  with constant bin width is not suited to reveal the statistics **Right:** Choosing the bin width proportional to  $x$  captures the overall distribution.

if there is a substantial amount of bins with  $h(x) = 0$ . For example, it would be difficult to gain statistical information from lognormally distributed particle sizes (Whitby, 1978), sampled over several orders of magnitude: Small particles are abundant, while large ones are distributed sparsely. The resulting histogram would have a sharp peak at the left side, and many empty bins on the right side. In order to overcome this limitation, logarithmic histograms are used. They are defined with the following binning:

$$x_i = x_{\min} \left( \frac{x_{\max}}{x_{\min}} \right)^{(i-1)/N_{\text{bins}}} \quad (2.20)$$

Subsequently, the bin width is proportional to the binned values, i.e.,  $(x_{i+1} - x_i) \propto x_i$ . A visual comparison of a linear and logarithmic histogram in the case of lognormal distributions can be seen in fig. 2.6.

### Anisotropy of Pore Shapes

Some foams have pores that are approximately ellipsoidal, for example the analyzed carbon foam (see section 2.4). The closest matching ellipsoid for a pore can be found using principal component analysis (Wijewickrema and Papliński, 2005).

First, for each pore, the covariance matrix  $\Sigma$  is calculated:

$$\Sigma = \sum_i (\mathbf{x}_i - \langle \mathbf{x} \rangle) (\mathbf{x}_i - \langle \mathbf{x} \rangle)^T \quad (2.21)$$

where  $i$  runs over all pore voxels,  $\langle \mathbf{x} \rangle$  is the average voxel position inside the pore (center of mass), and  $\mathbf{xy}^T$  is the outer product of column vectors  $\mathbf{x}, \mathbf{y}$ . Next,  $\mathbf{\Sigma}$  is decomposed into eigenvalues and eigenvectors,

$$\mathbf{\Sigma} = \mathbf{V}\mathbf{\Lambda}\mathbf{V}^T \quad (2.22)$$

with orthonormal eigenvectors

$$\mathbf{V} = \begin{bmatrix} \mathbf{v}_1, \mathbf{v}_2, \mathbf{v}_3 \end{bmatrix} \quad (2.23)$$

and eigenvalues

$$\mathbf{\Lambda} = \text{diag}(\lambda_1, \lambda_2, \lambda_3) \quad (2.24)$$

Now, the closest matching ellipsoid  $\mathcal{E}$  for the given pore  $\mathcal{P}$  has axes which are oriented in directions  $\mathbf{v}_1, \mathbf{v}_2, \mathbf{v}_3$ . Axes lengths are  $\mathcal{A} = (a, b, c)$ , where  $a^2 : b^2 : c^2 = \lambda_1 : \lambda_2 : \lambda_3$ . Axes are scaled such that the ellipsoid volume is equivalent to the pore volume,  $(4\pi/3)abc = V_{\text{pore}}$ .

Later in the text, pore shapes will be analyzed statistically. It is possible to assign an averaged ellipsoid to a set of similarly sized pores  $\{\mathcal{P}_i\}$ : The averaged covariance matrix  $\langle \mathbf{\Sigma} \rangle$  is calculated. Then, it is decomposed according to eq. (2.22).

### Correction for Statistical Effects at the Data Set Boundary

Boundary pores contain at least one voxel which is adjacent to a boundary of the data set. Since boundary pores are trimmed by definition, their real shape is unknown. Therefore, they are not considered in the statistical analyses.

Excluding boundary pores falsifies statistics, as it is more likely for large pores to coincide with the region boundary, than for small pores. For example, for spherical pores, the following relation can be derived (Arand and Hesser, 2018): Given a sphere  $S$  with radius  $r$ , which has its center randomly placed inside a box of size  $L$ , the probability  $p(r, L)$  to find the sphere entirely inside the box is

$$p(r, L) = \frac{(L - 2r)^3}{L^3} \quad (2.25)$$

Similarly, the following formula is true for ellipsoids which are aligned with the coordinate-system:  $p(a, b, c, L) = (L - 2a)(L - 2b)(L - 2c)/L^3$ . It should be possible to formulate the probability for general, rotated ellipsoids, using the notation introduced in section 3.1. However, in the analysis of the carbon foam sample, the relation between boundary pore probability and



**Fig. 2.7** Wall thickness  $\{w_i\}$ , where increasing brightness corresponds to increasing wall thickness.

ellipsoid size is of interested, therefore, the probability will be calculated as

$$p \approx \frac{(L - 2r^{\text{eff}})^3}{L^3} \quad (2.26)$$

and is validated later with the help of fig. 2.15.

### Wall Thickness

Previous methods only focused on the void space. Insightful statistics can also be extracted from material voxels  $\{\mathbf{x}_i^{\text{mat}}\}$ , by evaluating the wall thickness distribution. Wall thickness at each  $\mathbf{x}_i^{\text{mat}}$  is determined with the sphere method (Inui et al., 2015), as follows: First, a distance field is calculated, as described earlier, this time on  $\{-f_i\}$  with segmentation threshold  $-t$ . Subsequently, each  $d(\mathbf{x}_i^{\text{mat}})$  gives the distance from  $\mathbf{x}_i^{\text{mat}}$  to the closest position  $\mathbf{x}' \in \Omega_{\text{void}}$ . Next, the wall thickness data set,  $\{w_i\}$ , is initialized as a copy of the distance field,  $\{w_i\} \leftarrow \{d_i\}$ . Finally, values in  $\{w_i\}$  are updated such that each  $w_i$  gets the radius of its maximal overlapping sphere : If  $w_i < d_j$  and  $\|\mathbf{x}_i - \mathbf{x}_j\|_2 \leq d_j$ , then  $w_i \leftarrow d_j$ . An example can be found in fig. 2.7. For further investigations, the wall thickness distribution can be represented as a histogram  $h(w)$  with  $w > 0$ .

## 2.2 Computational Performance of Segmentation Algorithm

### 2.2.1 Memory Efficiency

Following explanations in section 2.1.2, the mMBA needs to store three major data structures:

- $\{d_i\}$ , where it is sufficient to store  $d_i$  as single-precision float. This accounts to 4 Bytes per voxel.
- $\{m_i\}$ , where each  $m_i$  requires 4 Bytes per voxel, see eq. (2.9).
- $po(i)$  (processing order), which can be stored as a simple array-like structure. This requires 8 Bytes per void voxel, then the indices inside  $po(i)$  can cover large, but realistic use cases (example:  $2^{32} < N_{\text{voxels}} = 2000^3 < 2^{64}$ ).

Thus, the total memory  $M$  amounts to the sum

$$M = N_{\text{voxels}}(4 \text{ Bytes} + 4 \text{ Bytes}) + \phi N_{\text{voxels}}(8 \text{ Bytes}) \quad (2.27)$$

where the porosity  $\phi$  times number of voxels,  $\phi N_{\text{voxels}}$ , gives the amount of void voxels.

It is possible to further reduce  $M$  by partial processing of  $po(i)$ :

- First, after finding the maximum value of the distance field,  $d_{\text{max}}$ , only voxels with  $d_{\text{max}} \geq d_i > d_{\text{max}}/2$  are processed. For real-world data sets, it should hold that  $N_{\text{voxels}}(d_{\text{max}} \geq d_i > d_{\text{max}}/2) \ll N_{\text{voxels}}$ . Therefore, partial processing of  $po(i)$  requires a relatively small amount of memory, compared to full processing.
- Second, after the subset with the largest maximal balls was processed,  $d_{\text{max}}$  is updated,  $d_{\text{max}} \leftarrow d_{\text{max}}/2$ , and the next subset is processed. Now, it is important to note that balls which were included according to (2.14) will not be processed, leading to further memory reduction.

Partial processing is repeated until  $d_{\text{max}} \leq 2$ , then the final subset of  $po(i)$  consists of maximal balls with  $d_{\text{max}} \geq d_i > 0$  (which were not previously included by larger balls).

Following the arguments on partial processing, total memory is estimated to have the following upper limit:

$$M \leq N_{\text{voxels}}(4 \text{ Bytes} + 4 \text{ Bytes}) + (\phi N_{\text{voxels}}/8) (8 \text{ Bytes}) \quad (2.28)$$

where it is estimated that at most one eighth of void space is processed at once. This is a significant improvement compared to previous maximal ball algorithms, including the preceding

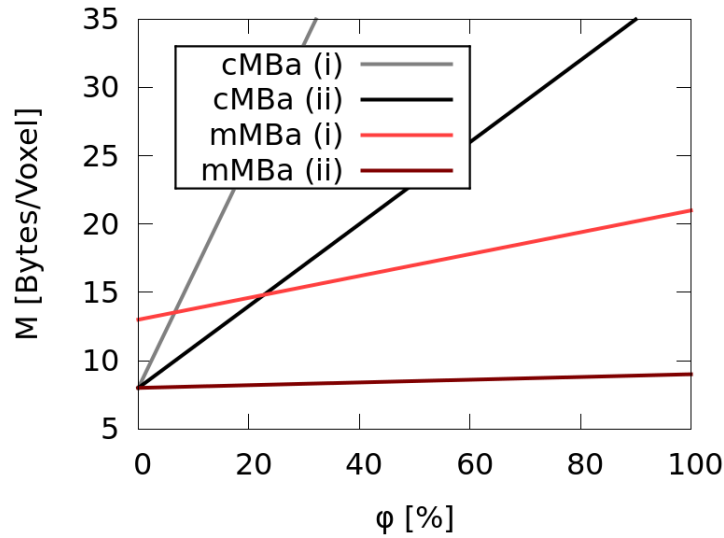


**Fig. 2.8** Required memory as a function of porosity for different MBa implementations: cMBa (i) (Silin and Patzek, 2006), cMBa (ii) (Dong and Blunt, 2009), mMBa (i) (Arand and Hesser, 2017), mMBa (ii) (current version).

mMBa implementation (Arand and Hesser, 2017), see fig. 2.8. In order to understand the memory requirements of the classic MB algorithms, their underlying data structures need to be discussed. Interested readers are referred to Arand and Hesser (2017).

It should be noted that the mMBa is also more memory-efficient than a recent segmentation algorithm which is not of the Maximal Ball type (Gostick, 2017): According to the authors, segmenting a volume of size  $1000^3$  voxels with their algorithm required 50 GB of RAM. As can be seen in fig. 2.8, the mMBa needs less than 10 GB for data sets of this volume size. In fact, later in this thesis, multiple data sets with size  $1000^3$  are segmented with a PC that is limited by 32 GB RAM.

In a recent publication, Raeini, Bijeljic, and Blunt (2017) describe a trick that saves memory and increase sprocessing speed: For an initial coarse segmentation, the authors use one voxel inside each  $2^3$  voxel block, reducing the problem size by a factor of 8. In comparison, the partial processing of the mMBa saves similar amounts of memory, without making compromises with respect to initial segmentation coarseness.

## 2.2.2 Processing Speed

A discussion of the algorithmic performance with respect to calculation speed is given by Arand and Hesser (2017). In summary, the mMBa is around 3 times faster than the MBa by Dong (2008), who made runtime information available in his thesis.

Previously (Arand and Hesser, 2017), it was stated that the void space segmentation algorithm by Homberg, Baum, et al. (2014) is around 2 times faster than the mMBa. It should be noted that the algorithm by Homberg, Baum, et al. (2014) needs a preceding segmentation of the material phase. Homberg, Binner, et al. (2009) state that their algorithmic material phase segmentation of a soil data set (size:  $1800^3$  voxels) takes as much as 5 days. If this additional step is understood as a part of the full segmentation pipeline of Homberg, Baum, et al. (2014), then the mMBa should be faster: For the soil data set, a conservative estimation (based on the measurements in Arand and Hesser, 2017) gives around 3 hours total runtime for segmentation with the mMBa.

## 2.3 Validation of Segmentation Algorithm

Two artificial data sets are used to validate the mMBa. First, a highly regular data set is used to evaluate the precision of the distance field, and as an initial check of automatic segmentation with the mMBa. Second, a more irregular data set evaluates details for the mMBa, i.e., boundary effects and the resolution limit. Readers which are interested in further validation (connectivity of an artificial pore network) are referred to Arand and Hesser (2017).

### 2.3.1 Regular Sphere Pack

A hexagonal close-packed (hcp) sphere configuration is created, where neighboring sphere centers have the distance  $d_{ij}^{\text{sphere}}$ , and each sphere has a radius  $r^{\text{sphere}} = 1.05(d_{ij}^{\text{sphere}}/2)$ . Subsequently, neighboring spheres have a small overlap. Spheres correspond to void space. The sphere configuration is voxelized, resulting in a coverage representation  $\{f_i\}$  with  $512 \times 512 \times 512$  voxels. In order to achieve a coverage representation, each voxel is sampled at  $8 \times 8 \times 8$  subvoxel positions for counting the containing material fraction.

The distance between sphere centers is chosen to be  $d_{ij}^{\text{sphere}} = 512/20 = 25.6$ .

### Results

Automatic segmentation is done with the mMBa. The input sphere radius is denoted as  $r^{\text{sphere}}$ , measured pore radii are denoted as  $r^{\text{pore}}$ . They are compared in fig. 2.9. Furthermore, the input circle radius  $r^{\text{circle}}$  is compared to throat radii  $r^{\text{throat}}$ , see also fig. 2.9. The circle radius  $r^{\text{circle}}$  is the result of two intersecting sphere surfaces in the hcp-packed configuration,  $(r^{\text{circle}})^2 = (r^{\text{sphere}})^2 - (d_{ij}^{\text{sphere}}/2)^2$ .

Input sphere centers,  $\mathbf{c}^{\text{sphere}}$ , have real coordinates, i.e., are in  $\mathbb{R}^3$ . Measured pore centers, in contrast, are constrained by voxelization, i.e., they have integers positions,  $\mathbf{c}^{\text{pore}} \in \mathbb{N}^3$ . Fig.

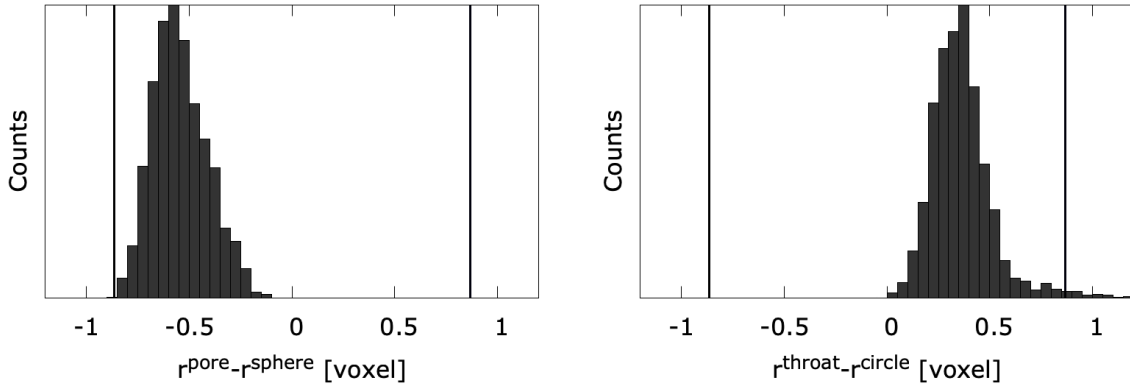


**Fig. 2.9 Left:** Histogram for difference of measured pore radii ( $r^{\text{pore}}$ ) and given sphere radius ( $r^{\text{sphere}}$ ). ( $r^{\text{sphere}} = 13.44$ ). Vertical lines indicate  $\Delta r = \pm\sqrt{3}/2$ . **Right:** A similar histogram for measured throat radii and given circle radius.

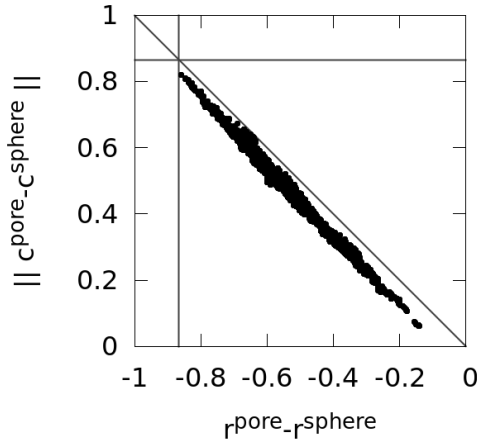


**Fig. 2.10** Distance of segmented pore center to next sphere centers,  $\|\mathbf{c}^{\text{pore}} - \mathbf{c}^{\text{sphere}}\|_2$ , as a function of measured radius. A vertical and a horizontal line indicate half a voxel diagonal,  $\sqrt{3}/2$ . A diagonal line indicates the expected dependency.

[2.10](#) relates the distance between pore centers and given sphere centers,  $\|\mathbf{c}^{\text{pore}} - \mathbf{c}^{\text{sphere}}\|_2$ , to the difference between radii,  $r^{\text{pore}} - r^{\text{sphere}}$ .

## Discussion

The following observations can be made with the help of the hcp data set:

- Measured pore radii in [fig. 2.9](#) (left) are always lower than the ground truth. However, [Fig. 2.10](#) shows that the measurement error is not due to shortcomings of the algorithm, but due to the discretization of the distance field: If the distance between (integer valued) pore centers  $\mathbf{c}^{\text{pore}}$  is close to the (real valued) sphere centers  $\mathbf{c}^{\text{sphere}}$ , then  $r^{\text{pore}} - r^{\text{sphere}}$  is close to 0.

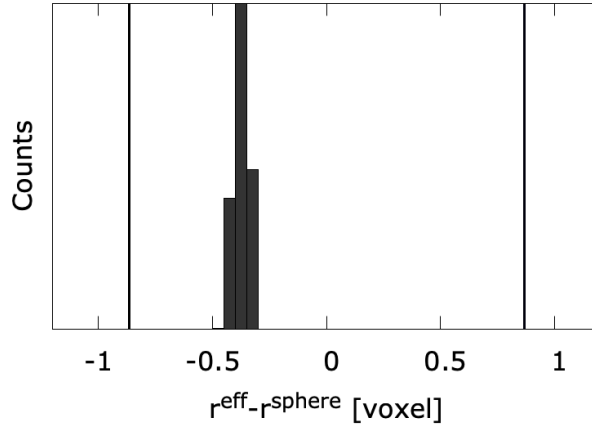


**Fig. 2.11** The effective radius  $r^{\text{eff}}$  is obtained by voxel counting. Compare to fig. 2.9 (left).

- For the same reason, throat radii are always measured larger than the reference circle radius (fig. 2.9).
- The close proximity of the points and the diagonal line in fig. 2.10 confirms precision of the mMBa: Label propagation in the algorithm relies on precise (discrete) distant field values.

The validation showed that the distance field is precise, but suffers from discretization. Detected pore radii in fig. 2.9 (left) vary within 1 voxel.

It is possible obtain pore radii in another way: Pore volumes are determined by voxel counting, and effective radii  $r^{\text{eff}}$  are calculated from the pore volumes (eq. 2.19). The effective radius has a much lower variation than the radius obtained from the distance field (fig. 2.11). Again,  $r^{\text{eff}}$  is always smaller than the input sphere radius, which can be explained as follows: Each pore has 12 connections to its neighbors. Therefore, several spherical caps are missing from each pore volume. The effect of spherical caps can be quantified, using the spherical cap volume formula (Weisstein, 2019):

$$V^{\text{cap}} = \pi h^2(3r - h)/3 \quad (2.29)$$

where  $r^{\text{sphere}}$  is abbreviated as  $r$ , and  $h$  is the height of the cap. Given the parameters of the sphere pack, it follows that  $h/r = 0.05$ . Since each sphere in the packing has 12 neighbors, the caps reduce the sphere volume as follows:

$$\begin{aligned} V^{\text{reduced}} &= V^{\text{sphere}} - 12 V^{\text{cap}} \\ &= V^{\text{sphere}}(1 - (h/r)^2(3 - h/r)) \\ &\approx 0.978 V^{\text{sphere}} \end{aligned} \quad (2.30)$$

Plugging in the sphere radius, which is around 13.4 voxels, the effect of spherical caps onto the effective radius is

$$r^{\text{sphere}} - r^{\text{reduced}} \approx (1 - 0.978^{1/3})r^{\text{sphere}} \approx 0.0993 \text{ voxels} \quad (2.31)$$

Altogether, the spherical caps which are missing from the pore volume account to a reduction of the measured radius by 0.1 voxels, compared to the input sphere radius.

The spherical caps alone cannot explain the discrepancy between  $r^{\text{eff}}$  and  $r^{\text{sphere}}$ , which is between 0.3 and 0.5 voxels (fig. 2.11). However, the throats, which are membranes of 1 voxel thickness, were not considered in the above discussion. In the validation data set, throats are circular voxel disks with radius  $r^{\text{circle}}$ , as described above. Subsequently,  $V^{\text{circle}}$  is

$$V^{\text{circle}} = \pi (r^{\text{circle}})^2 = \pi((r^2 - (r/1.05)^2) \quad (2.32)$$

again,  $r^{\text{sphere}}$  is abbreviated by  $r$ . Keeping in mind that each throat is shared by two pores, the calculated effective pore volume is

$$V^{\text{eff, calculated}} = V^{\text{sphere}} - 12 V^{\text{cap}} - 6V^{\text{circle}} \quad (2.33)$$

and subsequently

$$r^{\text{sphere}} - r^{\text{eff, calculated}} \approx 0.242 \text{ voxels} \quad (2.34)$$

Calculating the effects of sphere caps and throat voxels cannot fully reproduce the finding that  $r^{\text{sphere}} - r^{\text{eff}}$  is between 0.3 and 0.5 voxels (fig. 2.11). However, the discussion shows that the geometric objects which were used as input (the spheres) can be rediscovered up to a small difference, if their mutual overlap is small. The ellipsoidal bubbles which make up the physical foam which is analyzed later have such small overlaps (this can be seen in fig. 2.13 and fig. 2.14, and will also be validated in section 3.2).

## Comparison to Literature

Silin and Patzek (2006) use voxelized regular sphere packings for verification of their algorithm. In contrast to this thesis, the sphere pack represents the material phase. Subsequently, the space which is segmented lies between the packed spheres. The authors voxelize the sphere pack with different resolutions. They note that the resolution should be a factor of 10 higher than the representative sphere radius in order to obtain meaningful results.

Dong and Blunt (2009) use the void space between a regular sphere packings as a verification for their algorithm. The theoretical number of pores (which do not intersect the data set boundary) matches the number of pores which is found by their algorithm.

Gostick (2017) uses a regular sphere pack to demonstrate that pure watershed segmentation is sufficient for very simple geometries. The authors then proceeds with more complicated artificial geometries, which motivate additional algorithmic steps for proper segmentation.

In this thesis, carbon foam is discussed, which has a void space that resembles packed spherical bodies. In contrast, the real world structures which are of interest for the above authors have a low porosity, and void space is more similar to the space between the packed spheres.

The regular sphere packing in this thesis is used to discuss effects of subvoxel accuracy. In contrast, the above authors limit regular sphere packings for baseline checks of their segmentation algorithms.

### 2.3.2 Irregular Polydisperse Sphere Pack

The second artificial data set is a coverage representation as well, i.e., each voxel value is proportional to the amount of material it contains, the material fraction is sampled from  $8 \times 8 \times 8$  points per voxel.

Sphere centers are placed irregularly, and spheres of different radii are present, which is called polydispersity. Inside a cubic region with side length  $L = 128$  voxels, 32 spheres with radius 16.0 are sequentially added as void space. Center positions are random (in  $\mathbb{R}^3$ ), with the constraint that each sphere has at most 10 % overlap with previously created void space. Next, twice as many spheres with half the radius are added in the same manner. The procedure is repeated, and finishes after 1024 spheres with radius 0.5 are added.

## Results

After mMBa segmentation of the artificial data set, the given sphere size distribution is matched to the segmentation, see table 2.1. Each sphere can be classified into one of the following categories:

- Material: If the ground truth pore size is smaller than the voxel size, then it might not change the gray value of the coverage representation below the segmentation threshold. The pore is not detected in this case
- Boundary pore: Not considered for mMBa statistics, as described before (section 2.1.3)
- Merged pore: According to equation 2.18, small pores might merge into larger ones.

$r^{\text{sphere}}$	0.5	1.0	2.0	4.0	8.0	16.0
Material	991	0	0	0	0	0
Boundary pore	0	44	27	25	17	21
Merged into other pore	21	85	40	11	0	0
Pore	12	383	189	92	47	11
Sum	1024	512	256	128	64	32

**Table 2.1** Segmentation result for second artificial data set. The first row gives the radius of each sphere species. Following rows show how the mMBa interpreted the ground truth.

- Pore: Spheres from the ground truth which are successfully detected as pores.

A summation in the last line of the table confirms that all ground truth spheres are included in the analysis.

## Discussion

Table 2.1 provides the following insights:

- Nearly all spheres with  $r^{\text{sphere}} = 0.5$  cannot be detected by the mMBa. This is expected: If a sphere is located exactly at the voxel center, then it fills 52.4 % of the voxel cell, and can be detected in a true coverage representation. If the sphere center is slightly shifted, then the sphere will partially cover several voxels, leading to a minority of void space in each voxel cell, and subsequently no detection. More generally, the failure to detect sub-voxel structures is a consequence of the Nyquist-Shannon sampling theorem (Jerri, 1977).
- For  $r^{\text{sphere}} = 4.0$ , around 10 % of pores merge. For  $r^{\text{sphere}} = 2.0$  and  $r^{\text{sphere}} = 1.0$ , it is 20 %. Increased merging for small sphere radii can be explained by voxelization. If a pore with small  $r^{\text{eff}}$  intersects another one, the physical ground truth (sharp defined edge) is smoothed due to the coverage representation, resulting in high ratios  $r^{\text{throat}}/r^{\text{pore}}$ , and subsequently to merging, according to equation 2.18. A more extensive discussion of edges in coverage representations is given by Arand and Hesser (2017).
- Around 2/3 of pores with  $r^{\text{pore}} = 16.0$  coincide with the data set boundary. The high ratio of boundary pores agrees with the previously established relationship for (non-) boundary pores, eq. 2.25. For  $r = 16$ , the expected value for boundary spheres, given 32 randomly place spheres, is  $E(N_{\text{boundary}}) = 18.5$ , which is close to the measured value  $N_{\text{boundary}} = 21$ .

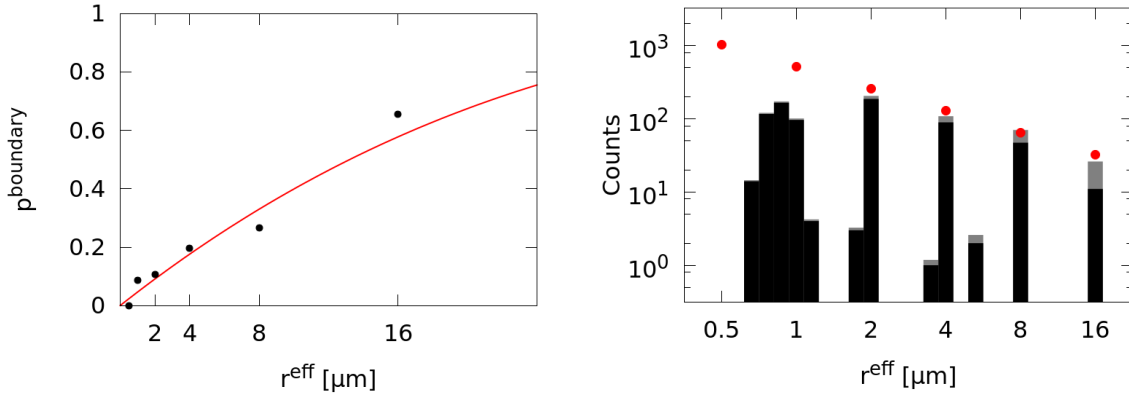


**Fig. 2.12 Left:** Red line: Probability of finding a boundary pore with radius  $r^{\text{eff}}$  (see eq. 2.26). Dots: relative ratio of detected boundary pores and given spheres. **Right:** Histogram for measured pore sizes (black bars). Grey bars show the estimated ground truth, based on the measured pore counts and using the boundary effect equation (2.26). Red dots show the actual number of spheres, used for creation of the data set.

The last point, i.e., the boundary effect, is visualized in fig. 2.12 (left). Furthermore, the right figure shows how the ground truth can be estimated, using only information obtained from automatic segmentation. It can be seen that the input distribution can be approximately reproduced for  $r \geq 2$ .

In summary, validation (see also Arand and Hesser, 2017) shows that the mMBA is well-suited for the desired segmentation of the carbon foam sample. The following limitations were identified: First, structures smaller than the resolution limit cannot be resolved. Second, near the resolution limit, the mMBA tends to merge small pores into neighboring pores due effects of the coverage representation. Third, data set boundaries have a significant effect on statistics, if pores are not small compared to the data set size:

$$r^{\text{eff}}/L > 0.01 \quad \Rightarrow \quad p^{\text{boundary}}(r^{\text{eff}}, L) > 0.05 \quad (2.35)$$

### Comparison to Literature

Homberg, Baum, et al. (2014) use a polydisperse sphere pack as voxelized material, and the areas in between as void space, in order to test their segmentation algorithm. The authors find that their reference pore centers are matched by the segmented ones closely.

Gostick (2017) uses a 2D disk packing to demonstrate how the segmentation algorithm works. The packing contains disks of constant radius, which are placed at random positions, overlap is allowed. Different steps of the algorithm are related to changes in the 2D segmentation. The author also uses the disk packing to tune parameters of the algorithm.

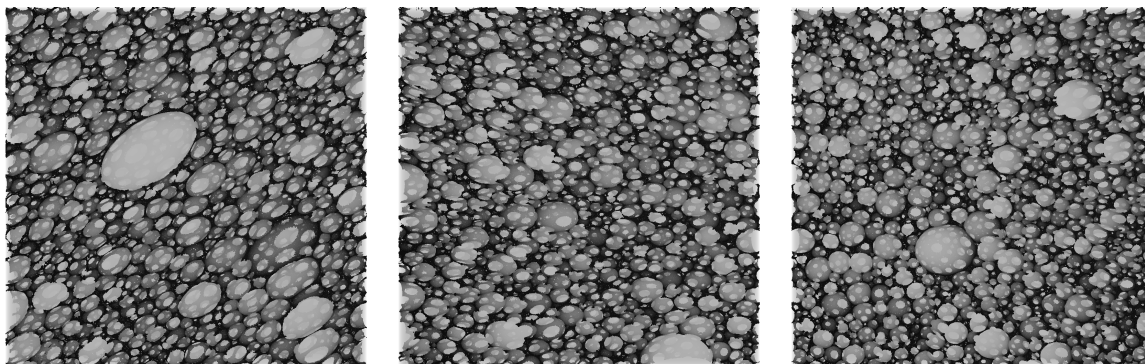


**Fig. 2.13** Renderings of the CT scan from three different sides, where artificial fog was added for better depth perception. **Left:** View from top (xy-plane) **Middle:** View from front (xz-plane) **Right:** View from right (yz-plane)

In this thesis, the polydisperse sphere packing is used to understand merging behavior, boundary effects, and limitations of voxel resolution. Pore matching is done similarly to Homberg, Baum, et al. (2014). In contrast to Gostick (2017), the mMBa is not tuned with the help of artificial data sets. Tuning might help to avoid effects such as unwanted merging of pores. Although the mMBa merging parameter (eq. 2.18) is not further discussed in this thesis, its choice gives pore statistics that agree with other segmentation methods (Arand and Hesser, 2017). It should be noted that parameter tuning with artificial data sets might also be a disadvantage, because the artificial data sets might represent irrelevant corner cases.

## 2.4 Statistics of Carbon Foam Sample

A carbon foam data set (“the sample”, fig. 2.13) is analyzed according to methods described in section 2.1, i.e., with respect to polydispersity and anisotropy of pores, and wall thickness. The workflow was done similarly by Arand and Hesser (2018). Functions are fitted to the found statistics. Fitted functions will serve as input for foam model creation in the next chapter.

### 2.4.1 Pore Size Distribution

Schunck GmbH provided a sample of their foam FU4545, and the German Institute of Textile and Fiber Research Denkendorf (DITF) made a CT scan thereof. The resulting data set has a resolution of  $1\ \mu\text{m}/\text{voxel}$ , and is of size  $3052 \times 3052 \times 2400$  voxels, i.e.,  $3.05 \times 3.05 \times 2.40\ \text{mm}^3$ . Near the edges of the data set, an increased amount of artifacts appear, resulting from CT reconstruction. Therefore, only the central region of size  $2000 \times 2000 \times 2000$  voxels is analyzed. The central region is called  $\mathcal{R}_{\text{large}}$ , it is rendered in fig. 2.13.

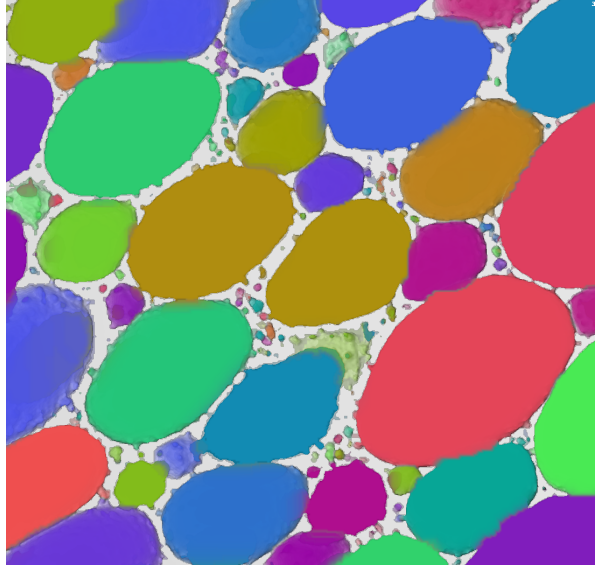


**Fig. 2.14** Rendering of automatically segmented volume.

$\mathcal{R}_{\text{large}}$  is preprocessed as described in section 2.1.1, i.e., the data set is denoised, and free floating material voxels are removed. In order to save computer memory (RAM) and time, 8 equally sized subregions of  $\mathcal{R}_{\text{large}}$  with half the side length are analyzed,  $\mathcal{R}_1, \dots, \mathcal{R}_8$ . Next, in order to process  $\mathcal{R}_{\text{large}}$  for large scale statistics, it is downsampled: Each block of  $2 \times 2 \times 2$  voxels is averaged, resulting in a volume of size  $1000 \times 1000 \times 1000$  voxels (resolution:  $2 \mu\text{m}/\text{voxel}$ ). The modified Maximal Ball algorithm is used for automatic segmentation of all data sets, see fig. 2.14.

## Results

Histograms with logarithmic bin widths (equation 2.20) are created for effective pore radii,  $r^{\text{eff}}$  (equation 2.19). For the subregions  $\mathcal{R}_1, \dots, \mathcal{R}_8$ , all histograms are summed up, and compared to the histogram obtained from  $\mathcal{R}_{\text{large}}$ . Histograms can be found in fig. 2.15. They are called  $h_{\text{summed}}$  and  $h_{\text{large}}$ , respectively.

## Discussion

Several conclusions can be drawn from fig. 2.15:

- Below  $r^{\text{eff}} \approx 1$  voxel, the histograms cannot provide meaningful information. This is due to previously discussed limitations of the segmentation algorithm, see section 2.3.2. Voxel size differs by a factor of 2 between  $\mathcal{R}_1, \dots, \mathcal{R}_8$  and  $\mathcal{R}_{\text{large}}$ . Therefore, when comparing  $h_{\text{summed}}$  and  $h_{\text{large}}$ , the occurrence of small scale effects has an offset.

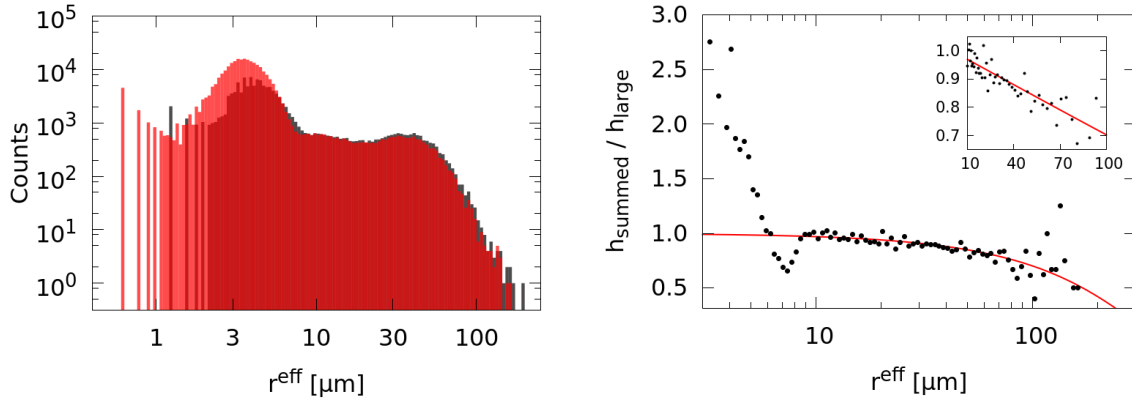


**Fig. 2.15 Left:** Pore size statistics, as found by segmentation algorithm. Grey: Statistics for  $\mathcal{R}_{\text{large}}$ . Red: Combined statistics of  $\mathcal{R}_1, \dots, \mathcal{R}_8$ . **Right:** Dots: Ratio of histogram heights,  $h_{\text{summed}}/h_{\text{large}}$ . A red line indicates the ratio  $p(r^{\text{eff}}, 1000 \mu\text{m})/p(r^{\text{eff}}, 2000 \mu\text{m})$ , where  $p(r^{\text{eff}}, L)$  is the probability for a pore to be entirely inside the analysis region, see equation 2.26. The small inlet window with linear abscissa shows the range  $10 \mu\text{m} \leq r^{\text{eff}} < 100 \mu\text{m}$ .

- In the left figure, the region  $r^{\text{eff}} < 10 \mu\text{m}$  differs significantly between  $h_{\text{summed}}$  and  $h_{\text{large}}$ . As explained in section 2.3.2, downsampling of  $\mathcal{R}_{\text{large}}$  leads to smoothing of structures, resulting in larger throats, and subsequently an increased merging ratio from small pores into large ones.
- For  $r^{\text{eff}} \geq 10 \mu\text{m}$ , a good agreement is found between cumulative statistics of the 8 subregions, and  $\mathcal{R}_{\text{large}}$ . Additionally, the right figure confirms the validity of the boundary effect formula (equation 2.26), which is indicated by a red line.
- A steep decrease of pore occurrence for  $r^{\text{eff}} \geq 30$  indicates that there is an upper limit to pore sizes. In particular, the decrease is much stronger than it is expected from boundary effects. The physical upper bound for pore sizes is therefore estimated to be  $r^{\text{eff}} < 200 \mu\text{m}$  (although, in theory, most size distributions do not have an upper bound). Inside  $\mathcal{R}_{\text{large}}$ , the largest pore has  $r^{\text{eff}} \approx 160 \mu\text{m}$ .

Using insights of the discussions, the actual pore size distribution is approximated by lognormal distributions. By doing so, it will be possible to tune the digital model of the foam with a limited set of parameters.

For further evaluations, the two histograms are combined, denoted as  $h_{\text{combined}}$ . The combined histogram consists of  $h_{\text{summed}}$  for  $r^{\text{eff}} < 10 \mu\text{m}$ , and of  $h_{\text{large}}$  for  $r^{\text{eff}} \geq 10 \mu\text{m}$ . Bin heights are corrected according to equation 2.26, in order to account for boundary effects. Finally, the sum of three Gaussian distributions is fitted to  $h_{\text{summed}}$ , where where  $x$ -values correspond to  $\log_{10}(r^{\text{eff}})$ , and  $y$ -values correspond to histogram heights. The result can be seen in table 2.2 and fig. 2.16.

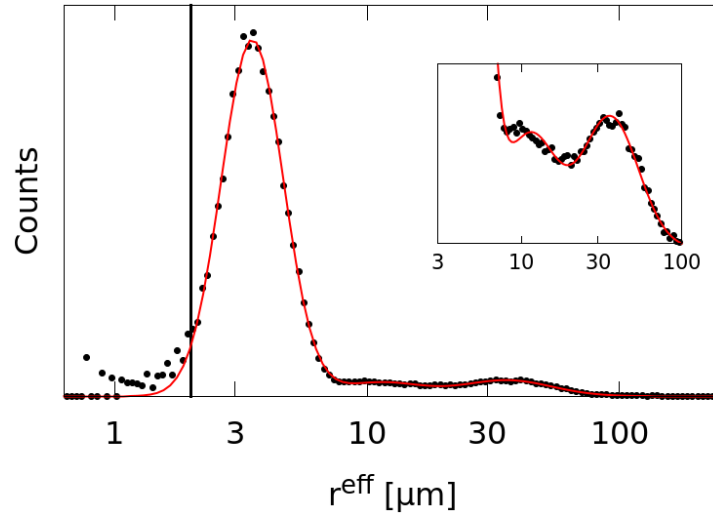


**Fig. 2.16** The sum of three Gaussians (red line), fitted to  $h_{\text{combined}}$  (black dots). Values smaller than  $2\mu\text{m}$  are ignored (vertical line, large graph). A small inlet window shows more details for the second and third peak.

$A$	4916.02	255.149	313.502
$\mu$	0.545511	1.05489	1.55488
$\sigma$	0.122803	0.165258	0.175474

**Table 2.2** Fitted parameters of Gaussians: Amplitude  $A$ , mean  $\mu$  and standard deviation  $\sigma$ . Peak locations in physical units can be obtained from means of the fitted Gaussians ( $10^\mu$ ): They are  $3.51\mu\text{m}$ ,  $11.3\mu\text{m}$ , and  $35.9\mu\text{m}$ .

## Comparison to Literature

Statistical analysis of pore space is an important tool in digital rock physics, as can be seen in the summary below. First, obtained statistics differ for different kinds of rock, and are correlated with physical properties of the specimen. Second, statistics serve as a good way to validate algorithms, and to discuss differences between them

- Al-Kharusi and Blunt (2007) compare pore size statistics of Fontainebleau sandstone obtained with their Maximal Ball algorithm to pore size statistics obtained with an algorithm by Øren and Bakke (2003).
- Dong and Blunt (2009) also compare results of their version of the MBa to the results of Øren and Bakke (2003). Two kinds of rocks are compared: Fontainebleau sandstone and Berea sandstone. In addition to pore size statistics, the authors compare coordination numbers, throat radii, and shape factors.
- Rabbani, Jamshidi, and Salehi (2014) compare their watershed based segmentation method with respect to coordination numbers to Dong and Blunt (2009). Coordination numbers are calculated for a Berea and a Carbonate sample.
- Gostick (2017) also compares his algorithm to the MB algorithm by Dong and Blunt (2009) with respect to pore and throat size statistic, and coordination numbers.
- Arand and Hesser (2017) compare the mMBa for a Berea sandstone to the results obtained by Dong and Blunt (2009), with respect to the number of pores and throats, and the average coordination number.

In this thesis, statistical analysis serves a different purpose: Pore sizes are extracted in order to have an input distribution for the foam model. Other publications which are related to carbon foam modeling obtain input distributions in different ways:

- Kirca et al. (2007) use scanning electron microscopy (SEM) images to specify the smallest and largest pore size. The authors do not provide these sizes to the reader, they also do not specify the kind of statistical distribution which they use as input for their sphere-based carbon foam model.
- Dyck and Straatman (2015) model their foam with spheres from a normal distribution. According to the authors, parameters of the distribution are taken from Klett, McMillan, et al. (2004), although the cited paper does not provide these values (the cited authors only mention that “[t]he foam typically exhibits uniformly shaped bubbles with a normal

distribution”). For the normal distribution, Dyck and Straatman (2015) choose a mean of  $400\mu\text{m}$  and a standard deviation of  $120\mu\text{m}$ . In contrast, all pores which are detected in the foam sample of this thesis are smaller than  $200\mu\text{m}$ . The majority of pores can even be found at an order of magnitude between  $1\mu\text{m}$  and  $10\mu\text{m}$ . Furthermore, quantitative analysis in this thesis shows that pore sizes of the investigated sample are distributed lognormally.

## 2.4.2 Anisotropy of Pores

Qualitatively, pore anisotropy of the sample can be seen in fig. 2.13. In particular, in the left figure, which corresponds to the view perpendicular to the  $xy$ -plane, orientation and deformation of pores is visible. Quantitative discussion of anisotropy follows.

### Results

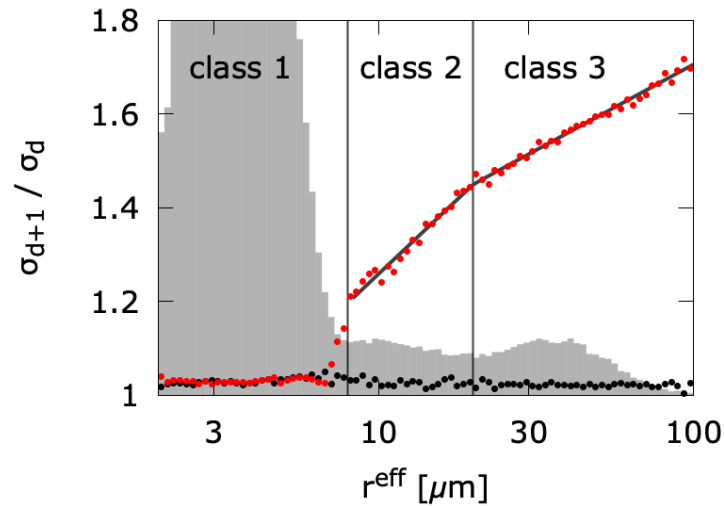
As described in section 2.1.3, an average covariance matrices  $\langle \Sigma \rangle$  is calculated for each subset of pores with similar size (same bin in logarithmic histogram). Next,  $\langle \Sigma \rangle$  is decomposed into orthonormal eigenvectors  $\langle \mathbf{v}_d \rangle$ , (eq. 2.23) and eigenvalues  $\langle \lambda_d \rangle = \langle \sigma_d \rangle^2$  (eq. 2.24), with  $d \in \{1, 2, 3\}$ .

Fig. 2.17 shows the ratios  $\langle \sigma_3 \rangle / \langle \sigma_2 \rangle$  and  $\langle \sigma_2 \rangle / \langle \sigma_1 \rangle$  as a function of  $r^{\text{eff}}$ . In fig. 2.18, projections onto coordinate planes are employed to evaluate the orientation of eigenvectors  $\langle \mathbf{v}_3 \rangle$ . These eigenvectors correspond to the largest eigenvalue  $\lambda_3 = \langle \sigma_3 \rangle^2$ . In both figures, values are restricted to  $r^{\text{eff}} \geq 2\mu\text{m}$ , in order to avoid artifacts coming from voxelization, and to  $r^{\text{eff}} < 100\mu\text{m}$  to have sufficient statistics.

### Discussion

From fig. 2.17, the following observations can be made:

- The ratio  $\langle \sigma_2 \rangle / \langle \sigma_1 \rangle$  stays constant across the entire scale,  $\langle \sigma_2 \rangle / \langle \sigma_1 \rangle \approx 1$ .
- For  $r^{\text{eff}} < 8\mu\text{m}$ , on average, pores are spherical: It approximately holds that  $\langle \sigma_1 \rangle : \langle \sigma_2 \rangle : \langle \sigma_3 \rangle = 1 : 1 : 1$ .
- Pores are “cigar-shaped” for  $r^{\text{eff}} \geq 8\mu\text{m}$ : The two smaller axis are equal,  $\langle \sigma_1 \rangle \approx \langle \sigma_2 \rangle$ . In contrast, there is a relative increase of  $\langle \sigma_3 \rangle / \langle \sigma_2 \rangle > 1$  as  $r^{\text{eff}}$  becomes larger.
- A comparison between the histogram and ratios  $\langle \sigma_3 \rangle / \langle \sigma_2 \rangle$  indicates a relation between intervals defined by distribution peaks and pore shapes. Subsequently, three classes can be identified: Class 1 has  $r^{\text{eff}} < 8\mu\text{m}$ , with spherical pores. Class 2 has  $8\mu\text{m} \leq r^{\text{eff}} < 20\mu\text{m}$ ,



**Fig. 2.17** Ratios of axes  $\langle \sigma_3 \rangle / \langle \sigma_2 \rangle$  (red dots) and  $\langle \sigma_2 \rangle / \langle \sigma_1 \rangle$  (black dots), as a function of effective radius. In the background, the pore size histogram serves as an orientation. Two vertical lines at  $8 \mu\text{m}$  and  $20 \mu\text{m}$  divide pores into three classes.

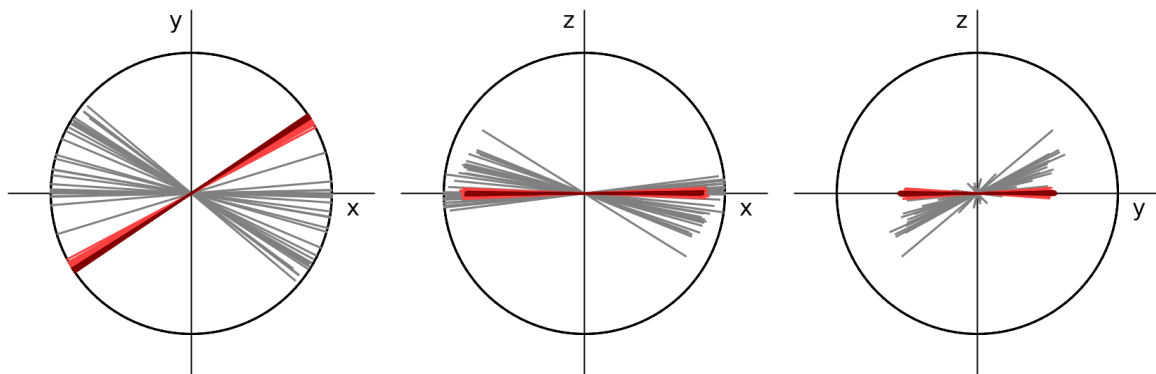


**Fig. 2.18** Projections of eigenvectors  $\pm \langle \mathbf{v}_3 \rangle$  onto coordinate system planes. Grey circles of radius 1 indicate the maximum projection length. Following the class subdivision in fig. 2.17, gray projections correspond to the left class, light red projections correspond to the middle class, and dark red projections correspond to the right class. Pore orientation can also be seen qualitatively in fig. 2.13.

where “cigar-shapedness” increases with  $r^{\text{eff}}$ . Class 3 has  $r^{\text{eff}} \geq 20 \mu\text{m}$ . Similar to the previous class,  $\langle \sigma_3 \rangle / \langle \sigma_2 \rangle$  increases with  $r^{\text{eff}}$ , but with a smaller slope.

Following the discussion, in classes 2 and 3, a pair of lines is fitted from  $x = \log_{10}(r^{\text{eff}})$  to  $\langle \sigma_3 \rangle / \langle \sigma_2 \rangle$ :

$$f_{\sigma}(x) = A + B(x - s) \mathbb{1}_{x < s} + C(x - s) \mathbb{1}_{x \geq s} \quad (2.36)$$

where  $s = \log_{10}(20)$  is the class separator,  $\mathbb{1}$  is the indicator function (which is 1 if the subscript condition is fulfilled, and 0 otherwise), and  $A, B, C$  are the fit variables. As a result, the following values are found:  $A = 1.45$ ,  $B = 0.636$  and  $C = 0.366$ .

For all pore sizes,  $\langle \sigma_1 \rangle \approx \langle \sigma_2 \rangle$ . Thus, orientation of pores is determined by  $\mathbf{v}_3$ . The following can be deduced from fig. 2.18:

- Pores with  $r^{\text{eff}} \geq 8 \mu\text{m}$  are oriented perpendicular to the  $z$ -axis/ aligned with the  $xy$ -plane.
- Pores from classes 2 and 3 are oriented parallel to each other with close to no variation.
- For  $r^{\text{eff}} < 8 \mu\text{m}$ , pores are nearly spherical. Still, another preferred direction can be seen, although variation is larger, compared to  $r^{\text{eff}} \geq 8 \mu\text{m}$ .

Similarly to pore elongation, a quantitative value for pore orientation is determined. For subsequent modeling, pores with  $r^{\text{eff}} < 8 \mu\text{m}$  will be idealized as spheres. Pores with  $r^{\text{eff}} \geq 8 \mu\text{m}$  will be idealized as cigar-shaped ellipsoids, perpendicular to the  $z$ -direction, which are rotated by an angle  $\phi$  from the  $x$ -axis, see fig. 2.19. Similar to (2.36), rotation is fitted to be

$$f_{\phi}(x) = A + B(x - s) \mathbb{1}_{x < s} + C(x - s) \mathbb{1}_{x \geq s} \quad (2.37)$$

with  $A = 32.8$ ,  $B = 8.75$ , and  $C = 1.45$ .

### Comparison to Literature

Anisotropy of foam can be obtained with methods other than the analysis of pores: Jang, Kraynik, and Kyriakides (2008) study polyurethane foam and aluminum foam in detail, using micro CT. The authors measure the lengths distribution of cell ligaments. As a result, average cell elongations are given as a function of the position along the main axis. Furthermore, ligament cross sectional areas are measured against axial positions.

Benouali et al. (2005) analyze pore orientations inside aluminum foam, and use methods which have similarities with this thesis. The authors first segment a CT data set of the foam with a watershed algorithm. Then, the authors take different cross-sections of the data set.

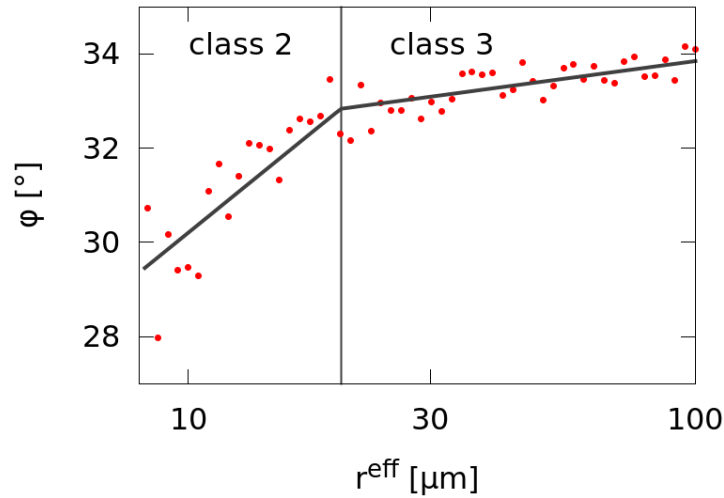


**Fig. 2.19** Rotation angle  $\phi$  in the  $xy$ -plane, as a function of effective radius (red dots). The vertical bar is located at  $r^{\text{eff}} = 20 \mu\text{m}$ . Similar to fig. 2.17, a pair of lines (black) is fitted to the points.

Inside each cross-section, a best-fit (2D) ellipse is related to the position along the data set axis. Next, the authors analyze large pore bodies (around 500), and find equivalent ellipsoids for them. Histograms are given for the three ellipsoid axes lengths. However, the correlation of axes lengths with each other is lost, in contrast to the analysis which is used in this thesis (fig. 2.17). Benouali et al. (2005) visualize orientations of the ellipsoids with scatter plots: Both end points of each ellipsoid axis are projected onto the coordinate planes, which has similarities to fig. 2.18. It is possible to see a preferred orientation in the scatter plots, however, since orientations are not statistically averaged, a high variance can be seen in the plots.

Both publications which are discussed above, Jang, Kraynik, and Kyriakides (2008) and Benouali et al. (2005), compare morphological properties to positions along the data set axis. This is not done in the thesis, mainly because spatial correlations are not incorporated in the digital foam model (see chapter 3).

The advantages of averaged covariance matrices  $\langle \Sigma \rangle$  become apparent when comparing this thesis to Benouali et al. (2005). If pores are binned, for example according to size or according to position in the data set, then each binned set of pores can be treated as a single statistical ellipsoid with covariance matrix  $\langle \Sigma \rangle$ . Changes in the statistical ellipsoid as a function of quantities such as size or position may then lead to insights about the analyzed sample. In contrast, properties of statistical (2D) ellipses depend on the orientation of the coordinate system.

# Chapter 3

## Digital Modeling of Carbon Foam

Carbon foam has previously been modeled digitally, see section 1.3.2. Models were of increasing complexity, starting with unit cell approaches, finishing with modeling of void space as polydisperse sphere packs. In this thesis, an additional layer of complexity is added to modeling, leading to a void space morphology that matches its real world sample more closely: Void space is approximated using ellipsoids of varying size and shape. The approach is described in detail at this point. It can be considered as an extension and update of a previous publication (Arand and Hesser, 2018). The resulting digital carbon foam will be called “the model”.

### 3.1 Methods

Before describing the modeling process, an ellipsoid  $\mathcal{E}$  is defined as follows:

$$\mathbf{x} \in \mathcal{E} : (\mathbf{x} - \mathbf{c})^T \mathbf{E} (\mathbf{x} - \mathbf{c}) \leq 1 \quad (3.1)$$

where

$$\mathbf{E} = \mathbf{R} \mathbf{A}^{-2} \mathbf{R}^T \quad (3.2)$$

and  $\mathbf{R}$  contains the ellipsoid axes directions as column vectors, and  $\mathbf{A}$  is a diagonal matrix that contains the axes lengths  $(a, b, c)$ , such that  $\mathbf{A}^{-2} = \text{diag}(1/a^2, 1/b^2, 1/c^2)$ . It should be noted that  $\mathbf{R}$  consists of orthonormal vectors, and can be seen as a rotation matrix, similar to the previously discussed principal component analysis (2.22).

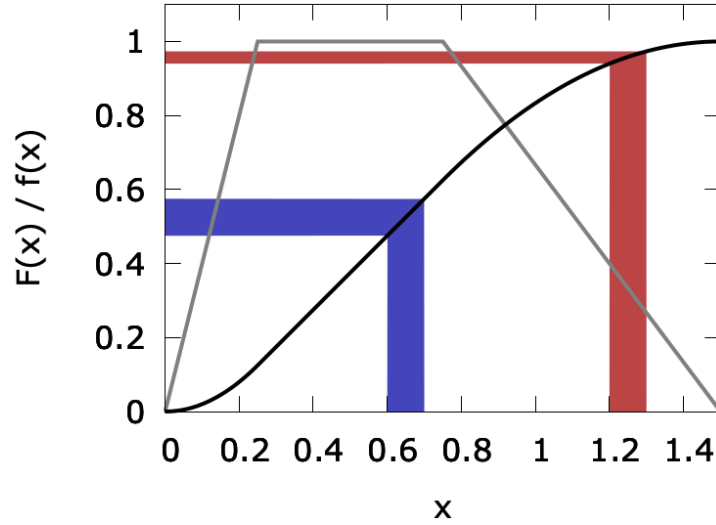


**Fig. 3.1** Visual explanation of inverse transform sampling. The probability density function  $f(x)$  is in the background (gray), the cumulative distribution function  $F(x)$  in the foreground (black). Example intervals are given in blue and red. Given an interval  $[a, b]$ , the probability  $p_f(a \leq x \leq b)$  is given by  $F(b) - F(a)$ . This is equal to  $p_u(F(a) \leq y \leq F(b))$ , where  $u(y)$  is the p.d.f. of the uniform random variable on the interval  $[0, 1]$ .

### 3.1.1 Sampling of Ellipsoids

Ellipsoids sizes of the model obey an input probability density function (p.d.f.)  $f(x)$ , which has the following properties:

- $f(x) \geq 0$
- $\int_{-\infty}^{\infty} f(x) dx = 1$
- $p_f(x < a) = \int_{-\infty}^a f(x) dx = F(a)$

where  $p_f(\cdot)$  gives a probability, and  $F(x)$  is the cumulative distribution function (c.d.f.).

Now, ellipsoid sizes  $x \equiv \log_{10}(r^{\text{eff}})$  can be sampled from the previously determined distribution (fig. 2.16, table 2.2). Given the random variable  $X$ , and its inverse c.d.f.,  $F^{-1}(y) = x$ , it can be shown that the random variable  $F^{-1}(U_{[0,1]})$  has the same distribution as  $X$  (Devroye, 1986), where  $U_{[0,1]}$  is the uniform random variable on the interval  $[0, 1]$ . A visual explanation can be found in fig. 3.1.

In order to obtain a large number of samples,  $F^{-1}(y)$  is discretized and calculated recursively:

---



---

```

1:  $F^{-1}[]$  ▷ Discretized version of  $F^{-1}(y)$ , size:  $N$ 
2:  $Y_{\min} = 0$ 
3:  $Y_{\max} = N - 1$ 
4:  $F^{-1}[Y_{\min}] \leftarrow x_{\min}$  ▷  $x_{\min} = \log_{10}(1.0)$ , smallest meaningful radius (section 2.3.2)
5:  $F^{-1}[Y_{\max}] \leftarrow x_{\max}$  ▷  $x_{\max} = \log_{10}(200.0)$ , largest expected radius (section 2.4.1)
6: fill_f_inv_recursive( $Y_{\min}$ ,  $Y_{\max}$ )
7: return  $F^{-1}[]$ 

```

---



---



---

```

1: function FILL_F_INV_RECURSIVE( $Y_{\min}$ ,  $Y_{\max}$ )
2:
3:    $x_{\text{middle}} = (F^{-1}[Y_{\min}] + F^{-1}[Y_{\max}])/2.0$ 
4:    $Y_{\text{middle}} = \lfloor N \cdot F(x_{\text{middle}}) \rfloor$  ▷  $\lfloor \cdot \rfloor$  is the floor function
5:    $F^{-1}[Y_{\text{middle}}] = x_{\text{middle}}$ 
6:
7:   if  $Y_{\min} + 1 < Y_{\text{middle}}$  then
8:     fill_f_inv_recursive( $Y_{\min}$ ,  $Y_{\text{middle}}$ )
9:
10:  if  $Y_{\text{middle}} + 1 < Y_{\max}$  then
11:    fill_f_inv_recursive( $Y_{\text{middle}}$ ,  $Y_{\max}$ )

```

---

The function `fill_f_inv_recursive`( $Y_{\min}$ ,  $Y_{\max}$ ) needs to evaluate the c.d.f. of the pore radii,  $F(x)$ , in line 4. It should be noted that  $F(x)$  can be trivially constructed from the sum of the three Gaussian distributions (fig. 2.16, table 2.2), knowing that

$$f(x) = N(x, \mu, \sigma) \Leftrightarrow F(x) = \frac{1}{2} \left( 1 + \operatorname{erf} \left( \frac{x - \mu}{\sigma \sqrt{2}} \right) \right) \quad (3.3)$$

where the error function  $\operatorname{erf}(x)$  can be taken from any math library. Finally, values can be sampled as  $x_{\text{sample}} = F^{-1}[N \cdot \operatorname{rand}(0, 1)]$ , where  $\operatorname{rand}(0, 1)$  gives a random number from the interval  $[0, 1)$ . Effective ellipsoid radii are then  $r^{\text{eff}} = 10^x \mu\text{m}$ . If sampled pores have radii  $r^{\text{eff}} \geq 8 \mu\text{m}$ , then they are modeled as cigar-shaped ellipsoids, i.e., their elongation and orientation are set according to the fits in equations (2.36) and (2.37).

### 3.1.2 Foaming Heuristic for Large Pores

Pore space creation in the model is divided into two steps: Large pores ( $r^{\text{eff}} \geq 8 \mu\text{m}$ ) are arranged using so-called time-driven molecular dynamics (in contrast to event-driven molecular

dynamics, see Donev, Torquato, and Stillinger (2005a)). Small pores are added to the remaining material using random sequential addition (Torquato, Uche, and Stillinger, 2006).

Choosing different methods for small and large pores is motivated as follows: Of the total void space with porosity  $\phi \approx 90\%$ , pores with  $r^{\text{eff}} < 8\ \mu\text{m}$  occupy a small fraction,  $\phi_{\text{small}}/\phi \approx 1\%$ . According to (Torquato, Uche, and Stillinger, 2006), random sphere configurations with low saturation densities ( $\phi < 38\%$ ) can be created by randomly adding spheres to space. If  $\phi > 38\%$ , then more elaborate methods are required. Therefore, since  $\phi \gg 38\%$  for  $r^{\text{eff}} \geq 8\ \mu\text{m}$ , a more sophisticated method is used, which is described in the following paragraphs.

After configuration of large pores, small pores are added to the remaining material using random sequential addition, since  $\phi_{\text{small}}/(1 - \phi) \approx 10\% < 38\%$ .

### Motivation for Heuristic Approach

Simulating the complex physical process of anisotropic bubbling is out of scope of this work. Instead, the goal is to achieve a pore configuration which resembles measurements of the sample (although the heuristic process does not reflect reality). The approach is designed such that qualitative findings, such as overlap of pores, and quantitative findings, such as the pore size distributions, are reproduced in the model.

Apart from reproducing previous morphological measurements, the heuristic has to be able to pack a large amount of ellipsoids densely and efficiently. Packing algorithms exist for non-overlapping ellipsoids, see section 1.3.2. However, in the present case, the final packing is supposed to be overlapping. Subsequently, a custom approach is developed.

### Approximative Distance of Ellipsoid Surfaces

A design goal of the heuristic is to exert a separating force onto ellipsoids in the case of mutual overlap: although overlap is allowed, it should be as minimal as possible. Therefore, it is desirable that ellipsoids that have more overlap are subject to a higher separating force.

The equations that describe ellipsoid surface distances involve sixth order polynomials, and can only be solved numerically. An elegant way to determine the surface distance of non-overlapping ellipsoids was developed by (Lin and Han, 2002). However, as soon as ellipsoids are overlapping, a non-convex optimization problem has to be solved. A method to obtain the signed distance for overlapping ellipsoids does exist (Iwata, Nakatsukasa, and Takeda, 2015), however, the approach is quite involved and prohibitive in our case since it requires solving a non-convex optimization problem for each overlapping sphere pair.

Instead of calculating exact distances, approximate distances are calculated in the heuristic, using an ellipsoid overlap potential  $F_{ij}$  (Perram and Wertheim, 1985), which was also employed

in another ellipsoid packing algorithm (Donev, Torquato, and Stillinger, 2005b).  $F_{ij}$  has the following property:

$$\begin{aligned} F_{ij} &> 1 && \text{if ellipsoids are disjoint} \\ F_{ij} &= 1 && \text{if ellipsoids are in external tangency} \\ F_{ij} &< 1 && \text{if ellipsoids overlap} \end{aligned} \quad (3.4)$$

The overlap potential is calculated as follows, where each of the following steps is explained in detail in (Perram and Wertheim, 1985): First, consider the function

$$F_i(\mathbf{x}) = F(\mathbf{x}, \mathbf{E}_i) = \mathbf{x}^T \mathbf{E}_i \mathbf{x} \quad (3.5)$$

where  $F_i(\mathbf{x} - \mathbf{c}_i) \leq 1$  is equivalent to (3.1). Next define

$$F_{ij}(\mathbf{x}, \lambda) = \lambda F_i(\mathbf{x}) + (1 - \lambda) F_j(\mathbf{x}) \quad (3.6)$$

where  $0 \leq \lambda \leq 1$ . A path  $\mathbf{x}(\lambda)$  connects ellipsoid centers  $\mathbf{c}_i$  and  $\mathbf{c}_j$  such that  $F_{ij}(\mathbf{x}(\lambda), \lambda) = F_{ij}(\lambda)$  is minimal for each  $\lambda$ .  $F_{ij}(\lambda)$  can be written explicitly as

$$F_{ij}(\lambda) = \lambda(1 - \lambda) \mathbf{c}_{ij}^T \mathbf{E}_{ij}(\lambda) \mathbf{c}_{ij} \quad (3.7)$$

where  $\mathbf{c}_{ij} = \mathbf{c}_j - \mathbf{c}_i$ , and

$$\mathbf{E}_{ij}(\lambda) = (\lambda \mathbf{E}_j^{-1} + (1 - \lambda) \mathbf{E}_i^{-1})^{-1} \quad (3.8)$$

$F_{ij}(\lambda)$  is a unimodal function, i.e.,  $F_{ij}(0) = F_{ij}(1) = 0$ , and for  $0 \leq \lambda \leq 1$ , it has a negative curvature,  $\nabla^2 F_{ij}(\mathbf{x}(\lambda), \lambda) < 0$ .

Finally,

$$F_{ij} = \max_{\lambda} (F_{ij}(\lambda)) \quad (3.9)$$

In (Donev, Torquato, and Stillinger, 2005b),  $F_{ij}(\lambda)$  is converted into polynomials such that  $F_{ij}(\lambda) = p(\lambda)/q(\lambda)$ , using properties of (3.2), matrix adjugates, and determinants. The updated form makes it trivial to calculate the derivative  $F'_{ij}(\lambda)$ , and use Newton's method to find  $F_{ij}$ .

$F_{ij}$  is obtained differently in the heuristic, in order to decrease implementation effort: Each calculation of  $F_{ij}(\lambda)$  is done by solving (3.7), where matrix inversion in (3.8) is sped up by using Cholesky decomposition (the matrix that needs to be inverted is positive definite). The

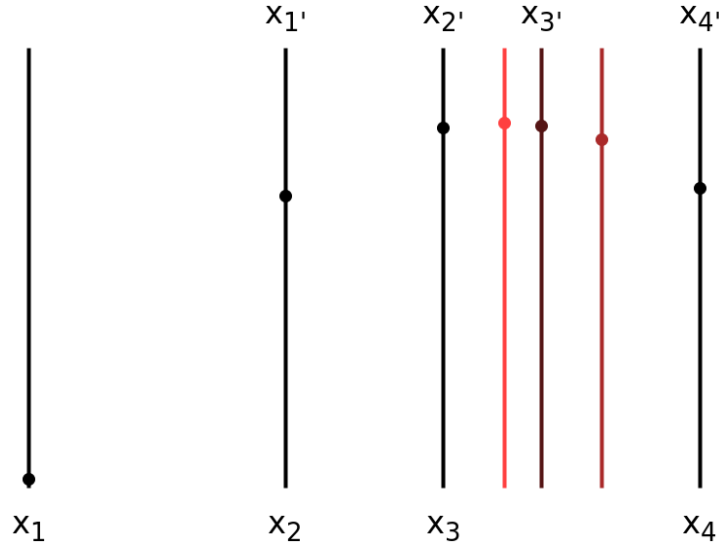


**Fig. 3.2** Golden section search for a function  $f(x)$  that is unimodal in the interval  $[x_1, x_4]$ . Note that the initial points are  $x_2 = (x_4 - x_1)/\phi^2$  and  $x_3 = (x_4 - x_1)/\phi$ , where  $\phi = (1 + \sqrt{5})/2$  is the golden section. Each subsequent sampling point reduces the search interval, and creates a set of 4 points  $(x'_1, \dots, x'_4)$  with the same ratios as in the initial interval.

maximum in (3.9) is then found using the golden section search (Kiefer, 1953). A visualization explanation of the golden section search is given in fig. 3.2.

The resulting  $F_{ij}$  can be interpreted as follows: If  $F_{ij} = s^2$  is calculated from  $\mathcal{E}_i$  and  $\mathcal{E}_j$ , then the scaled ellipsoids defined by  $\mathcal{E}_i^s = \mathcal{E}(\mathbf{E}_i/s, \mathbf{c}_i)$  and  $\mathcal{E}_j^s = \mathcal{E}(\mathbf{E}_j/s, \mathbf{c}_j)$  are in external tangency. Furthermore, the common point  $\mathbf{x}_{ij}^s$  can be calculated as

$$\mathbf{x}_{ij}^s = \mathbf{c}_i + (1 - \lambda^*)\mathbf{E}_i^{-1}\mathbf{E}_{ij}(\lambda^*)\mathbf{c}_{ij} = \mathbf{c}_j - \lambda^*\mathbf{E}_j^{-1}\mathbf{E}_{ij}(\lambda^*)\mathbf{c}_{ij} \quad (3.10)$$

where  $\lambda^*$  corresponds to the maximal value  $F_{ij}$ .

Finally, also in contrast to (Perram and Wertheim, 1985) and (Donev, Torquato, and Stillinger, 2005b), an approximative distance for overlapping ellipsoids is defined. A line is used, which originates at  $\mathbf{x}_{ij}^s$  and has the direction

$$\mathbf{n}_{ij}^s = \frac{\mathbf{E}_i(\mathbf{x}_{ij}^s - \mathbf{c}_i)}{\|\mathbf{E}_i(\mathbf{x}_{ij}^s - \mathbf{c}_i)\|} = -\frac{\mathbf{E}_j(\mathbf{x}_{ij}^s - \mathbf{c}_j)}{\|\mathbf{E}_j(\mathbf{x}_{ij}^s - \mathbf{c}_j)\|} \quad (3.11)$$

Intersection of the line with the (unscaled) ellipsoids  $\mathcal{E}_i$ ,  $\mathcal{E}_j$  is a straightforward operation, and results in two points  $\mathbf{x}_i$ ,  $\mathbf{x}_j$ , which define the approximative distance,

$$d_{ij} \approx \|\mathbf{x}_i - \mathbf{x}_j\| \quad (3.12)$$

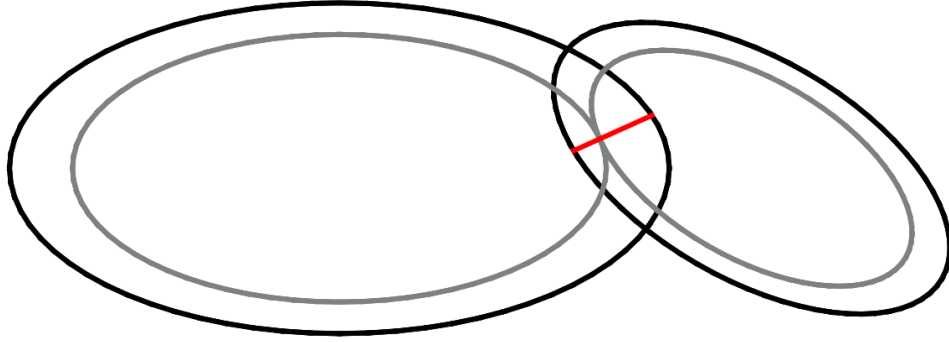


**Fig. 3.3** Approximative distance (red) between two overlapping ellipsoids (black). Grey ellipsoids are scaled versions of the original ellipsoids, and are in external tangency. The red line includes the contact point of the scaled ellipsoids and is parallel to its surface normal.

A visualization can be found in fig. 3.3.

### Interaction Law

As stated before, the goal of the heuristic bubbling approach is to minimize overlap between ellipsoids. In order to do this as efficiently as possible, each overlapping displacement,

$$\mathbf{x}_{ij} = \mathbf{x}_j - \mathbf{x}_i \quad (3.13)$$

is treated as a critically damped spring, where  $\mathbf{x}_i, \mathbf{x}_j$  are the positions obtained in (3.12). Subsequently, the following equation needs to be solved for each overlapping ellipsoid pair:

$$\mathbf{x}_{ij}'' + 2\zeta\omega_0\mathbf{x}_{ij}' + \omega_0^2\mathbf{x}_{ij} = 0 \quad (3.14)$$

where choosing  $\zeta = 1$  gives the equation for a critically damped harmonic oscillator,  $\omega_0 = 1$  simplifies the equation further, and  $(\cdot)'$  denotes the temporal derivative.  $\mathbf{x}_{ij}'$  is defined as the projection of the relative ellipsoid velocity onto the axis defined by  $\mathbf{x}_{ij}$ , i.e.,

$$\mathbf{x}_{ij}' = ((\mathbf{v}_j - \mathbf{v}_i)^T \mathbf{u}_{ij}) \mathbf{u}_{ij} \quad (3.15)$$

It should be noted that zero acceleration is present as soon as there is no overlap, i.e., when  $F_{ij} > 1$ .

Finally, pairwise acceleration is evenly split between the two ellipsoids, resulting in the following system of equations:

$$\mathbf{x}_i'' = -\epsilon\mathbf{x}_i' - 0.5 \sum_j (\mathbf{x}_{ij}' + \mathbf{x}_{ij}) \quad (3.16)$$

where a small friction factor  $-\epsilon \mathbf{x}'_i$  with  $\epsilon \ll 0.5$  prevents the numerical artifact of collective motion of the system.

### Numerical Integration in the Time Domain

A box with cyclic boundary conditions is now filled with randomly placed ellipsoids, such that overlap is guaranteed, for example,

$$V_{\text{box}} = \sum_i V_i^{\text{ellipsoid}} \quad (3.17)$$

Since ellipsoid interaction is modeled with damped oscillators, the total energy of the system is given by

$$E_{\text{total}} = \sum_i \left( \frac{1}{2} \mathbf{v}_i^2 + \frac{1}{2} \sum_{j>i} \mathbf{x}_{ij}^2 \right) \quad (3.18)$$

It should be noted that due to damping and the friction factor, energy is continuously dissipating from the ellipsoid configuration. Therefore, it is sufficient to use the Euler method for time integration, i.e.,

$$\begin{aligned} \mathbf{x}_i^{n+1} &= \mathbf{x}_i^n + \mathbf{v}_i^n \Delta t \\ \mathbf{v}_i^{n+1} &= \mathbf{v}_i^n + \mathbf{a}_i^n \Delta t \end{aligned} \quad (3.19)$$

Before each step  $n \rightarrow (n+1)$ ,  $\Delta t$  is limited such that

$$\max(\|\mathbf{v}_i^n\|) \Delta t \leq \Delta x_{\text{stable}} \quad \text{and} \quad \max(\|\mathbf{a}_i^n\|) \Delta t \leq \Delta v_{\text{stable}} \quad (3.20)$$

where  $\Delta x_{\text{stable}}$  and  $\Delta v_{\text{stable}}$  are small scalar quantities for absolute displacement and velocity. For example,  $\Delta x_{\text{stable}}$  can be chosen as  $1/10^{\text{th}}$  of the smallest ellipsoid size. When  $E_{\text{total}}$  approaches its infimum, it is possible that the integration step is too large, and the system behaves unphysically, i.e.,  $E_{\text{total}}^{n+1} > E_{\text{total}}^n$ . If this is the case, then the ellipsoid configuration is reverted to state  $n$ , and the quantities  $\Delta x_{\text{stable}}$  and  $\Delta v_{\text{stable}}$  are divided by two. The heuristic ends when

$$|E_{\text{total}}^n - E_{\text{total}}^{n-100}| \ll E_{\text{total}}^1 \quad (3.21)$$

### 3.1.3 Sequential Addition of Small Pores

After the previously described heuristic packing process is finished, the large pore configuration is binarized as a voxel volume. Small pores ( $r_{\text{eff}} < 8\mu\text{m}$ ) are added by setting voxels in the binary volume to zero. As described at the beginning of section 3.1.2, the sequential addition method is suitable for low relative porosities. Furthermore, it is computationally inexpensive:

For each small pore, i.e., sphere, a radius is sampled from the previously found distribution (fig. 2.16/ tab. 2.2). Then, random positions are trialed until 90 % of the potential pore is contained inside the material phase. Corresponding voxels are erased, and the process is repeated until all small pores are distributed.

### 3.1.4 Comparison to Literature

In contrast to the previous chapter, where literature was compared with respect to analysis results, literature related to this chapter is more concerned with methodology, and is subsequently discussed at this point.

#### Sphere and Ellipsoid Packing

It is possible to pack a relatively large number of spheres (10 000 or more) using event driven sphere packing methods (Lubachevsky and Stillinger, 1990; Kansal, Torquato, and Stillinger, 2002). A mathematically rigorous approach is taken by Torquato and Jiao (2010), in the sense that the produced packings are “strictly jammed” (Atkinson, Stillinger, and Torquato, 2013), i.e., provably stable against compression and shear. However, the non-overlapping sphere packings are more relevant for research in mathematics and theoretical chemistry, and less for material modeling. In particular, the foam model in this thesis is based on overlapping ellipsoids (instead of spheres), which are a closer approximation to the real carbon foam morphology.

Current ellipsoid packing algorithms fulfill non-overlapping criteria, and packings are smaller than for spheres: Birgin, Lobato, and Martínez (2017) report up to 1000 packed ellipsoids, and Donev, Torquato, and Stillinger (2005b) report up to 5000 packed ellipsoids. Again, existing ellipsoid packing algorithms have a focus which is different from material modeling. For example, the algorithms are used to explore maximal packing densities inside spherical containers. In this thesis, requirements to packed ellipsoids are less strict: pairwise overlap of ellipsoids is governed by simple spring laws, therefore, overlap is flexible. Subsequently, it is possible to pack relatively large amounts of ellipsoids (around 10 000) within a few hours of computation.

## Carbon Foam Modeling

The goal in this thesis is to model a full foam specimen. Other authors who create digital models of carbon foams are Kirca et al. (2007) and Dyck and Straatman (2015). Kirca et al. (2007) use an overlapping sphere pack to model void space, but do not specify details of the packing procedure. The authors convert the packing to CAD data, which are then used by a Finite Element program to calculate effective mechanical properties.

Dyck and Straatman (2015) provide more details, their sphere pack is the result of a physical simulations. Sphere interaction is described by a pairwise contact function, which is a simplification of a more general bubble force-displacement relationship derived by Chan, Klaseboer, and Manica (2011). Using the notation in this thesis, the contact function used by the authors can be written as  $d_{ij} \propto F_{ij} \log(F_{ij}/C)$ , where  $F_{ij}/C \ll 1$ . After the packing simulation, the authors convert the sphere configuration to CAD data, which are then used for Computational Fluid Dynamics simulations.

Compared to the publications above, the foam model in this thesis is not converted to CAD data, but to voxel data. This is due to differences in the Finite Element software, which is used in the evaluation step. The pairwise contact function used by Dyck and Straatman (2015) is more elaborate than the heuristic which is used in this thesis. However, no production process parameters were provided for the foam sample of this thesis. They would have been a necessary input for the bubble-force formula. Also, the critically damped springs in the heuristic lead to a quick convergence towards an equilibrium state, which is an advantage with respect to packing time.

## 3.2 Statistics of Model

The foam model is created with the following parameters:

- Ellipsoid/sphere sizes, shapes, and orientations are sampled from the previously fitted distributions.
- Number of pores: 100 000. Large pores: 9 581. Small pores: 90 419.
- Total volume of large pores, i.e., ellipsoids:  $0.95 V_{\text{box}}$ , see also (3.17)
- Binarized voxel volume dimensions:  $4\,000 \times 4\,000 \times 4\,000$ .
- Size of coverage representation:  $2\,000 \times 2\,000 \times 2\,000$ . Each binary block of  $2 \times 2 \times 2$  voxels is summed to obtain a “material fraction”.

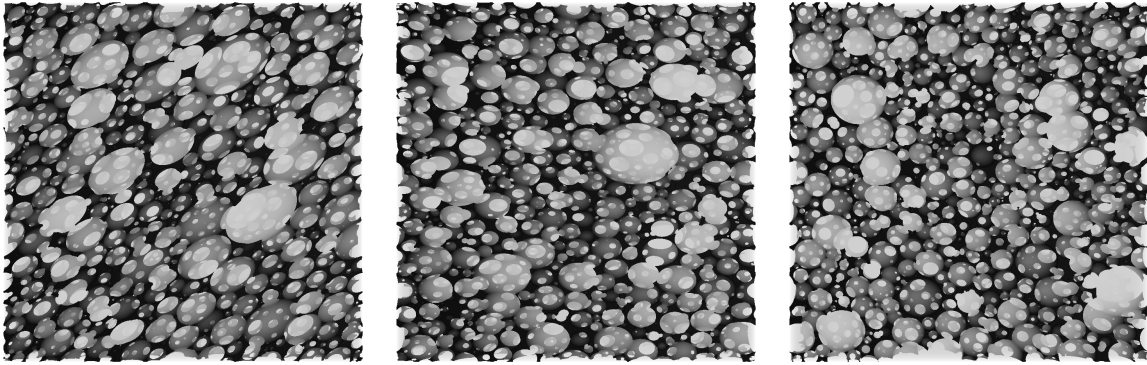


**Fig. 3.4** Rendering of generated foam model. Compare to fig. 2.13.

After the foam model is created, its coverage representation is analyzed using the same methods as previously applied to the foam sample (section 2.4). A rendering of the model foam can be found in fig. 3.4.

### 3.2.1 Pore Size Distribution

As before, the modified Maximal Ball algorithm is used to analyze the pore size distribution of the voxelized model.

#### Results

A visualization of the segmented foam and the obtained pore size distribution can be found in fig. 3.5. The voxel size in the model is smaller than in the sample: In the model, one voxel corresponds to  $0.69\mu\text{m}$ , compared to  $1\mu\text{m}$  in the sample. Porosity of the model is approximately equal to the sample,  $\phi_{\text{model}} = 89.5\%$ , and  $\phi_{\text{sample}} = 90.3\%$ .

#### Discussion

Since the model is based on the pore size distribution extracted from the sample, it is expected that the pore statistics are approximately equal. Fig. 3.5 (right) yields the following findings:

- In total, there are less pores in the model than in the sample. This follows directly from the decreased total volume of the model.
- A small peak can be seen at  $r^{\text{eff}} = 8\mu\text{m}$ . It is located at the separation point between the ellipsoid-packing heuristic of large pores and the sequential addition of small pores. Since the two methods are quite different, as well as the pore shapes (ellipsoids and spheres), a

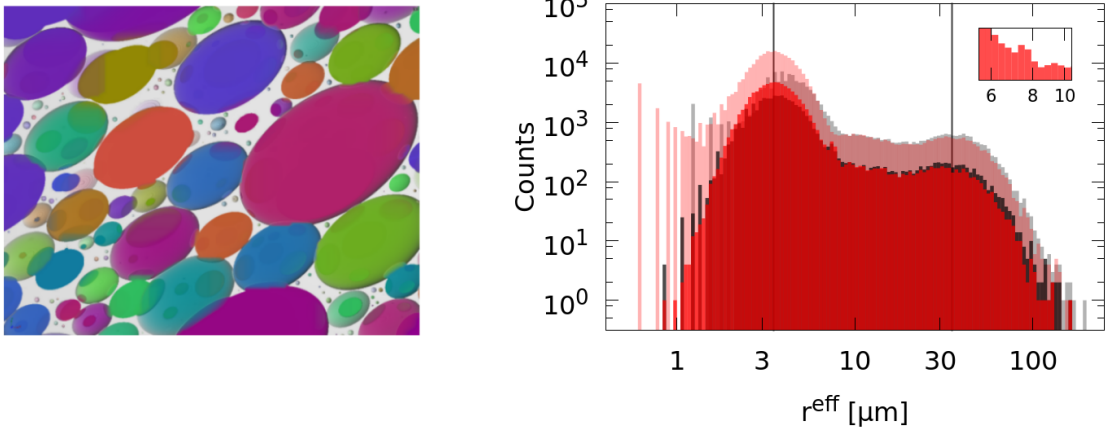


**Fig. 3.5 Left:** Segmentation of the generated foam model. Compare to fig. 2.14. **Right:** In the foreground, the pore size distribution of the model is given. In the background, the distribution of the physical sample can be seen. Two vertical lines show alignment of distributions. The small inlet window shows an artifact in the distribution that is due to the two stage modeling approach. Compare also to fig. 2.15.

small artifact is expected, although it is not possible to give an exact explanation for the origination.

### 3.2.2 Anisotropy of Modeled Pores

When sampling ellipsoids for the model (section 3.1.1), a one-to-one (piecewise linear) correspondence between effective radius and ratio of ellipsoid axes is chosen (eq. 2.36). Similarly, angular rotation of ellipsoids is directly mapped from the effective radius (eq. 2.37). In other words: If two sampled ellipsoids have the same effective radius, then they have the same axes ratios and orientation.

However, packed ellipsoids are overlapping. Subsequently, pore bodies have dents, which lead to small deviations in the covariance matrices (eq. 2.21), and subsequently, to variations of pore anisotropy, which are measured with principal component analysis.

## Results

Segmented pores of the model foam, which were previously analyzed with respect to size, are now analyzed using principal component analysis. Ratios of pore axes are depicted in fig. 3.6 (left), pore orientations are depicted in fig. 3.6 (right).

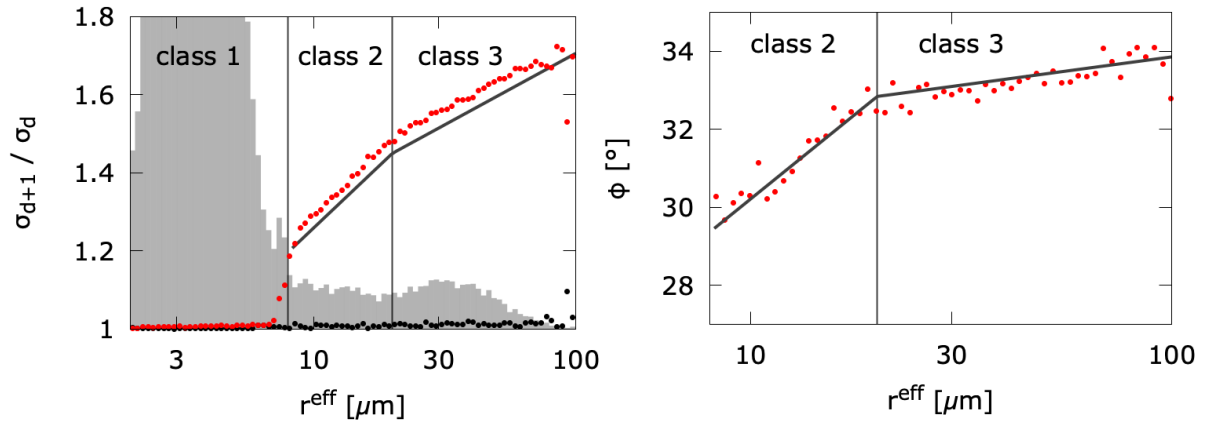


**Fig. 3.6 Left:** Ratios of pore axes ( $\langle\sigma_3\rangle/\langle\sigma_2\rangle$  and  $\langle\sigma_2\rangle/\langle\sigma_1\rangle$ ) as a function of effective radius. Black lines are taken from the fit in fig. 2.17. Red and black dots represent values which are measured in the model foam by principal component analysis. **Right:** Rotation angle for pores (rotation around z-axis, as measured from x-axis), as a function of effective radius. The black line is taken from the fit in fig. 2.19. Measurements (red dots) are a result of principal component analysis of pores in the model foam.

### Discussion

The right part of fig. 3.6 does not show surprising results: Variations of the orientation are expected because of ellipsoid overlaps, as explained before. Measured ratios of pore axes, as seen in fig. 3.6 (left), show unexpected behavior: Pore axes ratios  $\langle\sigma_3\rangle/\langle\sigma_2\rangle$  are always above the input ellipsoid axes ratios which are specified by eq. 2.36. In order to get a better understanding of the measured ratios, a Monte Carlo (MC) simulation is conducted in 2D:

1. Each MC experiment starts with an ellipse that is placed at the center of a discretized grid: Grid position that are covered by the ellipse are set to 1, else they are set to 0.
2. A copy of the ellipse (with equal axes ratio and orientation) is placed at a random position.
3. Positions which are inside the intersection area of the central ellipse and the copied ellipse are set to 0.
4. If no overlap exists between central ellipse and copied ellipse, then the experiment is discarded.
5. If overlap exists, then principal component analysis is applied to the remaining body of the central ellipse.

An ellipse axes ratio of  $a/b = 1.5$  is chosen. After 100 000 experiments with overlapping ellipses, the mean ‘‘pore’’ ratio is  $\langle\sigma_3/\sigma_2\rangle = 1.758 \pm 0.002$ , where 0.002 is the standard error

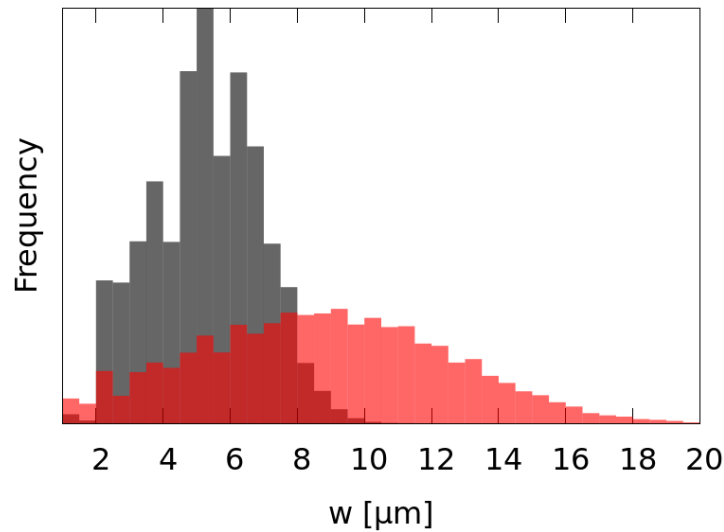


**Fig. 3.7** Wall thickness distribution of sample (black) and model (red).

of the mean. Although the MC simulation with ellipse pairs is a crude approximation of the pairwise ellipsoid overlaps in the model foam, the MC simulation indicates that the ellipsoid overlap leads to an increased pore axes ratio.

### 3.2.3 Wall Thickness Distribution

In contrast to properties of pores, the wall thickness distribution (section 2.1.3) did not play a role in the creation of the model. Subsequently, it serves as an indicator for possible differences between sample and model.

#### Results

Wall thickness distributions of sample and model are given in fig. 3.7. Calculating mean and standard deviation for  $w$  gives  $(5.27 \pm 1.61) \mu\text{m}$  for the sample and  $(8.77 \pm 3.68) \mu\text{m}$  for the model.

#### Discussion

Unlike pore statistics, wall thickness distributions differ between sample and model. With respect to mechanical properties, the large wall thickness variation of the model (in relative and absolute values) is not favorable: A higher variation in wall thickness corresponds to a lower elastic modulus (Li, Gao, and Subhash, 2006). In order to test the fitness of the model, it is compared to the sample via mechanical simulations in the next chapter.

# Chapter 4

## Structural Mechanics Simulation

Mechanics simulations are used to reduce compare the effective mechanical properties of model and sample. The procedure has been applied before (Arand and Hesser, 2018). However, in contrast to the previous publication, more experiments are carried out.

### 4.1 Methods

Virtual mechanics experiments are conducted with the software VGSTUDIO MAX 3.2., which uses a method similar to the finite cell method (Schillinger and Rues, 2015). Correctness of the software was shown in two publications (Plessis et al., 2017; Fieres, Schumann, and Reinhart, 2018).

#### 4.1.1 Preparation of Data Sets for Mechanics Simulation

The previously created foam model with voxel size of  $0.69\mu\text{m}$  is resampled such that one voxel corresponds to  $1\mu\text{m}$ , in order to match the resolution of the sample.

Regions of size  $1000 \times 1000 \times 1000 \mu\text{m}^3$ , are selected from sample and model. Next, each region is partitioned into 8 cubical subregions of size  $500^3$  voxels, which are the basis for mechanical simulations. Partitioning is done for two reasons: First, multiple experiments create statistics, as long as each subregion can be considered a representative volume element (RVE) (Kanit et al., 2003). Second, the mechanics simulation demands a high amount of computational memory, which favors small volumes.

Three data sets are created from each of the  $2 \times 8$  subregions: For each coordinate axis direction, planar slabs with thickness  $50\mu\text{m}$  are added at both sides of the current subregion, resulting in a sandwich structure, which is typical for real and virtual mechanics experiments

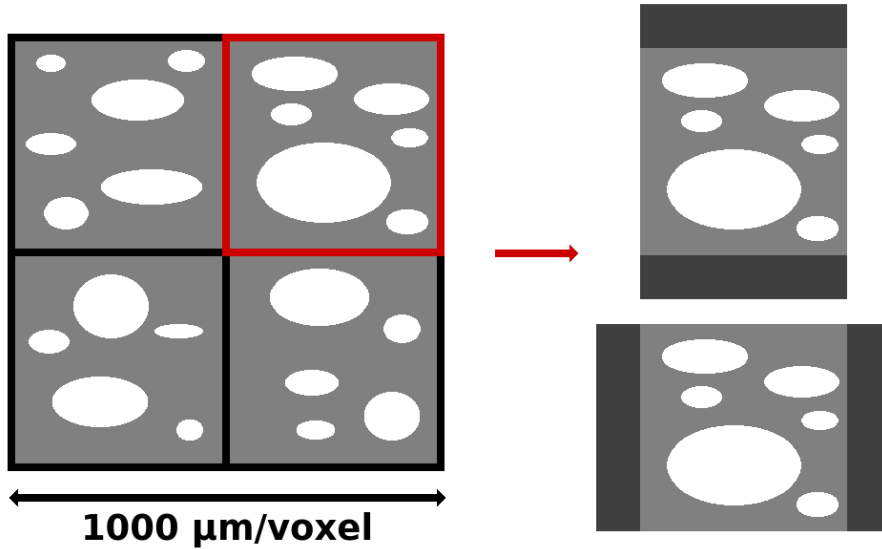


**Fig. 4.1** Partitioning of sample and model. Give a region of size  $1000^3$  voxels, 8 subregions of size  $500^3$  voxels are selected. For each subregion, 3 data sets are created for the experiments in x-,y-,z-direction. In total,  $2 \times 8 \times 3 = 48$  data sets are created. Slabs in the image are colored dark grey for better visualization. For the experiment, the slabs have the same material properties as the foam.

(Kirca et al., 2007). The slabs provide an even distribution of the applied force and fixation. A visualization of the data set creation can be found in fig. 4.1.

In order to identify each experiment, they are named according to a scheme:

$$\begin{array}{ccc}
 \text{s/m} & 1 \dots 8 & \text{x/y/z} \\
 \text{sample/model} & \text{subregion} & \text{direction of compression/ slab positions}
 \end{array} \quad (4.1)$$

For example, data set m3y is the third subregion of the model, with slabs perpendicular to the y-direction.

#### 4.1.2 Mechanics Simulation with VGSTUDIO MAX

Bulk material properties are set according to literature values (Sihn and Rice, 2003). Young's modulus is set to  $E_{\text{bulk}} = 15.61$  GPa, Poisson's ratio is set to  $\nu_{\text{bulk}} = 0.33$ . The simulation cell size is set to 1 voxel. Since the software uses an embedded domain method for mechanics simulation, subvoxel structures (surfaces which cut through the voxel cube) are considered in the calculation (Schillinger and Ruess, 2015). Multiple, similar experiments are set up and calculated using automation macros.

## 4.2 Evaluation of Simulations

Subregions which are used for mechanics simulation have a size of  $500 \times 500 \times 500 \mu\text{m}^3$ , while the largest bubble, as measured in the previous chapters, has an effective radius of approximately  $160 \mu\text{m}$ . Therefore, it is important to see if at least some of the analyzed subregions can be considered as representative volume elements.

Subsequently, for sample and model, all eight experiments in x-direction are calculated, i.e., s1x, s2x, ..., s8x, and m1x, m2x, ..., m8x. Then, for sample and model, the four experiments in x-direction which are closest to their mutual average Young's modulus are selected for further evaluation. The selected experiments will also be evaluated in y- and z-direction later.

### 4.2.1 Simulations in x-Direction

In the mechanics simulation, a force of  $F = 1 \text{ N}$  is applied in the direction of the surface normal of a slab ("mobile slab"), while the other slab is kept fixed. A visualization of the setup can be seen in fig. 4.2. After simulating, the total displacement  $\langle \Delta l \rangle$  is measured as the average displacement of the central plane  $\mathcal{P}$  of the mobile slab:

$$\langle \Delta l \rangle = \int_{\mathbf{x} \in \mathcal{P}} \Delta l(\mathbf{x}) dA / A \quad (4.2)$$

where  $A = 500^2 \mu\text{m}^2$ . Then,  $\langle \Delta l \rangle$  is incorporated into the textbook formula to obtain the effective Young's modulus  $E$ ,

$$E = (Fl_0) / (A \langle \Delta l \rangle) \quad (4.3)$$

where  $l_0 = 500 \mu\text{m}$ . The actual data set length is  $l_0^* = 500 \mu\text{m} + 2 \cdot 50 \mu\text{m}$ , (foam and two slabs). However, the assumption is made that the dense slabs deform negligibly compared to  $\langle \Delta l \rangle$ , and the equation is approximated in the above form.

### Results

Calculated (effective) Young's moduli  $E$  for sample and model are summarized in tables 4.1 and 4.2, respectively.

Experiment	s1x	s2x	s3x	s4x	s5x	s6x	s7x	s8x
$E$ [GPa]	<b>0.243</b>	0.219	<b>0.245</b>	0.269	0.199	0.262	<b>0.249</b>	<b>0.254</b>

**Table 4.1** Effective Young's moduli in x-direction of sample sub regions. Values which are closest to the common mean are bold.

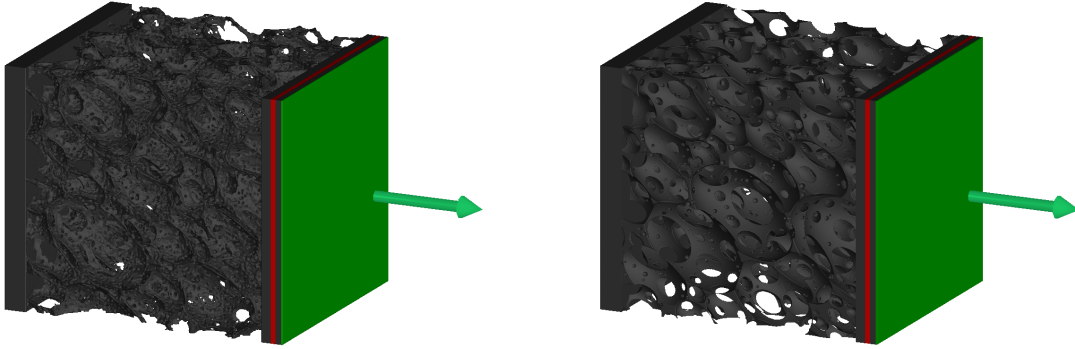


**Fig. 4.2** Simulation setups for data sets s1x (left) and m1x (right). A force of 1 N (green arrow) is applied in x-direction, to the surface of the right slab (green plane). The bottom side of the left slab (not visible) is fixed.  $\Delta \bar{l}$ , the displacement of the foam which is used for the calculation of  $E$ , is calculated from the right slab's central plane  $\mathcal{P}$  (red color).

Experiment	m1x	m2x	m3x	m4x	m5x	m6x	m7x	m8x
$E$ [GPa]	<b>0.159</b>	0.212	<b>0.192</b>	0.207	0.192	<b>0.147</b>	<b>0.179</b>	0.096

**Table 4.2** Effective Young's moduli in x-direction of model sub regions. Values which are closest to the common mean are bold.

## Discussion

For each table 4.1 and 4.2, mean values and standard deviations of the four most similar samples are calculated:

$$\begin{aligned} \langle E \rangle_{x, \text{sample}} \pm \sigma_{x, \text{sample}} &= (0.248 \pm 0.005) \text{ GPa} \\ \langle E \rangle_{x, \text{model}} \pm \sigma_{x, \text{model}} &= (0.169 \pm 0.020) \text{ GPa} \end{aligned} \quad (4.4)$$

$\langle E \rangle_{x, \text{sample}}$  is approximately 45 % higher than  $\langle E \rangle_{x, \text{model}}$ . The significantly higher modulus is surprising, since sample and model have approximately the same pore size distribution and overall porosity. Further discussion of modulus deviation follows after simulations in y- and z-direction.

With respect to standard deviation, results are vice versa:  $\sigma_{x, \text{sample}} < \sigma_{x, \text{model}}$ , the difference is even more striking if the ratios  $\sigma/\langle E \rangle$  are considered. The model data set seems to have a inhomogeneous distribution of pores (and subsequently material), which is showcased in data set m8x (fig. 4.3). In order to gain further insights, sample and model are analyzed in y- and z-direction.

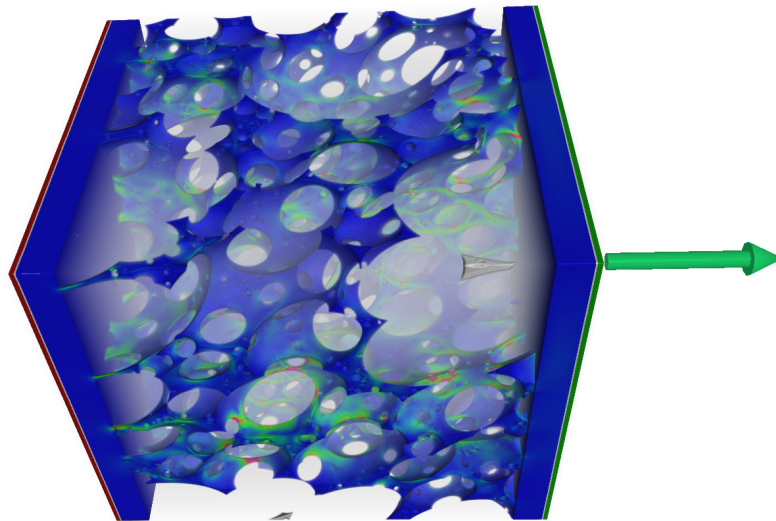


**Fig. 4.3** Data set m8x has a very low elastic modulus according to table 4.2. The rendering reveals large empty regions.

#### 4.2.2 Simulations in y- and z-Direction

Data sets which were selected in tables 4.1 and 4.2 are analyzed in y- and z-direction.

##### Results

Simulation results are obtained similarly to the previous section. They are summarized in tables 4.3 and 4.4.

Experiment	s1y	s1z	s3y	s3z	s7y	s7z	s8y	s8z
$E$ [GPa]	0.154	0.134	0.165	0.131	0.163	0.140	0.176	0.132

**Table 4.3** Effective Young's moduli in sample sub regions.

Experiment	m1y	m1z	m3y	m3z	m6y	m6z	m7y	m7z
$E$ [GPa]	0.125	0.122	0.133	0.107	0.140	0.115	0.133	0.142

**Table 4.4** Effective Young's moduli in model sub regions.

## Discussion

Means and standard deviations of the elastic moduli in y-direction are

$$\begin{aligned}\langle E \rangle_{y, \text{ sample}} \pm \sigma_{y, \text{ sample}} &= (0.164 \pm 0.009) \text{ GPa} \\ \langle E \rangle_{y, \text{ model}} \pm \sigma_{y, \text{ model}} &= (0.133 \pm 0.006) \text{ GPa}\end{aligned}\quad (4.5)$$

and in z-direction

$$\begin{aligned}\langle E \rangle_{z, \text{ sample}} \pm \sigma_{z, \text{ sample}} &= (0.134 \pm 0.004) \text{ GPa} \\ \langle E \rangle_{z, \text{ model}} \pm \sigma_{z, \text{ model}} &= (0.121 \pm 0.015) \text{ GPa}\end{aligned}\quad (4.6)$$

Again, elastic moduli in the sample are higher than in the model: 23 % in y-direction, and 10 % in z-direction. Standard deviations in z-direction show a similar behavior to the x-direction,  $\sigma_{z, \text{ sample}} < \sigma_{z, \text{ model}}$ . However, in y-direction,  $\sigma_{y, \text{ sample}} > \sigma_{y, \text{ model}}$ .

Next, relative ratios of average elastic moduli are compared.

$$\begin{aligned}\langle E \rangle_{x, \text{ sample}} : \langle E \rangle_{y, \text{ sample}} : \langle E \rangle_{z, \text{ sample}} &= 1.47 : 1 : 0.82 \\ \langle E \rangle_{x, \text{ model}} : \langle E \rangle_{y, \text{ model}} : \langle E \rangle_{z, \text{ model}} &= 1.30 : 1 : 0.91\end{aligned}\quad (4.7)$$

Despite pore elongations of the model were chosen according to the sample, anisotropy of the sample is more distinct than for the model, with respect to Young's modulus. This is surprising: In section 3.2.2, model pores were measured with respect to elongations, which were on average higher than pore elongation in the sample. It is expected that a higher elongation of pores leads to more anisotropy in the material distribution, which would lead to higher relative ratios of elastic moduli.

Altogether, the real world foam sample has favorable mechanical properties, i.e., the same amount of material gives a significantly higher elastic modulus. There are two possible explanations for low performance of the model foam:

- Foam ligaments have a greater influence on the overall elastic modulus than material nodes (where ligaments meet) (Sihn and Roy, 2004). The sample has more ligaments, i.e., membranes between void spaces, than the model: A real world foam is the result of a physical/ chemical process, and membranes form naturally as a result of bubble surface tension. The geometric model on the other hand does not incorporate a heuristic that promotes membrane formation. Digitally measuring the surface area of sample and model gives an indicator for the amount of ligaments (the node surface is negligible compared to the total surface).  $A_{\text{sample}} = 48.1 \text{ mm}^2$  is approximately 20 % larger than  $A_{\text{model}} = 40.6 \text{ mm}^2$ .

- According to Li, Gao, and Subhash (2006), a higher uniformity in the cross-sectional area of ligaments corresponds to a higher elastic modulus. This was measured in section 3.2.3: it was shown that the sample has a smaller standard deviation with respect to wall thickness, compared to the model (1.61  $\mu\text{m}$  vs 3.68  $\mu\text{m}$ ).

Following the two given explanations, Arand and Hesser (2018) modified a similar foam model by material erosion and dilation in order to homogenize wall thickness distribution, while keeping the total porosity constant. Subsequently, the effective Young's modulus could be increased.

### 4.2.3 Comparison to Literature

Foam models which can be found in literature offer formulas which assign an effective elastic modulus to a given porosity and bulk modulus. Literature sources which are also used by Kırca et al. (2007) for evaluation are used for comparison to sample and model. A summary of the literature models was given in section 1.4.2.

#### Results

Four different literature formulas are compared, using  $E_{\text{bulk}} = 15.68 \text{ GPa}$  and the material fraction  $\rho = 1 - \phi$  (where  $\phi$  is the porosity).

- Warren and Kraynik (1988):  $E = E_{\text{bulk}} \rho^2(11 + 4\rho)/(10 + 31\rho + 4\rho^2)$
- Zhu, Knott, and Mills (1997):  $E = E_{\text{bulk}} 1.009\rho^2/(1 + 1.514\rho)$
- Roberts and Garboczi (2002):  $E = E_{\text{bulk}} 0.93\rho^{2.04}$
- Gan, Chen, and Shen (2005):  $E = E_{\text{bulk}} \rho^2/(1 + 6\rho)$

In fig. 4.4, the formulas are evaluated with porosities  $\phi \in [0.89, 0.91]$ , and are shown together with the simulation results for sample and model.

#### Discussion

All literature formulas were derived with the help of foam models. The model which was used in this thesis does not show significant deviations compared to the other models. In contrast, the sample has increased elastic moduli, compared to the literature models.

According to Li, Gao, and Subhash (2006), polydispersity of foam structures leads to increased moduli, compared to structures with uniform cell sizes: Young's modulus of model foams with irregular cells is between 85 % and 90 % higher than the modulus of homogeneous

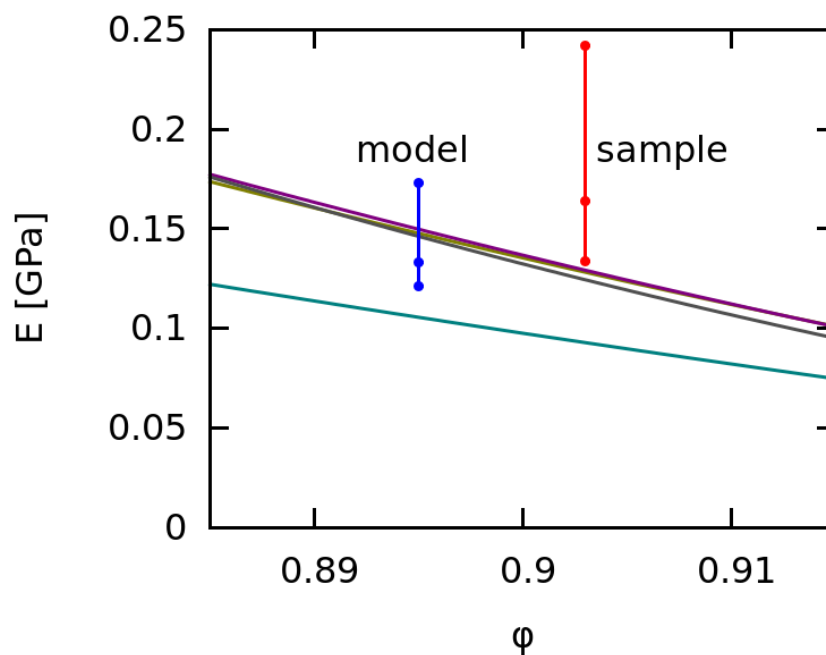


**Fig. 4.4** Comparison of Young's moduli according to literature formulas with measured ones. The three curves which are close to each other are calculated according to the formulas by Warren and Kraynik (1988), Zhu, Knott, and Mills (1997), and Roberts and Garboczi (2002). The curve at the bottom corresponds to Gan, Chen, and Shen (2005). For sample and model, the points correspond to  $\langle E \rangle_x$ ,  $\langle E \rangle_y$ , and  $\langle E \rangle_z$ . Porosities of sample and model, as measured by voxel counting, are  $\phi_{\text{sample}} = 90.3 \%$  and  $\phi_{\text{model}} = 89.5 \%$ .

model foams. In this thesis, cell sizes of sample and model are highly irregular, while in the literature models, cells are either constant or only slightly irregular (section [1.4.2](#)). Considering this information, the sample matches the literature formulas better than the model.



# Chapter 5

## Conclusion

Investigations of a carbon foam sample led to improvements of the maximal ball algorithm, morphological analysis based on pore statistics, a novel two-step modeling process with an ellipsoid packing heuristic, and an evaluation based on multiple mechanics simulations.

### Morphological Analysis of Pore Space

The maximal ball algorithm was improved with respect to computer memory usage, and also with respect to calculation speed and accuracy (Arand and Hesser, 2017). Furthermore, the step-by-step explanation given in this thesis might serve as a useful implementation instruction for other researchers, ideally after reading the “classic” papers (Silin and Patzek, 2006; Dong and Blunt, 2009). Parts of the modified maximal ball algorithm run in a single thread. It would be interesting to invest engineering work in order to clear this limitation.

Data sets which were investigated have void spaces of similar type: Verification data sets were generated from spheres, the carbon foam sample consists of pores which resemble ellipsoids, and the foam model was created accordingly. These geometries are based on convex pores, and resemble the algorithmic Maximal Ball approach, which could explain relatively unambiguous results, compared to other porous media such as sandstones (Kim, Kim, and Lindquist, 2013; Hormann et al., 2016).

Due to automatic segmentation of pore space (based on  $\mu$ CT), it was possible to quantify multiple pore statistics, i.e., size distribution, pore elongation, and orientation. Given the detected pores sizes, lognormal distributions could be identified. Although it was argued that pores with  $r_{\text{eff}} > 200\mu\text{m}$  are unlikely in the analyzed foam, certainty can only be obtained by analysis on a larger scale. Similarly, discovering pores with  $r_{\text{eff}} < 1\mu\text{m}$  needs higher resolution imaging techniques, for example SEM.

### Digital Modeling of Carbon Foam

Lognormal pore size distributions which were measured in the sample were used as input for the modeling process. This is a novelty compared to previous (sphere-based) modeling approaches for polydisperse carbon foam. Kirca et al. (2007) used an unspecified distribution, minimum and maximum bubble size are estimated from a SEM image. Dyck and Straatman (2015) used a normal distribution for modeling, mean and standard deviations were obtained from other authors (Klett, McMillan, et al., 2004). Pore sizes in the model of this thesis spanned orders of magnitude, resulting in a two-stage process, which can also be considered a novelty for carbon foam modeling.

Modeling parameters were chosen such that pore space statistics of the sample were matched closely. A next step could lie in parametric studies, which bridge the gap between uniform pore sizes and polydispersity, and between spherical and ellipsoidal pores.

After analyzing wall thickness and mechanical properties, discrepancies of model and sample became visible. The model should be improved such that these discrepancies decrease. For example, morphological erosion and dilation operations can improve the foam model in the sense that wall thickness distribution and elastic moduli get closer to the sample (Arand and Hesser, 2018).

Pairwise ellipsoid forces in the model were chosen heuristically, and it was possible to pack approximately 10 000 ellipsoids with reasonable computational resources. It would be interesting to study the actual foaming process of the sample, and model interaction forces accordingly. An example for physics based interaction laws embedded in a packing algorithm is demonstrated by Dyck and Straatman (2015).

### Structural Mechanics Simulation

Multiple subregions of size  $500^3$   $\mu\text{m}$ /voxels were analyzed. Sizes of investigated regions was small compared to the full size of the sample and model data sets, due to computational limitations. However, despite the restriction of size, it was possible to gain meaningful results: Mechanical properties of most subregions were similar to each other, as one would expect from representative volume elements. Still, it would be interesting to analyze larger regions at once, for example by distributed computing, in order to gain certainty.

Mechanics simulations were conducted in the linear-elastic regime. Beyond that, crushing behavior, which is relevant for industrial foams (Gaitanaros, Kyriakides, and Kraynik, 2012), might also be investigated. Furthermore, instead of comparing Young's modulus in x-, y-, and z-direction, apparent/ effective elasticity tensors (Pahr and Zysset, 2008) could be examined.

Previous studies with model foams showed a high sensitivity of effective elastic properties to low porosities. Given the model in this thesis, a parametric study on the relationship between porosity and effective moduli could add additional insights.

It was argued that thickness distribution of material ligaments and total surface area play an important role in effective mechanical properties. Further parametric studies which vary the uniformity of ligaments would be interesting. A starting point would be modifying an existing voxel model with erosion and dilation operations (Arand and Hesser, 2018). Another possibility is a foam model which has ligament irregularity as an input parameter (Li, Gao, and Subhash, 2006).



# References

- Andrä, H. et al. (2013a). “Digital rock physics benchmarks—Part I: Imaging and segmentation”. In: *Computers & Geosciences* 50. Benchmark problems, datasets and methodologies for the computational geosciences, pp. 25–32. ISSN: 0098-3004. DOI: [10.1016/j.cageo.2012.09.005](https://doi.org/10.1016/j.cageo.2012.09.005).
- Andrä, H. et al. (2013b). “Digital rock physics benchmarks—Part II: Computing effective properties”. In: *Computers & Geosciences* 50, pp. 33–43. ISSN: 00983004. DOI: [10.1016/j.cageo.2012.09.008](https://doi.org/10.1016/j.cageo.2012.09.008).
- Arand, F. and Hesser, J. (2017). “Accurate and efficient maximal ball algorithm for pore network extraction”. In: *Computers and Geosciences* 101, pp. 28–37. ISSN: 00983004. DOI: [10.1016/j.cageo.2017.01.004](https://doi.org/10.1016/j.cageo.2017.01.004).
- Arand, F. and Hesser, J. (2018). “Quantitative morphological analysis and digital modeling of polydisperse anisotropic carbon foam”. In: *Carbon* 136, pp. 11–20. ISSN: 0008-6223. DOI: [10.1016/j.carbon.2018.04.049](https://doi.org/10.1016/j.carbon.2018.04.049).
- Atkinson, S., Stillinger, F. H., and Torquato, S. (2013). “Detailed characterization of rattlers in exactly isostatic, strictly jammed sphere packings”. In: *Phys. Rev. E* 88 (6), p. 062208. DOI: [10.1103/PhysRevE.88.062208](https://doi.org/10.1103/PhysRevE.88.062208).
- Bangerth, W., Hartmann, R., and Kanschat, G. (2007). “deal.II—A general-purpose object-oriented finite element library”. In: *ACM Transactions on Mathematical Software* 33.4, 24–es. ISSN: 00983500. DOI: [10.1145/1268776.1268779](https://doi.org/10.1145/1268776.1268779).
- Barrett, R. et al. (1994). *Templates for the solution of linear systems: building blocks for iterative methods*. Vol. 43. Siam. ISBN: 978-0-89871-328-2.
- Bathe, K.-J. (2006). *Finite element procedures*. Bathe, Klaus-Jürgen. ISBN: 0133014584.
- Baumeister, J., Banhart, J., and Weber, M. (1997). “Aluminium foams for transport industry”. In: *Materials & Design* 18.4, pp. 217–220. ISSN: 0261-3069. DOI: [10.1016/S0261-3069\(97\)00050-2](https://doi.org/10.1016/S0261-3069(97)00050-2).
- Beechem, T., Lafdi, K., and Elgafy, A. (2005). “Bubble growth mechanism in carbon foams”. In: *Carbon* 43.5, pp. 1055–1064. ISSN: 00086223. DOI: [10.1016/j.carbon.2004.11.046](https://doi.org/10.1016/j.carbon.2004.11.046).
- Benouali, A.-H. et al. (2005). “Investigation on the influence of cell shape anisotropy on the mechanical performance of closed cell aluminium foams using micro-computed tomography”. In: *Journal of Materials Science* 40.22, pp. 5801–5811. ISSN: 0022-2461. DOI: [10.1007/s10853-005-4994-9](https://doi.org/10.1007/s10853-005-4994-9).
- Birgin, E. G., Lobato, R. D., and Martínez, J. M. (2016). “Packing ellipsoids by nonlinear optimization”. In: *Journal of Global Optimization* 65.4, pp. 709–743. ISSN: 1573-2916. DOI: [10.1007/s10898-015-0395-z](https://doi.org/10.1007/s10898-015-0395-z).
- Birgin, E. G., Lobato, R. D., and Martínez, J. M. (2017). “A nonlinear programming model with implicit variables for packing ellipsoids”. In: *Journal of Global Optimization* 68.3, pp. 467–499. ISSN: 1573-2916. DOI: [10.1007/s10898-016-0483-8](https://doi.org/10.1007/s10898-016-0483-8).

- Bower, A. F. (2009). *Applied mechanics of solids*. CRC press. ISBN: 9781439802472. URL: <http://solidmechanics.org/>.
- Brakke, K. A. (1992). “The Surface Evolver”. In: *Experimental Mathematics* 1.2, pp. 141–165. DOI: [10.1080/10586458.1992.10504253](https://doi.org/10.1080/10586458.1992.10504253).
- Buades, A., Coll, B., and Morel, J.-M. (2005). “A Non-Local Algorithm for Image Denoising”. In: *2005 IEEE Computer Society Conference on Computer Vision and Pattern Recognition (CVPR’05)*. Vol. 2. IEEE, pp. 60–65. ISBN: 0-7695-2372-2. DOI: [10.1109/CVPR.2005.38](https://doi.org/10.1109/CVPR.2005.38).
- Bultreys, T., Van Hoorebeke, L., and Cnudde, V. (2015). “Multi-scale, micro-computed tomography-based pore network models to simulate drainage in heterogeneous rocks”. In: *Advances in Water Resources* 78, pp. 36–49. ISSN: 03091708. DOI: [10.1016/j.advwatres.2015.02.003](https://doi.org/10.1016/j.advwatres.2015.02.003).
- Burman, E. and Hansbo, P. (2012). “Fictitious domain finite element methods using cut elements: II. A stabilized Nitsche method”. In: *Applied Numerical Mathematics* 62.4. Third Chilean Workshop on Numerical Analysis of Partial Differential Equations (WONAPDE 2010), pp. 328–341. ISSN: 0168-9274. DOI: [10.1016/j.apnum.2011.01.008](https://doi.org/10.1016/j.apnum.2011.01.008).
- Buzug, T. M. (2008). *Computed tomography: from photon statistics to modern cone-beam CT*. Springer Science & Business Media. ISBN: 978-3-540-39408-2.
- Chan, D. Y. C., Klaseboer, E., and Manica, R. (2011). “Film drainage and coalescence between deformable drops and bubbles”. In: *Soft Matter* 7 (6), pp. 2235–2264. DOI: [10.1039/C0SM00812E](https://doi.org/10.1039/C0SM00812E).
- Cornea, N. D., Silver, D., and Min, P. (2007). “Curve-skeleton properties, applications, and algorithms”. In: *IEEE Transactions on Visualization and Computer Graphics* 13.3, pp. 530–548. ISSN: 10772626. DOI: [10.1109/TVCG.2007.1002](https://doi.org/10.1109/TVCG.2007.1002).
- Cowin, S. C. and Mehrabadi, M. M. (1987). “On the identification of material symmetry for anisotropic elastic materials”. In: *The Quarterly Journal of Mechanics and Applied Mathematics* 40.4, pp. 451–476. ISSN: 0033-5614. DOI: [10.1093/qjmam/40.4.451](https://doi.org/10.1093/qjmam/40.4.451).
- Danielsson, P.-E. (1980). “Euclidean distance mapping”. In: *Computer Graphics and Image Processing* 14.3, pp. 227–248. ISSN: 0146664X. DOI: [10.1016/0146-664X\(80\)90054-4](https://doi.org/10.1016/0146-664X(80)90054-4).
- Dantzig, G. B. (1963). *Linear Programming and Extensions*. Princeton University Press. ISBN: 978-1-4008-8417-9.
- Darbon, J. et al. (2008). “Fast nonlocal filtering applied to electron cryomicroscopy”. In: *2008 5th IEEE International Symposium on Biomedical Imaging: From Nano to Macro*. IEEE, pp. 1331–1334. ISBN: 978-1-4244-2002-5. DOI: [10.1109/ISBI.2008.4541250](https://doi.org/10.1109/ISBI.2008.4541250).
- De Jaeger, P. et al. (2011). “An experimentally validated and parameterized periodic unit-cell reconstruction of open-cell foams”. In: *Journal of Applied Physics* 109.10, p. 103519. ISSN: 0021-8979. DOI: [10.1063/1.3587159](https://doi.org/10.1063/1.3587159).
- Delgado-Friedrichs, O., Robins, V., and Sheppard, A. (2015). “Skeletonization and Partitioning of Digital Images Using Discrete Morse Theory”. In: *IEEE Transactions on Pattern Analysis and Machine Intelligence* 37.3, pp. 654–666. ISSN: 0162-8828. DOI: [10.1109/TPAMI.2014.2346172](https://doi.org/10.1109/TPAMI.2014.2346172).
- Devroye, L. (1986). “Sample-based Non-uniform Random Variate Generation”. In: *Proceedings of the 18th Conference on Winter Simulation*. WSC ’86. Washington, D.C., USA: ACM, pp. 260–265. ISBN: 0-911801-11-1. DOI: [10.1145/318242.318443](https://doi.org/10.1145/318242.318443).
- Donev, A., Torquato, S., and Stillinger, F. H. (2005a). “Neighbor list collision-driven molecular dynamics simulation for nonspherical hard particles. I. Algorithmic details”. In: *Journal of Computational Physics* 202.2, pp. 737–764. ISSN: 0021-9991. DOI: [10.1016/j.jcp.2004.08.014](https://doi.org/10.1016/j.jcp.2004.08.014).

- Donev, A., Torquato, S., and Stillinger, F. H. (2005b). “Neighbor list collision-driven molecular dynamics simulation for nonspherical hard particles.: II. Applications to ellipses and ellipsoids”. In: *Journal of Computational Physics* 202.2, pp. 765–793. ISSN: 0021-9991. DOI: [10.1016/j.jcp.2004.08.025](https://doi.org/10.1016/j.jcp.2004.08.025).
- Dong, H. (2008). “Micro-CT imaging and pore network extraction”. PhD thesis. Department of Earth Science and Engineering, Imperial College London.
- Dong, H. and Blunt, M. J. (2009). “Pore-network extraction from micro-computerized-tomography images”. In: *Physical Review E - Statistical, Nonlinear, and Soft Matter Physics* 80.3, p. 036307. ISSN: 15393755. DOI: [10.1103/PhysRevE.80.036307](https://doi.org/10.1103/PhysRevE.80.036307).
- Düster, A. et al. (2008). “The finite cell method for three-dimensional problems of solid mechanics”. In: *Computer Methods in Applied Mechanics and Engineering* 197.45-48, pp. 3768–3782. ISSN: 00457825. DOI: [10.1016/j.cma.2008.02.036](https://doi.org/10.1016/j.cma.2008.02.036).
- Dyck, N. J. and Straatman, A. G. (2015). “A new approach to digital generation of spherical void phase porous media microstructures”. In: *International Journal of Heat and Mass Transfer* 81, pp. 470–477. ISSN: 00179310. DOI: [10.1016/j.ijheatmasstransfer.2014.10.017](https://doi.org/10.1016/j.ijheatmasstransfer.2014.10.017).
- Embar, A., Dolbow, J., and Harari, I. (2010). “Imposing Dirichlet boundary conditions with Nitsche’s method and spline-based finite elements”. In: *International Journal for Numerical Methods in Engineering* February. ISSN: 00295981. DOI: [10.1002/nme.2863](https://doi.org/10.1002/nme.2863).
- Felzenszwalb, P. F. and Huttenlocher, D. P. (2012). “Distance transforms of sampled functions”. In: *Theory of Computing* 8.1, pp. 415–428. ISSN: 1557-2862. DOI: [10.4086/toc.2012.v008a019](https://doi.org/10.4086/toc.2012.v008a019).
- Fernández-Méndez, S. and Huerta, A. (2004). “Imposing essential boundary conditions in mesh-free methods”. In: *Computer Methods in Applied Mechanics and Engineering* 193.12-14, pp. 1257–1275. ISSN: 00457825. DOI: [10.1016/j.cma.2003.12.019](https://doi.org/10.1016/j.cma.2003.12.019).
- Fieres, J., Schumann, P., and Reinhart, C. (2018). “Predicting failure in additively manufactured parts using X-ray computed tomography and simulation”. In: *Procedia Engineering* 213. 7th International Conference on Fatigue Design, Fatigue Design 2017, 29-30 November 2017, Senlis, France, pp. 69–78. ISSN: 1877-7058. DOI: [10.1016/j.proeng.2018.02.008](https://doi.org/10.1016/j.proeng.2018.02.008).
- Forman, R. (1998). “Morse theory for cell complexes”. In: *Topology* 37.5, pp. 945–979. ISSN: 00409383. DOI: [10.1016/S0040-9383\(97\)00071-2](https://doi.org/10.1016/S0040-9383(97)00071-2).
- Fratzl, P. and Weinkamer, R. (2007). “Nature’s hierarchical materials”. In: *Progress in Materials Science* 52.8, pp. 1263–1334. ISSN: 00796425. DOI: [10.1016/j.pmatsci.2007.06.001](https://doi.org/10.1016/j.pmatsci.2007.06.001).
- Gaitanaros, S., Kyriakides, S., and Kraynik, A. M. (2012). “On the crushing response of random open-cell foams”. In: *International Journal of Solids and Structures* 49.19-20, pp. 2733–2743. ISSN: 00207683. DOI: [10.1016/j.ijsolstr.2012.03.003](https://doi.org/10.1016/j.ijsolstr.2012.03.003).
- Gan, Y., Chen, C., and Shen, Y. (2005). “Three-dimensional modeling of the mechanical property of linearly elastic open cell foams”. In: *International Journal of Solids and Structures* 42.26, pp. 6628–6642. ISSN: 00207683. DOI: [10.1016/j.ijsolstr.2005.03.002](https://doi.org/10.1016/j.ijsolstr.2005.03.002).
- García-Moreno, F. (2016). “Commercial Applications of Metal Foams: Their Properties and Production”. In: *Materials* 9.2. ISSN: 1996-1944. DOI: [10.3390/ma9020085](https://doi.org/10.3390/ma9020085).
- Gibson, S. F. F. (1998). “Constrained elastic surface nets: Generating smooth surfaces from binary segmented data”. In: *Medical Image Computing and Computer-Assisted Intervention—MICCAI’98*, pp. 888–898. ISBN: 3-540-65136-5. DOI: [10.1007/BFb0056277](https://doi.org/10.1007/BFb0056277).
- Gong, L., Kyriakides, S., and Jang, W.-Y. (2005). “Compressive response of open-cell foams. Part I: Morphology and elastic properties”. In: *International Journal of Solids and Structures* 42.5-6, pp. 1355–1379. ISSN: 00207683. DOI: [10.1016/j.ijsolstr.2004.07.023](https://doi.org/10.1016/j.ijsolstr.2004.07.023).

- Gostick, J. T. (2017). “Versatile and efficient pore network extraction method using marker-based watershed segmentation”. In: *Physical Review E* 96.2, p. 023307. ISSN: 2470-0045. DOI: [10.1103/PhysRevE.96.023307](https://doi.org/10.1103/PhysRevE.96.023307).
- Homberg, U., Baum, D., et al. (2014). “Definition, Extraction, and Validation of Pore Structures in Porous Materials”. In: *Topological Methods in Data Analysis and Visualization III*. Vol. 56. September, pp. 235–248. DOI: [10.1007/978-3-319-04099-8\\_15](https://doi.org/10.1007/978-3-319-04099-8_15).
- Homberg, U., Binner, R., et al. (2009). “Determining Geometric Grain Structures from X-Ray Micro-Tomograms of Gradated Soils”. In: *Proc. Work. Internal Erosion 2008*. Schriftenreihe Geotechnik 21. Bauhaus-Universität Weimar, pp. 37–52.
- Hormann, K. et al. (2016). “Topological analysis of non-granular, disordered porous media: determination of pore connectivity, pore coordination, and geometric tortuosity in physically reconstructed silica monoliths”. In: *New Journal of Chemistry* 40.5, pp. 4187–4199. ISSN: 1144-0546. DOI: [10.1039/C5NJ02814K](https://doi.org/10.1039/C5NJ02814K).
- Huang, T., Yang, G., and Tang, G. (1979). “A fast two-dimensional median filtering algorithm”. In: *IEEE Transactions on Acoustics, Speech, and Signal Processing* 27.1, pp. 13–18. ISSN: 0096-3518. DOI: [10.1109/TASSP.1979.1163188](https://doi.org/10.1109/TASSP.1979.1163188).
- Hughes, T., Cottrell, J., and Bazilevs, Y. (2005). “Isogeometric analysis: CAD, finite elements, NURBS, exact geometry and mesh refinement”. In: *Computer Methods in Applied Mechanics and Engineering* 194.39-41, pp. 4135–4195. ISSN: 00457825. DOI: [10.1016/j.cma.2004.10.008](https://doi.org/10.1016/j.cma.2004.10.008).
- Iassonov, P., Gebrenegus, T., and Tuller, M. (2009). “Segmentation of X-ray computed tomography images of porous materials: A crucial step for characterization and quantitative analysis of pore structures”. In: *Water Resources Research* 45.9, pp. 1–12. ISSN: 00431397. DOI: [10.1029/2009WR008087](https://doi.org/10.1029/2009WR008087).
- Images in Public Domain (2019). [https://commons.wikimedia.org/wiki/File:Structure\\_of\\_the\\_Universe.jpg](https://commons.wikimedia.org/wiki/File:Structure_of_the_Universe.jpg) and <https://commons.wikimedia.org/wiki/File:Gray350.png> and [https://commons.wikimedia.org/wiki/File:Orange\\_Pore\\_Fungus\\_\(Favolaschia\\_calocera\)\\_33327394770.jpg](https://commons.wikimedia.org/wiki/File:Orange_Pore_Fungus_(Favolaschia_calocera)_33327394770.jpg) and [https://commons.wikimedia.org/wiki/File:Atomic\\_resolution\\_Au100.JPG](https://commons.wikimedia.org/wiki/File:Atomic_resolution_Au100.JPG).
- Immerkær, J. (1996). “Fast Noise Variance Estimation”. In: *Computer Vision and Image Understanding* 64.2, pp. 300–302. ISSN: 10773142. DOI: [10.1006/cviu.1996.0060](https://doi.org/10.1006/cviu.1996.0060).
- Inagaki, M., Qiu, J., and Guo, Q. (2015). “Carbon foam: Preparation and application”. In: *Carbon* 87, pp. 128–152. ISSN: 0008-6223. DOI: [10.1016/j.carbon.2015.02.021](https://doi.org/10.1016/j.carbon.2015.02.021).
- Inui, M. et al. (2015). “Thickness and clearance visualization based on distance field of 3D objects”. In: *Journal of Computational Design and Engineering* 2.3, pp. 183–194. ISSN: 2288-4300. DOI: [10.1016/j.jcde.2015.04.001](https://doi.org/10.1016/j.jcde.2015.04.001).
- Iwata, S., Nakatsukasa, Y., and Takeda, A. (2015). “Computing the Signed Distance Between Overlapping Ellipsoids”. In: *SIAM Journal on Optimization* 25.4, pp. 2359–2384. DOI: [10.1137/140979654](https://doi.org/10.1137/140979654).
- Jang, W.-Y., Kraynik, A. M., and Kyriakides, S. (2008). “On the microstructure of open-cell foams and its effect on elastic properties”. In: *International Journal of Solids and Structures* 45.7-8, pp. 1845–1875. ISSN: 00207683. DOI: [10.1016/j.ijsolstr.2007.10.008](https://doi.org/10.1016/j.ijsolstr.2007.10.008).
- Jerri, A. J. (1977). “The Shannon sampling theorem — Its various extensions and applications: A tutorial review”. In: *Proceedings of the IEEE* 65.11, pp. 1565–1596. DOI: [10.1109/PROC.1977.10771](https://doi.org/10.1109/PROC.1977.10771).
- Kanit, T. et al. (2003). “Determination of the size of the representative volume element for random composites: statistical and numerical approach”. In: *International Journal of*

- Solids and Structures* 40.13, pp. 3647–3679. ISSN: 0020-7683. DOI: [10.1016/S0020-7683\(03\)00143-4](https://doi.org/10.1016/S0020-7683(03)00143-4).
- Kansal, A. R., Torquato, S., and Stillinger, F. H. (2002). “Computer generation of dense polydisperse sphere packings”. In: *The Journal of Chemical Physics* 117.18, pp. 8212–8218. ISSN: 0021-9606. DOI: [10.1063/1.1511510](https://doi.org/10.1063/1.1511510).
- Al-Kharusi, A. S. and Blunt, M. J. (2007). “Network extraction from sandstone and carbonate pore space images”. In: *Journal of Petroleum Science and Engineering* 56.4, pp. 219–231. ISSN: 09204105. DOI: [10.1016/j.petrol.2006.09.003](https://doi.org/10.1016/j.petrol.2006.09.003).
- Kiefer, J. (1953). “Sequential minimax search for a maximum”. In: *Proceedings of the American mathematical society* 4.3, pp. 502–506. DOI: [10.1090/S0002-9939-1953-0055639-3](https://doi.org/10.1090/S0002-9939-1953-0055639-3).
- Kim, J.-W., Kim, D., and Lindquist, W. B. (2013). “A re-examination of throats”. In: *Water Resources Research* 49.11, pp. 7615–7626. ISSN: 00431397. DOI: [10.1002/2013WR014254](https://doi.org/10.1002/2013WR014254).
- Kırca, M. et al. (2007). “Computational modeling of micro-cellular carbon foams”. In: *Finite Elements in Analysis and Design* 44.1-2, pp. 45–52. ISSN: 0168874X. DOI: [10.1016/j.finel.2007.08.008](https://doi.org/10.1016/j.finel.2007.08.008).
- Klett, J. W., Hardy, R., et al. (2000). “High-thermal-conductivity, mesophase-pitch-derived carbon foams: effect of precursor on structure and properties”. In: *Carbon* 38.7, pp. 953–973. ISSN: 00086223. DOI: [10.1016/S0008-6223\(99\)00190-6](https://doi.org/10.1016/S0008-6223(99)00190-6).
- Klett, J. W., McMillan, A. D., et al. (2004). “The role of structure on the thermal properties of graphitic foams”. In: *Journal of Materials Science* 39.11, pp. 3659–3676. ISSN: 0022-2461. DOI: [10.1023/B:JMSC.0000030719.80262.f8](https://doi.org/10.1023/B:JMSC.0000030719.80262.f8).
- Knackstedt, M. a. et al. (2006). “Elastic and transport properties of cellular solids derived from three-dimensional tomographic images”. In: *Proceedings of the Royal Society A: Mathematical, Physical and Engineering Sciences* 462.2073, pp. 2833–2862. ISSN: 1364-5021. DOI: [10.1098/rspa.2006.1657](https://doi.org/10.1098/rspa.2006.1657).
- Lee, C.-G. et al. (2016). “Application of carbon foam for heavy metal removal from industrial plating wastewater and toxicity evaluation of the adsorbent”. In: *Chemosphere* 153, pp. 1–9. ISSN: 0045-6535. DOI: [10.1016/j.chemosphere.2016.03.034](https://doi.org/10.1016/j.chemosphere.2016.03.034).
- Li, K., Gao, X.-L., and Subhash, G. (2006). “Effects of cell shape and strut cross-sectional area variations on the elastic properties of three-dimensional open-cell foams”. In: *Journal of the Mechanics and Physics of Solids* 54.4, pp. 783–806. ISSN: 00225096. DOI: [10.1016/j.jmps.2005.10.007](https://doi.org/10.1016/j.jmps.2005.10.007).
- Lin, A. and Han, S. (2002). “On the Distance between Two Ellipsoids”. In: *SIAM Journal on Optimization* 13.1, pp. 298–308. DOI: [10.1137/S1052623401396510](https://doi.org/10.1137/S1052623401396510).
- Lindblad, J. and Sladoje, N. (2015). “Exact Linear Time Euclidean Distance Transforms of Grid Line Sampled Shapes”. In: *Mathematical Morphology and Its Applications to Signal and Image Processing*. Ed. by J. A. Benediktsson et al. Cham: Springer International Publishing, pp. 645–656. ISBN: 978-3-319-18720-4. DOI: [10.1007/978-3-319-18720-4\\_54](https://doi.org/10.1007/978-3-319-18720-4_54).
- Lorensen, W. E. and Cline, H. E. (1987). “Marching cubes: A high resolution 3D surface construction algorithm”. In: *ACM siggraph computer graphics*. Vol. 21. 4. ACM, pp. 163–169.
- Lubachevsky, B. D. and Stillinger, F. H. (1990). “Geometric properties of random disk packings”. In: *Journal of Statistical Physics* 60.5-6, pp. 561–583. ISSN: 0022-4715. DOI: [10.1007/BF01025983](https://doi.org/10.1007/BF01025983).
- Maggioni, M. et al. (2013). “Nonlocal Transform-Domain Filter for Volumetric Data Denoising and Reconstruction”. In: *IEEE Transactions on Image Processing* 22.1, pp. 119–133. ISSN: 1057-7149. DOI: [10.1109/TIP.2012.2210725](https://doi.org/10.1109/TIP.2012.2210725).

- Maire, E. (2003). “X-ray tomography applied to the characterization of cellular materials. Related finite element modeling problems”. In: *Composites Science and Technology* 63.16, pp. 2431–2443. ISSN: 02663538. DOI: [10.1016/S0266-3538\(03\)00276-8](https://doi.org/10.1016/S0266-3538(03)00276-8).
- Meijster, A., Roerdink, J. B. T. M., and Hesselink, W. H. (2000). “A General Algorithm for Computing Distance Transforms in Linear Time”. In: *Mathematical Morphology and its Applications to Image and Signal Processing*. Vol. 18. 8. Boston: Kluwer Academic Publishers, pp. 331–340. ISBN: 978-0-306-47025-7. DOI: [10.1007/0-306-47025-X\\_36](https://doi.org/10.1007/0-306-47025-X_36).
- Mosekilde, L. et al. (2000). “Trabecular bone structure and strength-remodelling and repair”. In: *J Musculoskelet Neuronal Interact* 1.1, pp. 25–30.
- Olurin, O. B. et al. (2002). “The investigation of morphometric parameters of aluminium foams using micro-computed tomography”. In: *Materials Science and Engineering A* 328.1, pp. 334–343. ISSN: 09215093. DOI: [10.1016/S0921-5093\(01\)01809-3](https://doi.org/10.1016/S0921-5093(01)01809-3).
- Øren, P.-E. and Bakke, S. (2003). “Reconstruction of Berea sandstone and pore-scale modelling of wettability effects”. In: *Journal of Petroleum Science and Engineering* 39.3. Reservoir Wettability, pp. 177–199. ISSN: 0920-4105. DOI: [10.1016/S0920-4105\(03\)00062-7](https://doi.org/10.1016/S0920-4105(03)00062-7).
- Pahr, D. H. and Zysset, P. K. (2008). “Influence of boundary conditions on computed apparent elastic properties of cancellous bone”. In: *Biomechanics and Modeling in Mechanobiology* 7.6, pp. 463–476. ISSN: 16177959. DOI: [10.1007/s10237-007-0109-7](https://doi.org/10.1007/s10237-007-0109-7).
- Perram, J. W. and Wertheim, M. (1985). “Statistical mechanics of hard ellipsoids. I. Overlap algorithm and the contact function”. In: *Journal of Computational Physics* 58.3, pp. 409–416. ISSN: 0021-9991. DOI: [10.1016/0021-9991\(85\)90171-8](https://doi.org/10.1016/0021-9991(85)90171-8).
- Piegl, L. and Tiller, W. (2012). *The NURBS book*. Springer Science & Business Media. ISBN: 978-3-642-97385-7.
- Plessis, A. du et al. (2017). “Prediction of mechanical performance of Ti6Al4V cast alloy based on microCT-based load simulation”. In: *Journal of Alloys and Compounds* 724, pp. 267–274. ISSN: 0925-8388. DOI: [10.1016/j.jallcom.2017.06.320](https://doi.org/10.1016/j.jallcom.2017.06.320).
- Pyatykh, S., Hesser, J., and Zheng, L. (2013). “Image Noise Level Estimation by Principal Component Analysis”. In: *IEEE Transactions on Image Processing* 22.2, pp. 687–699. ISSN: 1057-7149. DOI: [10.1109/TIP.2012.2221728](https://doi.org/10.1109/TIP.2012.2221728).
- Rabbani, A., Ayatollahi, S., et al. (2016). “Estimation of 3-D pore network coordination number of rocks from watershed segmentation of a single 2-D image”. In: *Advances in Water Resources* 94, pp. 264–277. ISSN: 03091708. DOI: [10.1016/j.advwatres.2016.05.020](https://doi.org/10.1016/j.advwatres.2016.05.020).
- Rabbani, A., Jamshidi, S., and Salehi, S. (2014). “An automated simple algorithm for realistic pore network extraction from micro-tomography images”. In: *Journal of Petroleum Science and Engineering* 123, pp. 164–171. ISSN: 09204105. DOI: [10.1016/j.petrol.2014.08.020](https://doi.org/10.1016/j.petrol.2014.08.020).
- Raeini, A. Q., Bijeljic, B., and Blunt, M. J. (2017). “Generalized network modeling: Network extraction as a coarse-scale discretization of the void space of porous media”. In: *Phys. Rev. E* 96 (1), p. 013312. DOI: [10.1103/PhysRevE.96.013312](https://doi.org/10.1103/PhysRevE.96.013312).
- Roberts, A. and Garboczi, E. (2002). “Elastic properties of model random three-dimensional open-cell solids”. In: *Journal of the Mechanics and Physics of Solids* 50.1, pp. 33–55. ISSN: 00225096. DOI: [10.1016/S0022-5096\(01\)00056-4](https://doi.org/10.1016/S0022-5096(01)00056-4).
- Saad, Y. (2003). “Iterative methods for sparse linear systems”. In: vol. 82. SIAM.
- Schillinger, D. and Ruess, M. (2015). “The Finite Cell Method: A Review in the Context of Higher-Order Structural Analysis of CAD and Image-Based Geometric Models”. In: *Archives of Computational Methods in Engineering* 22.3, pp. 391–455. ISSN: 1886-1784. DOI: [10.1007/s11831-014-9115-y](https://doi.org/10.1007/s11831-014-9115-y).
- Serra, J. and Vincent, L. (1992). “An overview of morphological filtering”. In: *Circuits, Systems and Signal Processing* 11.1, pp. 47–108. ISSN: 1531-5878. DOI: [10.1007/BF01189221](https://doi.org/10.1007/BF01189221).

- Sihn, S. and Rice, B. P. (2003). “Sandwich Construction with Carbon Foam Core Materials”. In: *Journal of Composite Materials* 37.15, pp. 1319–1336. DOI: [10.1177/0021998303033818](https://doi.org/10.1177/0021998303033818).
- Sihn, S. and Roy, A. K. (2004). “Modeling and prediction of bulk properties of open-cell carbon foam”. In: *Journal of the Mechanics and Physics of Solids* 52.1, pp. 167–191. ISSN: 00225096. DOI: [10.1016/S0022-5096\(03\)00072-3](https://doi.org/10.1016/S0022-5096(03)00072-3).
- Silin, D. and Patzek, T. (2006). “Pore space morphology analysis using maximal inscribed spheres”. In: *Physica A: Statistical Mechanics and its Applications* 371.2, pp. 336–360. ISSN: 03784371. DOI: [10.1016/j.physa.2006.04.048](https://doi.org/10.1016/j.physa.2006.04.048).
- Tai, S.-C. and Yang, S.-M. (2008). “A fast method for image noise estimation using Laplacian operator and adaptive edge detection”. In: *2008 3rd International Symposium on Communications, Control and Signal Processing*. March. IEEE, pp. 1077–1081. ISBN: 978-1-4244-1687-5. DOI: [10.1109/ISCCSP.2008.4537384](https://doi.org/10.1109/ISCCSP.2008.4537384).
- Taylor, J. E. (1976). “The structure of singularities in soap-bubble-like and soap-film-like minimal surfaces”. In: *Annals of Mathematics*, pp. 489–539. DOI: [10.2307/1970949](https://doi.org/10.2307/1970949).
- Tenginakai, S., Jinho Lee, and Machiraju, R. (2001). “Salient iso-surface detection with model-independent statistical signatures”. In: *Proceedings Visualization, 2001. VIS '01*. IEEE, pp. 231–238. ISBN: 0-7803-7200-X. DOI: [10.1109/VISUAL.2001.964516](https://doi.org/10.1109/VISUAL.2001.964516).
- Torquato, S. and Jiao, Y. (2010). “Robust algorithm to generate a diverse class of dense disordered and ordered sphere packings via linear programming”. In: *Physical Review E* 82.6, p. 061302. ISSN: 1539-3755. DOI: [10.1103/PhysRevE.82.061302](https://doi.org/10.1103/PhysRevE.82.061302).
- Torquato, S., Uche, O. U., and Stillinger, F. H. (2006). “Random sequential addition of hard spheres in high Euclidean dimensions”. In: *Phys. Rev. E* 74 (6), p. 061308. DOI: [10.1103/PhysRevE.74.061308](https://doi.org/10.1103/PhysRevE.74.061308).
- Van Rietbergen, B. et al. (1996). “Direct mechanics assessment of elastic symmetries and properties of trabecular bone architecture”. In: *Journal of Biomechanics* 29.12, pp. 1653–1657. ISSN: 00219290. DOI: [10.1016/S0021-9290\(96\)80021-2](https://doi.org/10.1016/S0021-9290(96)80021-2).
- Veyhl, C. et al. (2011). “Finite element analysis of the mechanical properties of cellular aluminium based on micro-computed tomography”. In: *Materials Science and Engineering: A* 528.13-14, pp. 4550–4555. ISSN: 09215093. DOI: [10.1016/j.msea.2011.02.031](https://doi.org/10.1016/j.msea.2011.02.031).
- Warren, W. and Kraynik, A. (1988). “The linear elastic properties of open-cell foams”. In: *Journal of Applied Mechanics* 55.2, pp. 341–346. DOI: [10.1115/1.3173680](https://doi.org/10.1115/1.3173680).
- Weisstein, E. W. (2019). *Spherical Cap*. From *MathWorld—A Wolfram Web Resource*. Last visited in March 2019. URL: [%5Curl%7Bhttp://mathworld.wolfram.com/SphericalCap.html%7D](https://mathworld.wolfram.com/SphericalCap.html).
- Whitby, K. T. (1978). “The physical characteristics of sulfur aerosols”. In: *Atmospheric Environment (1967)* 12.1-3, pp. 135–159. ISSN: 00046981. DOI: [10.1016/0004-6981\(78\)90196-8](https://doi.org/10.1016/0004-6981(78)90196-8).
- Wijewickrema, S. N. and Papliński, A. P. (2005). “Principal component analysis for the approximation of an image as an ellipse”. In: *Proc. 13th Int. Conf. Central Europe on Computer Graphics, Visualization and Computer Vision*. URL: <http://hdl.handle.net/11025/916>.
- Wildenschild, D. and Sheppard, A. P. (2013). “X-ray imaging and analysis techniques for quantifying pore-scale structure and processes in subsurface porous medium systems”. In: *Advances in Water Resources* 51, pp. 217–246. ISSN: 03091708. DOI: [10.1016/j.advwatres.2012.07.018](https://doi.org/10.1016/j.advwatres.2012.07.018).
- Wolff, J. (2010). “The Classic: On the Inner Architecture of Bones and its Importance for Bone Growth”. In: *Clinical Orthopaedics and Related Research®* 468.4, pp. 1056–1065. ISSN: 1528-1132. DOI: [10.1007/s11999-010-1239-2](https://doi.org/10.1007/s11999-010-1239-2).

- Yuan, Y. et al. (2016). “Multifunctional Stiff Carbon Foam Derived from Bread”. In: *ACS Applied Materials & Interfaces* 8.26, pp. 16852–16861. ISSN: 1944-8244. DOI: [10.1021/acsami.6b03985](https://doi.org/10.1021/acsami.6b03985).
- Zander, N. et al. (2014). “FCMLab: A finite cell research toolbox for MATLAB”. In: *Advances in Engineering Software* 74, pp. 49–63. ISSN: 09659978. DOI: [10.1016/j.advengsoft.2014.04.004](https://doi.org/10.1016/j.advengsoft.2014.04.004).
- Zhang, Y. et al. (2016). “Composition and structure control of ultralight graphene foam for high-performance microwave absorption”. In: *Carbon* 105, pp. 438–447. ISSN: 0008-6223. DOI: [10.1016/j.carbon.2016.04.070](https://doi.org/10.1016/j.carbon.2016.04.070).
- Zhu, H., Knott, J., and Mills, N. (1997). “Analysis of the elastic properties of open-cell foams with tetrakaidecahedral cells”. In: *Journal of the Mechanics and Physics of Solids* 45.3, pp. 319–343. ISSN: 0022-5096. DOI: [10.1016/S0022-5096\(96\)00090-7](https://doi.org/10.1016/S0022-5096(96)00090-7).

## Acknowledgements

First and foremost, I thank my advisor Jürgen Hesser. He guided and supported me since my Master's thesis, and understood well to teach me academic working and thinking. Jürgen's repeated reminders to focus on a small set of problems thoroughly, instead of random walking from topic to topic, made this work possible. Additionally, his broad knowledge, ability to comprehend my drafts, and constructive feedback gave me the opportunity to make parts of this thesis accessible to a broader scientific audience.

I thank my second advisor Guido Kanschat, who was very helpful every time I contacted him, especially during the beginning of my doctoral studies, when I aimed primarily towards finite elements.

Many thanks to Stanislav Pyatykh for overlooking my progress until he started working outside academia.

Volume Graphics provided me with a regular salary (and coffee and sweets), but more importantly, kind, intelligent and experienced colleagues, who always gave advice when I sought it. Thank you Christof Reinhart, Thomas Günther and Christoph Poliwoda for founding Volume Graphics, and putting your trust in me, and thank you to my colleagues, particularly Johannes Fieres, the simulation team, and the lunch group.

Some data of this work was available due to the generous help of Hermann Finckh and Albrecht Dinkelmann from DITF. Thank you for making a CT scan of the carbon foam sample. I also thank Thomas Strobel from Schunk GmbH for providing the sample.

Throughout my life, I was in the fortunate situation to have a caring and loving family, and amazing friends. Thank you Isabel for the profound love we share. You bring out the best parts in me, going well beyond achieving this degree. Thank you (Mama) Sylvia and (Papa) Franz for your unconditional love and support, which sets an example for me that I will live up to. Thank you Devi and Joey, you are my beloved sisters, and I am proud that you are such successful and independent women. Thank you to my grandparents and further relatives. I also thank my friends, including the choir "Klangfarben".

If you read this text and feel like you did not get any recognition, I apologize that you remain unmentioned: At last, this page is too small to contain all the remarkable people which contributed directly and indirectly to the thesis.

